POLITECNICO DI TORINO

Master's Degree in Biomedical Engeneering

Master's Degree Thesis

Contactless human vital signals monitoring based on a FMCW Radar

Supervisors

Prof. Danilo DEMARCHI

Ph.D. Paolo MOTTO ROS

Ph.D. Irene BURAIOLI

Candidate

Marco POGLIANO

December 2022

Abstract

Breath and heart rate, highly used during the recent Covid emergency, are among the first vital parameters of clinical interest. They can provide lots of information about a person's state of health. Their continuous monitoring will be a sector of great interest in the next decades by companies operating in various fields, mostly in healthcare (home monitoring, elderly patients, or for sleep analysis). According to the latest report by the WHO (World Health Organization), the world population is aging, thanks to the advancements in medicine, leading to an increase in geriatric diseases related to breathing and the cardiovascular system. Nowadays, monitoring breath and heart rate technologies are mainly wearable, and based on electrodes or contact sensors. However, these technologies have the disadvantage of being uncomfortable for the subject, sometimes irritating to the skin, and highly sensitive to the level of skin-sensor contact. New remote technologies are therefore being studied, and the thesis project is part of this new research field. The aim is to design an automatic system based on Infineon's BGT60ATR24C FM (Frequency Modulated) radar, developed in an ECSEL-JU project called AI4CSM (Automotive Intelligence for Connected Shared Mobility) with Polytechnic of Turin as partner, chosen because of its reduced size. Being a prototype, the radar required a careful characterization and investigation of the performance, aiming at monitoring the millimeter displacement of the chest wall from a distance. Then, an algorithm was designed with the aim of locating the human and extract its vital parameters by processing the data acquired from the radar. Signal frequency analysis based on a high-resolution PSD (Power Spectral Density) was used to obtain the necessary spatial resolution. The first validation phase was carried out using manually generated signals on Matlab, by superimposing variable noise on the breathing signals. The second validation phase was performed using the filament 3D printer, RepRap X400, reprogramming it in its native language (gcode) to simulate vital signs. The modelling of breathing was in these steps of the sinusoidal type with different amplitude levels, in the literature between 4 and 12 millimeter. After fine tuning the algorithm to improve its robustness, a third validation phase was carried out on volunteer subjects. Standing one meter far from the radar, the subject was asked to breathe in a relaxed condition. The vital parameters extracted

were compared with those obtained by respiratory belt and photoplethysmography, taken as the gold standard.

Table of Contents

List of Tables

List of Figures

Acronyms

PSD
Power Spectral Density

UWB
Ultra Wide Band

IR-UWB
Impulse Radio Ultra Wide Band

FM
Frequency Modulated

CW
Continuous Wave

FMCW
Frequency Modulated Continuous Wave

CAD
Computer-Aided Design

Tx
Transmitted Antenna

Rx
Receiver Antenna

BW
Bandwidth

CDT

Chirp Duration Time

CRT

Chirp Repetition Time

IF

Intermediate Frequency

DFT

Discrete Fourier Transform

FFT

Fast Fourier Transform

SIMO

Single Input Multiple Output

MIMO

Multiple Input Multiple Output

Chapter 1

Introduction

According to data from the latest report from the World Health Organization (WHO), the population is increasing, thanks to the evolution of medicine and clinical engineering that have made it possible to extend the average life span of people [1]. However, the aging of the population brings an increase in cardiovascular diseases, of more significant impact in modern societies than in the past, and a significant increase in chronic diseases linked to age [2, 3]. The coming of COVID has also highlighted how respiratory diseases are more than ever to be kept under control and have a substantial impact, given that many of the most severe implications of the disease have been observed, especially in patients with previous respiratory diseases. These data show us how the monitoring of the elderly is a growing need in hospitals, and nursing homes, for those patients who carry out treatment at home or for the simple control of the state of health of chronic patients [4]. Therefore, monitoring vital parameters, such as heart rate and respiratory rate, is of clinical relevance to knowing the patient's state of health [5]. With this in mind, in recent decades, devices capable of real-time monitoring of the patient's condition have increasingly been developed [6]. Contact devices were developed first. They are also the most used to monitor respiration and cardiac activity, such as ECG (electrocardiography), PPG (photoplethysmography), and breathing belts [7] (***figure 1.1***).

These devices use electrodes, piezoelectric or piezoresistive sensors, or radiation in the infrared range to extract the vital parameters of interest. Although they have a high degree of accuracy, they also have several limitations. They allow limited mobility of the subject, causing a condition of non-comfort. They may disconnect during use due to hindrance of the cables; they can cause discomfort to the skin and, in the most severe cases, allergic reactions are inapplicable on tissues damaged by wounds or burns and also sometimes suffer from the presence of clothes or clothing [6, 7]. Over the years, wearable sensors based mainly on accelerometers

(a) *ECG device*

(b) *PPG device*

(c) *Respiration belt*

Figure 1.1: Traditional devices to record respiration and heart rate.

and LEDs have also been produced to extract parameters less invasively, having the advantage of being integrated into smartwatches or bracelets, ***figure 1.2***.

Figure 1.2: Smartwatch with PPG and ECG measurements.

The limits of these devices are the dependence on the ambient light conditions and the conditions of contact with the skin that can alter the reading of the sensors

[7]. To overcome these problems, non-contact imaging-based devices and radar-based systems have become increasingly popular in recent decades. Imaging-based devices can be thermal imaging or optical imaging using RGB cameras, ***figure 1.3***. They can also be coupled to simultaneously extract multiple parameters such as body temperature, heart rate, and respiratory rate.

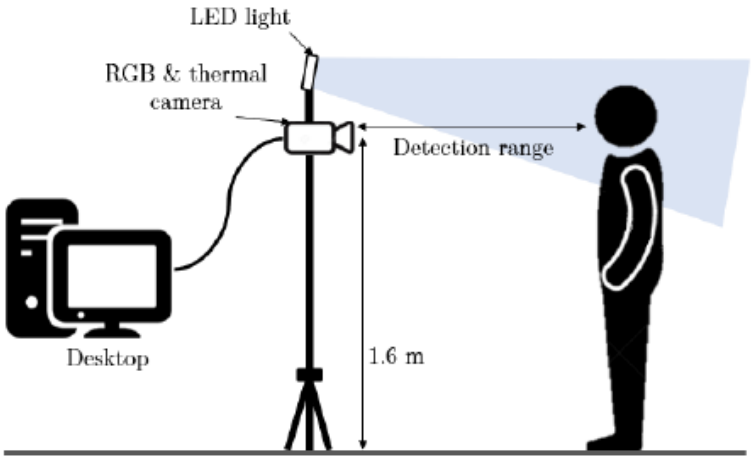

Figure 1.3: RGB and thermocamera set up [8].

The images produced by the cameras are analyzed and processed through neural networks to extract the parameters of interest. Thermal cameras localize the subject by exploiting the higher human temperature than the environment. In contrast, cameras analyze the thoracic movements influenced by respiratory and cardiac activity by extracting ROI [8]. These systems, however, have a high dependence on the external lighting conditions and the visual occlusion of the subject. For these reasons, instead, devices based on UWB (Ultra Wide Band) radars have been developed for the monitoring of vital parameters without contact, and it is precisely here that this thesis work fits. The main difference compared to other types of radar is linked to the frequency of the radiation used, in this case in the order of GHz. The operating mechanism is the same; a signal is emitted through a transmitter antenna, the object of interest reflects this, and the reflected signal is recorded with the receiving antenna [9]. For this application, the reflective object is the chest's patient, ***figure 1.4***. The respiratory and heart rate information of interest are contained in the micro-movements of the chest wall. Specific signal processing can extract these bio-signals. In fact, during the various respiratory phases, the rib cage expands and contracts due to the entry and exit of air. Cardiac activity, on the other hand, manifests itself as an external pulsation due to the diastolic and systolic contractions of the heart.

The application of the monitoring of cardiac-respiratory parameters has clinical

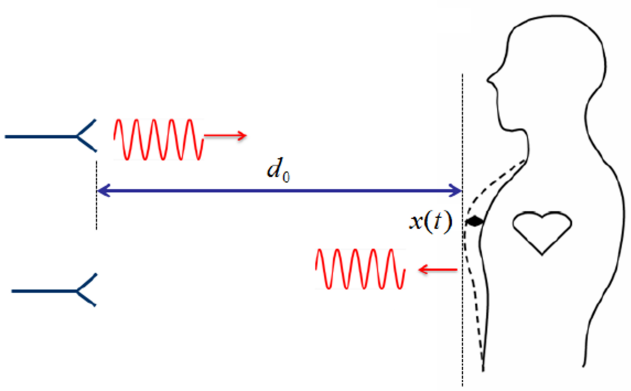

Figure 1.4: Thoracic displacement scheme during breathing [4].

relevance for the control and verification of a patient's state of health but also finds many applications that make this technology of great interest. It is used in research operations following disasters such as collapses or natural disasters such as earthquakes, allowing the status of survivors to be verified even in conditions that are difficult to reach [10, 11]. They are also used during sleep monitoring to evaluate diseases such as OSA (Obstructive Sleep Apnea), the most common respiratory disorder characterized by repetitive obstruction of the upper airways during sleep. They can be used at home to monitor the fall of older people at risk [12] or in smart homes, automatically adjusting the home's heating, saving on bills, improving livability, and reducing pollution [13]. They can also be used for security and surveillance, even in the military [14]. In the latest radiotherapy devices, UWB radars are used to evaluate respiratory rate and chest wall movement to synchronize radiation emission and improve target centering by reducing injury to healthy tissues and maximizing tumor mass destruction [15]. Another wide field of use is the automotive one, where they can be used to monitor the driver's health to avoid accidents due to sleepiness, high stress, or various types of illness [16].

1.1 Thesis outline

The following thesis is divided into chapters organized as follows:

- **Chapter 2** describes the theoretical background, including theoretical foundations of the radar's physic; signal case histories specifically for radar FMCWs; theoretical analysis of PSD and selection criteria as an analysis method; algorithms for extraction of respiration rate from radar data found in the literature;

modeling of respiratory and cardiac signals found in the literature along with a physiological presentation of the two phenomena.

- **Chapter 3** describes the device with its technical characteristics and the characterization tests performed on it.
- **Chapter 4** describes in detail the algorithm implemented in this thesis project. The developed GUI and the main parts defining the algorithm's operation are described.
- **Chapter 5** describes the CAD of the radar case, the 3D filament printer used for the breathing simulations, the writing language (gcode) for programming the printer, and the mode of conversion from a digital signal to gcode.
- **Chapter 6** presents and discusses the results obtained in the different validation phases, namely the analysis phase of data synthesized with Matlab, the analysis phase of real data taken from database [2], the validation phase performed with the simulations done with the 3D printer, and finally the tests performed on volunteer subjects.
- **Chapter 7** presents the conclusions of this thesis work with final comments on the results obtained.

Chapter 2

Background

2.1 Radar basics

The mechanism of operation of a radar system is quite simple. An electromagnetic wave emitted by the Tx antenna interacts with the surrounding environment. The receiving antenna records the reflective wave. From the analysis of the two signals, emitted and reflected, it is possible to describe the surrounding environment. The presence of an object at a certain distance will reflect the wave emitted with a certain time shift and with a certain power concerning its characteristics, such as its size. A high-level descriptive block diagram of a radar device is shown in ***figure 2.1***. The shape generator has the function of producing the waveform of the emitted signal. The emitter circuit transforms this into the electromagnetic wave emitted by the emitting antenna. At the same time, the receiver circuit records the electromagnetic wave received through the receiving antenna. The two signals thus obtained are combined with different strategies, depending on the type of radar in the mixer. The output signal is analyzed in the signal processing block producing the final result. The power supply and timing and control blocks supply energy to the system, the former, and control the correct execution of the various operations, the latter.

The waveform generator is the central block that differentiates the different radars because, based on the type of waveform emitted, the radars are generally divided into pulsed or continuous wave radars (CW). In pulsed radar, the wave is emitted for short and specific time intervals, while in CW radar, the wave is emitted continuously. The emitted signal can also be modulated or not, generally with frequency modulation. It is also possible to change the wave's shape concerning the application of the radar [17]. All these aspects are explored in detail in the following chapters by individually analyzing pulsed and continuous wave radars.

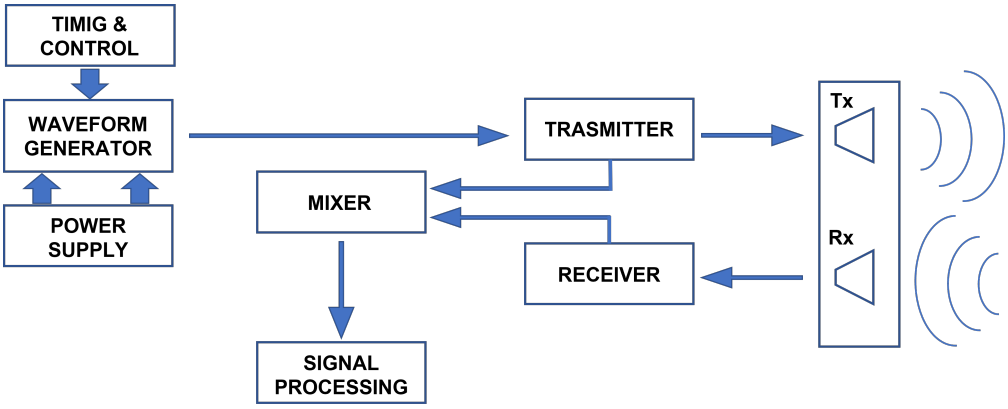

Figure 2.1: Block scheme of a generic radar.

2.1.1 Pulsed Radar

A pulsed radar uses short pulses as the emitted signal and records the return echo to evaluate the distance of the object of interest. In this type of radar, only one antenna is necessary because the same is used first as the emitter and second as the receiver. The calculation of the distance is therefore subordinated to the measurement of a time difference between the moment of emission of the pulse and the reception of the echo, as shown in ***equation 2.1***, where d is the distance to be estimated, Δt is the measured time interval and c is the propagation speed of the electromagnetic wave (speed of light).

$$d = \frac{c\Delta t}{2} \tag{2.1}$$

Since distance estimation is based on a temporal measurement, this type of radar is often used for long-distance measurements, for which the temporal distance between the emitted signal and the echo is easily and precisely measurable with low-cost electronics [18]. For short-range applications, in the order of the meter, the precise measurement of time intervals in the order of a few milliseconds is required, making it necessary to use high-performing and expensive electronics. A subclass of pulsed radars is the IR UWB (Impulse Radio Ultra Wide Band), in which the pulse emitted is modulated in frequency with a wide band, allowing it to be used even in applications at a shorter distance. The following chapters will explore the advantages of frequency modulation, specifically for CW radars. However, it is necessary to underline that the great advantage of a pulsed radar compared to a CW radar is to be found in consumption. The limited emission to short time intervals compared to the continuous emission of the CW radar makes the consumption of a pulsed radar significantly lower.

2.1.2 Continuous Wave Doppler

The presence of two antennas characterizes a continuous wave radar, one receiving and one emitting, since the signal is emitted in a constant form. Therefore, it would not be possible to use the same antenna as with pulsed radars. Doppler radars, in particular, exploit a signal with fixed and stable amplitude and frequency generated by an oscillator inside the device. The pattern of the signal is given in ***equation 2.2***, where A is the amplitude of the signal, f_T is the frequency of the emitted signal, ϕ_0 is the phase of the signal.

$$y(t) = A\ sin(2\pi f_T t + \phi_0) \tag{2.2}$$

These radars are mainly used for detecting the speed of objects in the field of view (FoV) by exploiting the Doppler effect. The frequency contribution of the received signal will differ from the sent signal. From the frequency analysis of the received signal, it is possible to extract the Doppler frequency f_D used to calculate the speed of the object, as given in ***equation 2.3***.

$$v = \frac{c\ f_D}{2\ f_T} \tag{2.3}$$

As given in ***equation 2.4***, the angular velocity is related to the frequency by the factor 2π and is also defined as the time derivative of the phase shift.

$$\omega = 2\pi f = \frac{d\phi}{dt} \tag{2.4}$$

The total phase shift of the wave can be calculated as in ***equation 2.5***, where R is the distance between the antenna and the object and λ is the wavelength. In fact on a path length of 2R the wave makes N oscillations given by the ratio of path length to wavelength where each wavelength introduces a phase shift of 2π.

$$\phi_0 = \frac{4\pi R}{\lambda} \tag{2.5}$$

Combining ***equation 2.4*** and ***equation 2.5*** yields ***equation 2.6***.

$$2\pi f = \frac{\frac{d(4\pi R)}{\lambda}}{dt} \tag{2.6}$$

Developing the latter, taking into account that the derivative of the distance in time is the velocity of the object, ***equation 2.7*** is obtained.

$$f = \frac{1}{2\pi}\frac{4\pi}{\lambda}\frac{dR}{dt} \tag{2.7}$$

We prove the relationship between Doppler frequency and velocity of the object under consideration by substituting for the generic frequency f just the frequency difference of the Doppler phenomenon, as in ***equation 2.8***.

$$f_d = \frac{2v}{\lambda} = \frac{2vf_T}{c} \tag{2.8}$$

Observe from this formulation of the Doppler frequency that it is directly proportional to the velocity of the object v and the frequency of the emitted signal, f_T. Therefore, to obtain a high-velocity resolution, it is preferable to have a high frequency of the emitted signal that results in a higher Doppler frequency, which is more easily measured at the same frequency resolution. Finally, to obtain the ***equation 2.8***, it is sufficient to substitute for the value of λ its formulation given by the ratio of the wave speed, light speed c, to the frequency of the wave and rewrite the equation as a function of the object speed [19]. The significant limitations of this type of radar are the inability to measure the object's absolute distance [20] of the object because it lacks a time reference and the failure to distinguish different objects with similar velocities.

2.1.3 Frequency Modulated Continuous Wave

FMCW have the characteristic of emitting a frequency-modulated signal allowing the limitations of Doppler radars to be overcome, yet with the advantages of continuous emission. Frequency modulation allows for constructing a time reference and even distance measurements between radar and object within the field of view. Radar with different center band frequencies and bandwidths falls into this category, thus allowing uses in a wide variety of areas. The service, in fact, of lower frequencies, facilitates object displacement extraction operations. In comparison, using higher frequencies increases the sensitivity of the device, allowing the detection of small amplitude movements, such as thoracic movements due to breathing, in which this study is interested [6]. The main characteristics of these radars can be summarized as follows [18]:

- Ability to measure small movements in relation to the frequencies of the emitted signal;
- Ability to simultaneously measure displacement and velocity of the object under investigation;
- High stability in measurements, reducing errors;
- Reduced size by taking advantage of miniaturization technologies;
- Reduced power consumption;

- Safety due to absence of pulse signals.

All these features make them ideal for measuring small displacements in a field of view (FoV) at short distances, precisely the scenario considered in this thesis. A generic block diagram of an FMCW radar is presented in ***figure 2.2***. The

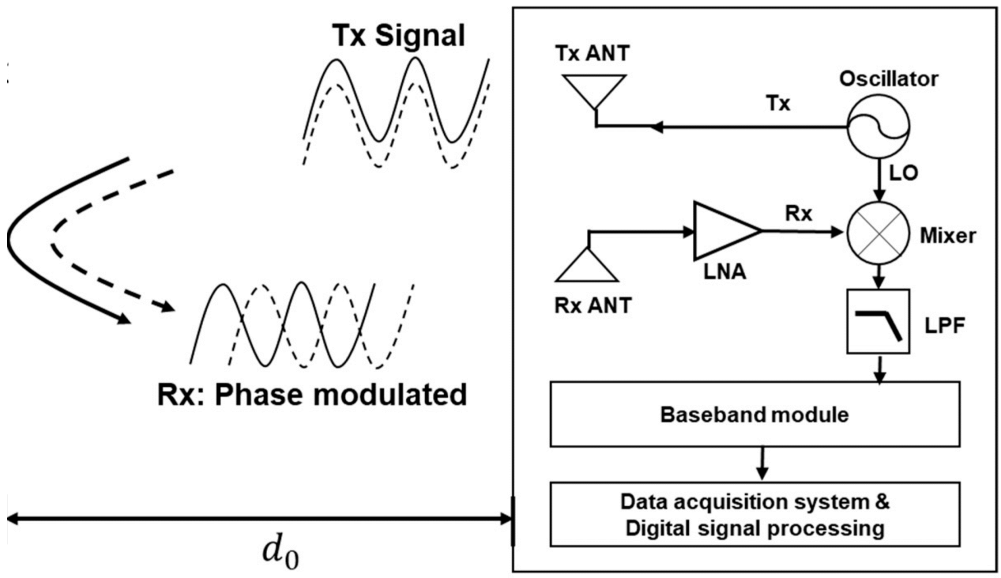

Figure 2.2: Block scheme of a FMCW radar.

emission block consists of the emitting antenna that receives the signal from the oscillator. The oscillator inputs all the characteristic parameters of the waveform and generates the wave. To the mixer, the same signal is passed. During the flight phase, the emitted wave undergoes a phase shift due to flight time and environmental interactions. The echo signal is transmitted through the receiving antenna to the mixer as a second input after it has been processed. An LNA (Low Noise Amplifier) amplifies the received signal to cope with the power loss during the flight phase. The output of the mixer is the time product between the two signals. The new signal is low-pass filtered to remove high-frequency components not of interest. Then the signal is digitally transformed by an ADC to be processed, obtaining the measurements of interest.

Modulation patterns

Signal modulation can be of different types depending on the application and objective of the measurement [18, 20]. The main, but not the only, types of modulation are shown below and depicted in ***figure 2.3***:

- Square wave modulation (FSK) is based on the emission of a pulsed signal obtained by switching between two states of the system. It is a modulation that allows high-precision measurement over a close distance by comparing the phases of the two signals. However, it cannot distinguish echoes from multiple objects making the measurement range considerably narrow. The inability to detect multiple targets makes it inefficient in the application of detecting multiple subjects;

- Sawtooth modulation has a frequency change that grows linearly over time. It is one of the most widely used modulations because it allows for a wide range and uniquely detects multiple objects. However, it is not optimized for doppler measurement and is, therefore, less efficient than other modulations for velocity measurement;

- Stepped modulation is characterized by a stepped frequency increase. This modulation is very similar to sawtooth modulation and is mainly used for interferometric measurements. It also has the advantage of expanding the spatial analysis range of the radar;

- Triangular modulation is based on a double linear front, one of greeting and one of descent. It is a modulation that couples two opposite sawteeth. It is a modulation that, compared to its counterpart, sawtooth modulation, is more efficient in measuring doppler frequencies and velocities. However, the doppler frequencies are not uniquely separable in the case of multiple objects with the same speed;

- Sinusoidal modulation is based on a sinusoidal frequency change. It is a particularly simple modulation whose applications are mainly in short-range altimeters, moving target sensors, and level-measuring radar.

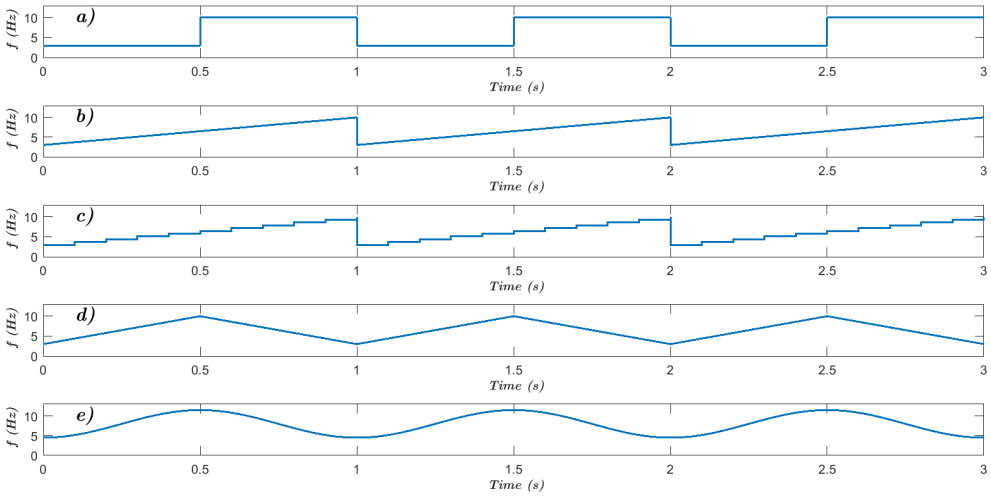

Figure 2.3: Basic patterns modulation. a) Square Wave b) Sawtooth c) Stepped d) Triangular e) Sinusoidal.

A sawtooth modulation was chosen for the application under consideration, which allows for precise distance measurements even at short distances with the possibility of analyzing the subject's speed. In this type of modulation, the emitted signal is a chirp characterized by a linear increase in frequency over time, as in ***equation 2.9***, where A is the amplitude, $f1$ is the starting frequency, S is the slope $[Hz/s]$ and ϕ is the starting phase.

$$y(t) = A\ sin(2\pi(f_1 + St) + \phi) \tag{2.9}$$

The main characteristics of this type are:

- Centerband frequency, which is the f_0 working frequency of the radar;
- Bandwidth (BW), which is the bandwidth of the signal between f_1 and f_2;
- Chirp duration time (CDT);
- Chirp repetition time (CRT).

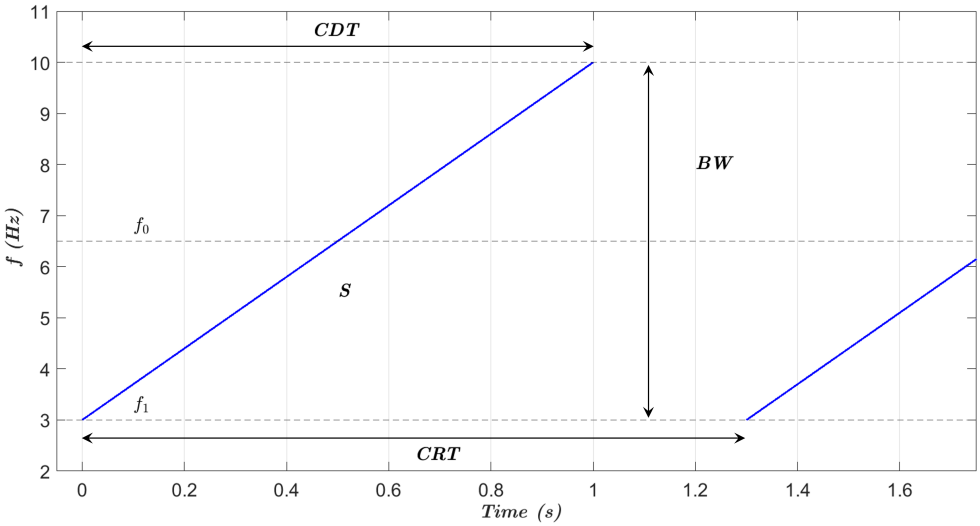

Figure 2.4: Time-frequency chirp representation.

Fixed Single Object

FMCW radars have the particularity of allowing the measurement of the distance between the device and an object. The emitted signal $S_t(t)$ (***equation 2.10***) is a chirp with its amplitude A, its own centerband frequency f_0 and its phase ϕ_t.

$$S_T(t) = A\ sin(2\pi(f_0 + St) + \phi_T) \tag{2.10}$$

After interacting with the object, in this first single and completely reflective analysis, it returns in the form of an echo to the receiving antenna with a τ time delay (***equation 2.11***).

$$S_R(t) = B\ sin(2\pi(f_0 + S(t - \tau)) + \phi_R) \tag{2.11}$$

This phenomenon is reported in a time-frequency representation (***figure 2.5***), where τ is the delay between the two signals, S is the slope of the chirp given by the ratio between BW and CDT. The delay the time interval used by the participation to complete the radar-object-radar trajectory is equal to the ratio between the double of the distance d and the speed of the radiation, equal to the speed of light c (***equation 2.12***).

$$\tau = \frac{2d}{c} \tag{2.12}$$

In ***figure 2.5*** it is also observed how, in the time-frequency representation, the frequency shift between two curves in a given period is equal to $S\tau$, and this is precisely the signal of interest in this type of radar. This signal is called the IF

(Intermediate Frequency) signal. If the device were a simple pulsed radar, it would be necessary to measure the τ period between the two signals, which, however, for short-range applications (< 3 m), would require time interval measurements in the order of μs for fixed distances and in the order of the to solve movements of a few millimeters in amplitude. The peculiarity of an FM device lies precisely in the fact that the temporal information is contained within frequency domain.

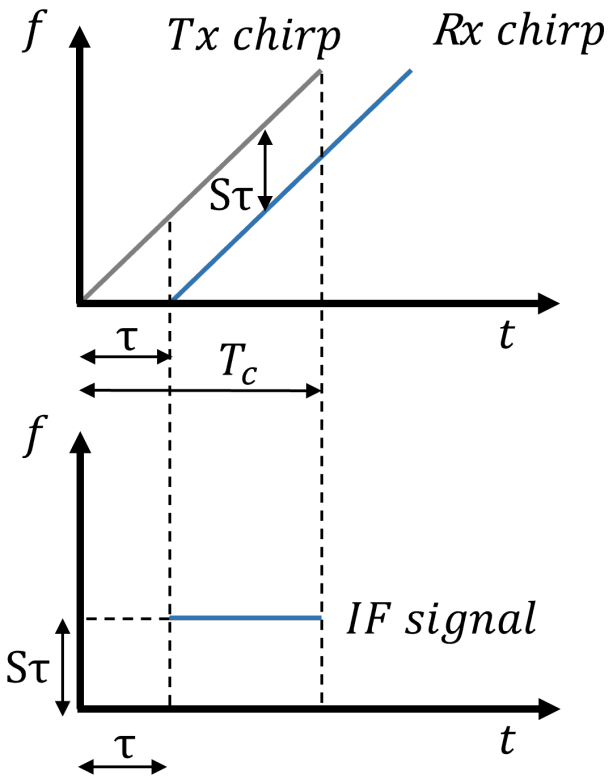

Figure 2.5: TX and Rx chirps time-frequency representation.

The mixer takes the two signals, the transmitted and the received one, as input and multiplies them with each other over time. The output is the IF signal. The mathematical product of two sinusoids results in a sum of two components. The first has a frequency equal to the difference between the two starting sinusoid frequencies and has a phase equal to the difference between the phases. On the other hand, the second component is a chirp with a frequency equal to the single frequency sum and a phase equal to the sum of the phases. Therefore, multiplying the signals $S_t(t)$ and $S_r(t)$ (***equation 2.10*** and ***equation 2.11***) we obtain the

signal $S_{fin}(t)$ (***equation 2.13***).

$$\begin{aligned} S_{fin}(t) =& Csin(2\pi S\tau + (\phi_T - \phi_R)) + \\ & Dsin(2\pi(2(f_0 + St) - S\tau) + (\phi_T + \phi_R)) \end{aligned} \tag{2.13}$$

This signal has a low-frequency component and a high-frequency component. The low-frequency component is precisely that of interest to evaluate the radar-object distance. Its frequency, as reported in ***equation 2.13***, is proportional to the product of S and τ, where S is the slope of the chirp, and τ is the time delay. The phase, on the other hand, is given by the product between the IF and the re-writable τ delay (***equation 2.14***), as a ratio between the distance and the radiation wavelength with a multiplicative coefficient.

$$\phi_0 = 2\pi f_{IF}\tau = \frac{4\pi d}{\lambda} \tag{2.14}$$

By exploiting both information it is possible to trace the distance value as reported in ***equation 2.15***.

$$\begin{cases} d = \dfrac{\phi\lambda}{4\pi} \\ d = \dfrac{f_{IF}c}{2S} \end{cases} \tag{2.15}$$

On the other hand, the high-frequency component is disturbing and therefore filtered with a cascade low-pass filter. Furthermore, it requires highly performing electronics with a sampler working at frequencies in the order of GHz to be analyzed and used.

As an example of the previous discussion, the following is an analysis conducted on Matlab with simulated signals. In ***figure 2.6*** are represented an example of a transmitted signal, received signal, and the mixer output. For this demonstration, frequencies in the ultrasound band are used to simplify the calculates and the representation. On ***figure 2.7***, instead, the power spectral density (PSD) of the mixed signal is shown to allow the reader to appreciate the lower frequency component, the IF signal, and the higher frequency component. All the parameters used in this simulation are reported in ***table 2.1***. The entered speed and time delay parameters between the emitted and received signal lead to calculating the radar-object distance of 0.34 m using ***equation 2.12*** as a function of distance. On the other hand, the low frequency of the IF signal uses the ***equation 2.15*** results to be equal to 600 Hz, considering the value of S equal to 300 kHz/s given by the ratio between BW of 3 kHz and duration of the chirp (T) of 10 ms. From the PSD analysis, the peak appears to be at 610,35 Hz. This discrepancy is due to the frequency resolution of the analysis with the PSD. The frequency error of 1.7% is propagated to the final distance estimated as 0,345 m. All this analysis is valid in the presence of a single stationary object because the conditions change in the presence of multiple objects or moving objects.

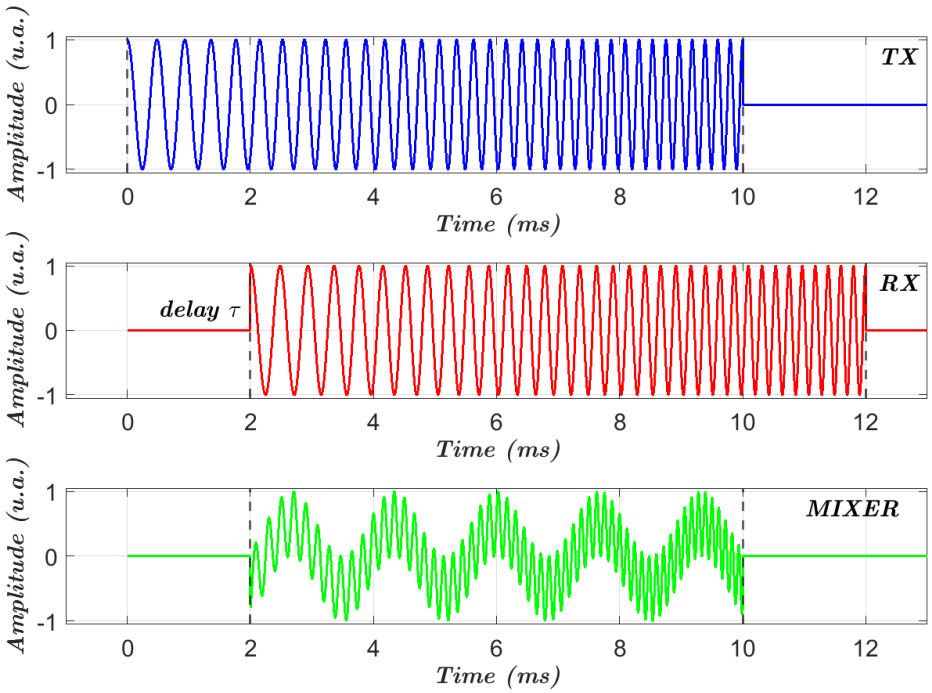

Figure 2.6: Single object example : TX, RX and Mixer signals in time.

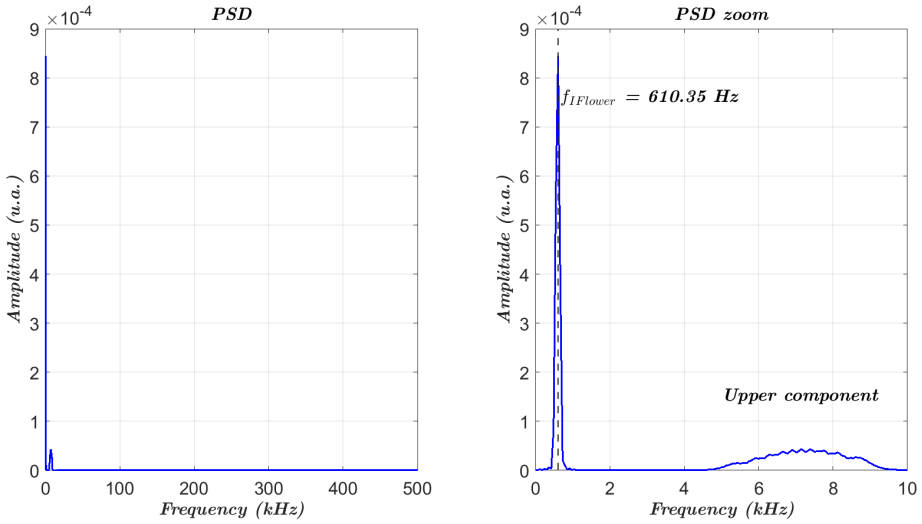

Figure 2.7: Complete and zoomed PSD of the example mixer signal.

Table 2.1: Parameters used for the fixed single object DEMO of the FM radar elaboration.

Parameter	***Value***
center-band frequency (f_0)	3,5 kHz
chirp frequency start	2 kHz
chirp frequency end	5 kHz
chirp duration time (CDT)	10 ms
delay Rx vs Tx	2 ms
radiation velocity	340 m/s
sampling frequency	1 MHz

Fixed Multiple Object

In the case of multiple objects, the return signal will not be unique, but more than one will combine each other with a different delay. The time-frequency representation will be as in ***figure 2.8***. Therefore, the resulting IF signal will not have a single contribution in frequency but will be a combination of several frequency contents. In ***figure 2.9*** is also reported in this case an example with synthesized signals, whose parameters are reported in ***table 2.2***. Three objects at different distances were simulated, and the mixer output signal PSD was performed. The various objects produce distant low-frequency peaks of the IF signal.

Table 2.2: Parameters used for the fixed multiple objects DEMO of the FM radar elaboration.

Parameter	***Value***
center-band frequency (f_0)	3,5 kHz
chirp frequency start	2 kHz
chirp frequency end	5 kHz
chirp duration time (CDT)	10 ms
delay 1	2 ms
delay 2	3 ms
delay 3	5 ms
radiation velocity	340 m/s
sampling frequency	1 MHz

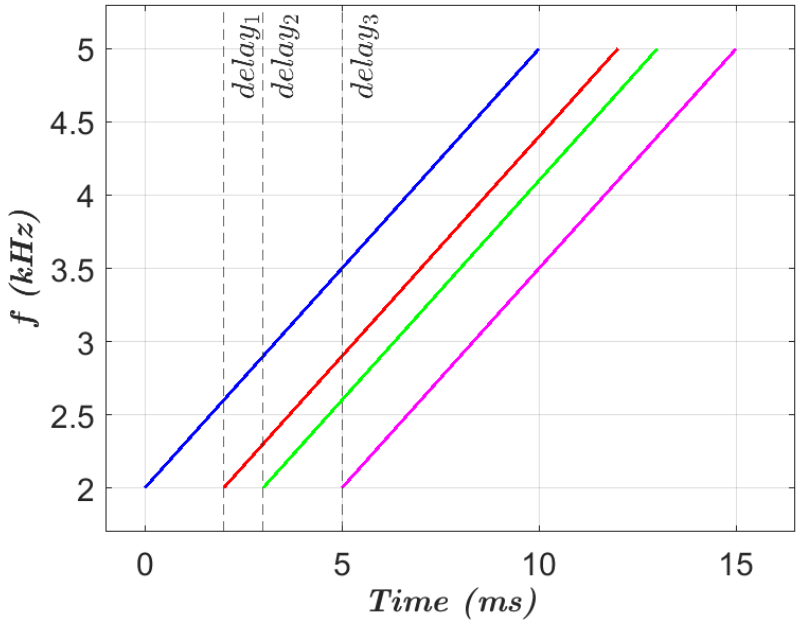

Figure 2.8: Multiple Objects time-frequency chirps representation.

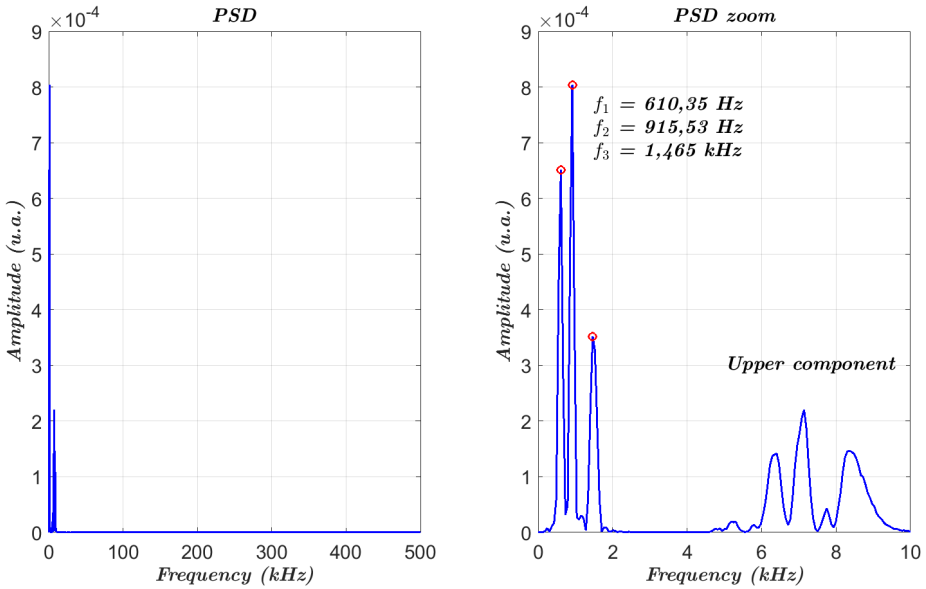

Figure 2.9: PSD example for multiple object configuration.

Moving Object

Moving objects mixer output will have a Doppler contribution in addition to the shift frequency given by the return echo delay. The Doppler frequency is then

added with a sign to the frequencies of the signal received. The time-frequency representation in (***figure 2.10***) shows this phenomenon. If not considered, it can go to an under or overestimate of the real radar-object distance. In ***table 2.3*** shows the parameters used for the simulation. In this particular situation, an object was simulated that moves radially approaching the radar at a speed of 10 m/s. By exploiting ***equation 2.8***, the estimated Doppler frequency is 205.88 Hz added to the received chirp. This Doppler contribution introduces, as seen in ***figure 2.10***, an upward shift of the time-frequency representation of the received chirp.

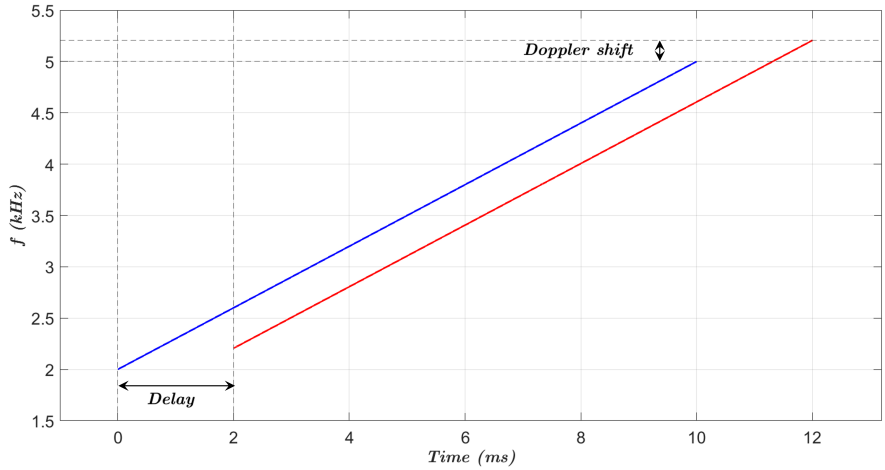

Figure 2.10: Moving objects time-frequency chirps representation.

Table 2.3: Parameters used for the moving object DEMO of the FM radar elaboration.

Parameter	***Value***
center-band frequency (f_0)	3,5 kHz
chirp frequency start	2 kHz
chirp frequency end	5 kHz
chirp duration time (CDT)	10 ms
delay	2 ms
radiation velocity	340 m/s
object velocity	10 m/s
sampling frequency	1 MHz

Spatial resolution and Power Analysis

For any application of use, and in particular, for this thesis, it is essential to know and identify the range and spatial and speed resolution of the device. After being filtered, the mixer's output signal is analyzed in frequency. In this case, the frequency analysis is carried out with the PSD, which finds its foundations in the Fourier Transform. This type of analysis, having fixed an observation window of duration T_c, imposes a theoretical resolution in frequency, which, as seen previously, sets a theoretical spatial resolution. In our case, the period of the T_c window coincides with the duration of the single chirp issued since the device sends single chirps spaced apart. Fourier analysis applied to a signal of duration T_c has a theoretical resolution in Δf frequency equal to the inverse of the interval T_c (***equation 2.16***).

$$\Delta f = \frac{1}{T_c} \tag{2.16}$$

This theoretical frequency resolution implies that two frequency peaks are distinguishable only if they are at least Δf apart. The IF signal is reported in ***equation 2.17***. Its formulation as a function of distance, where S is the slope expressed in Hz/s, d is the radar-object distance, and c is the speed of the radiation.

$$f_{If} = \frac{2\ S\ d}{c} \tag{2.17}$$

This treatment, specialized in IF, implies that two objects are distinguishable at least Δd apart and therefore contribute in frequency with a phase shift of at least Δf. The combination of ***equation 2.17*** in differential form, ***equation 2.16***, and T_c definition as bandwidth BW and slope S ratio, lead to ***equation 2.18***.

$$\Delta f = \frac{2\ S\ \Delta d}{c} = \frac{1}{T_c} = \frac{S}{BW} \tag{2.18}$$

Reformulating (***equation 2.19***) the spatial resolution of the device is described.

$$\Delta d = \frac{c}{2\ BW} \tag{2.19}$$

As far as the power of the echo signal is concerned, this is abundantly dealt with in [21]. The power density S_T at a distance d is expressed as in ***equation 2.20***, where P_T is the transmitted power and G_T is the gain of the transmitting antenna.

$$S_T = \frac{P_T G_T}{4\pi d^2}[\frac{W}{m^2}] \tag{2.20}$$

From its formulation it emerges that the power decreases with the square of the distance. The power density received S_R on the receiving antenna following the

reflection on the target object is expressed as in ***equation 2.21***, where σ is the Radar Cross Section (RCS) defined as the ability of the target to reflect the incident radiation.

$$S_R = \frac{P_T G_T}{4\pi d^2} \frac{\sigma}{4\pi d^2} [\frac{W}{m^2}] \tag{2.21}$$

In order to define the total power received, it is first necessary to define the effective area as in ***equation 2.22***, where G_R is the gain of the receiving antenna and λ is the wavelength of the radiation.

$$A_R = \frac{G_R \lambda^2}{4\pi} [m^2] \tag{2.22}$$

Multiplying the effective area by the power density S_T, the power received by the receiving antenna is obtained (***equation 2.23***). The use of this equation will be presented in the following chapters to sensibly set the gain on the receiving antenna.

$$P_R = \frac{P_T G_T G_R \lambda^2 \sigma}{(4\pi)^3 d^4} [W] \tag{2.23}$$

Angle of Arrival

FMCW radar systems equipped with multiple receiving antennas can also estimate the arrival angle (AoA) of the received signal, exploiting the phase variation between signals reflected by the same obstacle on the different receiving antennas. In ***figure 2.11***, an example case is represented with two receiving antennas placed at a distance d and an object with an angular position of θ concerning the radial position. In this configuration on the Rx2 antenna the evaluated distance will be increased by an addend $d\ sin(\theta)$ and therefore the antennas will have a phase shift of $\Delta\phi$ (***equation 2.24***).

$$\Delta\phi = \frac{2\ \pi\ d\ sin(\theta)}{\lambda} \tag{2.24}$$

Rewriting the equation as a function of θ we obtain the equation (***equation 2.25***) that describes its behavior. Being a non-linear equation, the sensitivity of θ with respect to $\Delta\phi$ is not constant but rather it is maximum for θ angles close to 0 while it reduces for θ which tends to $\frac{\pi}{2}$.

$$\theta = sin^{-1}(\frac{\lambda\Delta\phi}{2\pi d}) \tag{2.25}$$

The resolution on θ (***equation 2.26***) is also dependent on the θ angle, increasing for θ which tends to zero, and on the number of receiving antennas N, a factor that increases the resolution.

$$\Delta\theta = \frac{\lambda}{N\ d\ cos(\theta)} \tag{2.26}$$

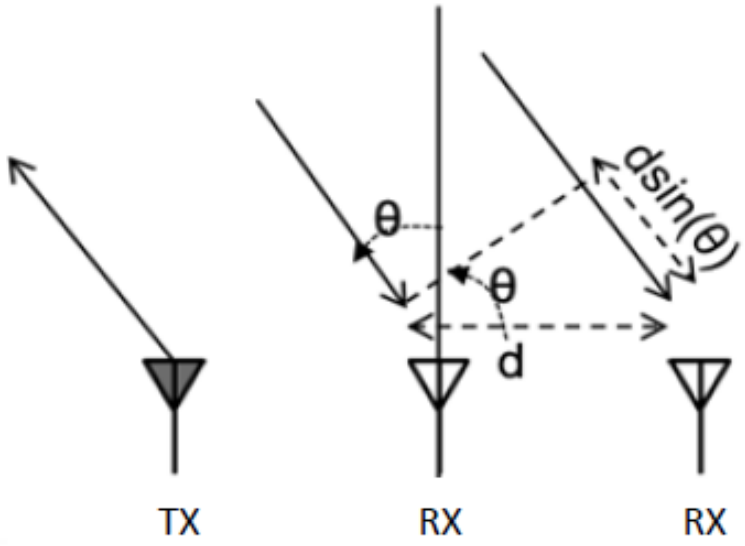

Figure 2.11: Angle of Arrival [16].

The maximum angle that defines the radar's field of view is defined in ***equation 2.27*** and depends exclusively on the λ wavelength and the distance between the antennas d [16].

$$\theta_{max} = sin^{-1}(\frac{\lambda}{2d}) \tag{2.27}$$

Velocity

As mentioned above, FMCW radars also allow you to evaluate the target's speed like Doppler radars, using two different processes. The first consists of the use of the Doppler frequency, which, however, is very often difficult to estimate and use. The second is to send two consecutive chirps spaced by a Δt interval and exploit the phase difference between the two signals to evaluate the target's speed. The phase of the signal, as reported in ***equation 2.5***, is directly proportional to the distance. A Δd shift results in a $\Delta\phi$ phase change. By inverting the equation in its differential form and relating it to the time interval between chirps, the velocity v is obtained, as reported in ***equation 2.28***.

$$v = \frac{\lambda\ \Delta\phi}{4\ \pi\ \Delta t} \tag{2.28}$$

Depending on the phase difference, in order not to have ambiguity due to the periodicity of the phase, we have a measurable limit speed. The phase shift must in fact be smaller than π and therefore the maximum measurable speed is reported

in ***equation 2.29***.

$$v_{max} = \frac{\lambda}{4\ \Delta t} \tag{2.29}$$

As regards the speed resolution, this is defined as the minimum speed variation measurable by the device. This value is obtained as in ***equation 2.30*** from the ratio between the λ wavelength and the product between double the time interval between consecutive chirps and the number of chirps in the same frame (N) [16].

$$\Delta v = \frac{\lambda}{2\ N\ \Delta t} \tag{2.30}$$

2.2 Power Spectral Density (PSD)

Power spectral density (PSD) is a mathematical measure of the frequency content of a given signal. It makes it possible to represent the distribution of different frequency components, facilitating the interpretation conveyed to DFT (Discrete Fourier Transform). It is used in various areas, from quantifying vibrations in mechanical systems to analyzing noise in electronics to quantifying scattering properties in optics. It is, firstly, necessary to start from the expression of the Fourier Transform in the time domain (***equation 2.31***) where $x(t)$ is a generic signal and $X(f)$ is its transform in the frequency domain f.

$$X(f) = \int_{-\infty}^{+\infty} x(t) e^{-j2\pi ft} dt \tag{2.31}$$

It is also necessary to remember the definition of energy E of a signal $x(t)$, given in ***equation 2.32***.

$$E = \int_{-\infty}^{+\infty} x(t)^2 dt \tag{2.32}$$

According to Parseval's relation, the total signal energy does not depend on the domain in which it is represented and is, therefore, the same in both time and frequency domains. This relationship, mathematically expressed in ***equation 2.33***, allows the energy of a signal to be related to its Fourier transform as given in ***equation 2.34***.

$$\int_{-\infty}^{+\infty} x(t)^2 dt = \int_{-\infty}^{+\infty} |X(f)|^2 df \tag{2.33}$$

$$E = \int_{-\infty}^{+\infty} |X(f)|^2 df \tag{2.34}$$

Recalling now the definition of the power of a signal as the ratio of its energy to the time support T on which it is calculated, we obtain the mathematical formulation in ***equation 2.35***.

$$P = \frac{E}{T} = \frac{1}{T} \int_{-\infty}^{+\infty} |X(f)|^2 df = \int_{-\infty}^{+\infty} \frac{|X(f)|^2}{T} df \tag{2.35}$$

At this point the limit for T goes to ∞ of the integrand of the function turns out to be just the definition of Power Spectral Density (PSD), ***equation 2.36***.

$$PSD = \lim_{T \to \infty} \frac{|X(f)|^2}{T} \tag{2.36}$$

Some properties of the PSD can be inferred from the definition:

- PSD a real function being defined as the square modulus of the Fourier transform;
- PSD is a positive function;
- Integrating the PSD yields the variance of the signal.

Relying on the Fourier transform and, in particular, the DFT (Discrete Fourier Transform) in our application since we work with discretized signals, the PSD offers a significant advantage. From theory, the Fourier transform of a finite signal returns a continuous function in frequency. Ideally, exploiting this property of the DFT and thus of the PSD conduce to infinite frequency resolution. In the use of FM radar, this potential of frequency analysis was exploited to increase the spatial resolution of the device by a factor of 30, achieving a spatial resolution of 1 millimeter. Using a computer to perform the Fourier Transform, particularly the Fast Fourier Transform, a low computational cost formulation, improves the resolution but also increases the variance of the PSD obtained. The variance increase turns out to be the significant difficulty of such an approach.

2.3 Breathing and heartbeat physiological models

The in and out of the lung's air movement consisting of two main phases, inhalation and exhalation, repeated alternately, is called lung ventilation. During inspiration, there is a contraction of two main muscle groups the diaphragm and the external intercostal muscles (***figure 2.12***). The former contracting moves inferior toward the abdomen, while the latter moves the ribs outward. This double contraction increases thoracic volume and lung volume, given the adhesive force of pleura's fluid between the lungs and pleura. This increase in volume results in a reduction of intra-alveolar pressure below the external atmospheric pressure allowing air to enter the lungs. Muscle contraction makes the inspiratory process active, while the exhalation process is generally passive. In fact, during exhalation, the elasticity of lung tissue and muscle relaxation contracts the lungs to the 'rest' position by increasing intra-alveolar pressure and promoting air exit. While breathing

at the alveolar level, there is a gas exchange between blood and air. The blood transfers carbon dioxide to the air and instead absorbs oxygen. This way, waste carbon dioxide is expelled through exhalation, and oxygen necessary for almost all metabolic reactions is introduced. Influencing and controlling the respiratory rate and depth of breathing are the respiratory centers in the brain that are stimulated by chemical and blood pH changes [22].

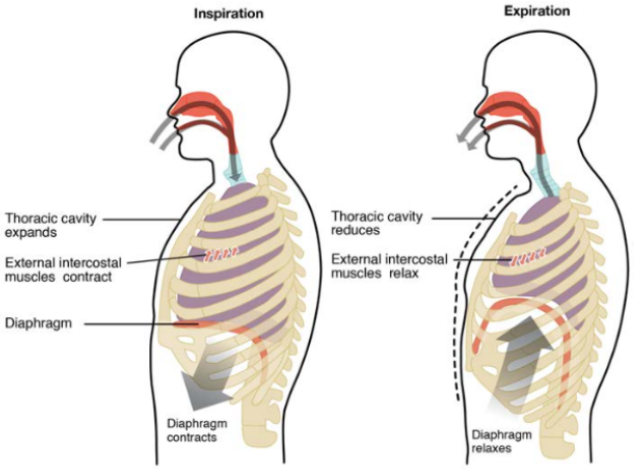

Figure 2.12: Breathing muscles effects [22].

Inside the rib cage is also the heart, located above the diaphragm with an apex near the anterior surface of the chest wall (***figure 2.13***). The heart is divided into two parts, right and left, each with a different task. The first pumps deoxygenated blood in the pulmonary arteries to the lungs for oxygenation. The second, on the other hand, pumps oxygenated blood through the aorta to all peripheral tissues and organs. Each part is then composed of two chambers, atrium and ventricle, of which the ventricle is the most significant portion and also the one of greatest interest. The rhythmic contraction of the heart, divided into the systole and diastole phases, begins in the atrial sinus (AS), where the pacemaker cells' contraction transmits the depolarizing electrical impulse to the rest of the heart cells. The diastole phases are those of contraction and blood pumping, while the systole phases are those of chamber filling. The vibration transmission up to the chest wall during contraction is interesting for this application.

Chest wall motion $x(t)$ is given, barring body movements, by the sum of the motion due to respiration $x_b(t)$ and the motion due to heartbeat $x_h(t)$, ***equation 2.37***.

$$x(t) = x_b(t) + x_h(t) \tag{2.37}$$

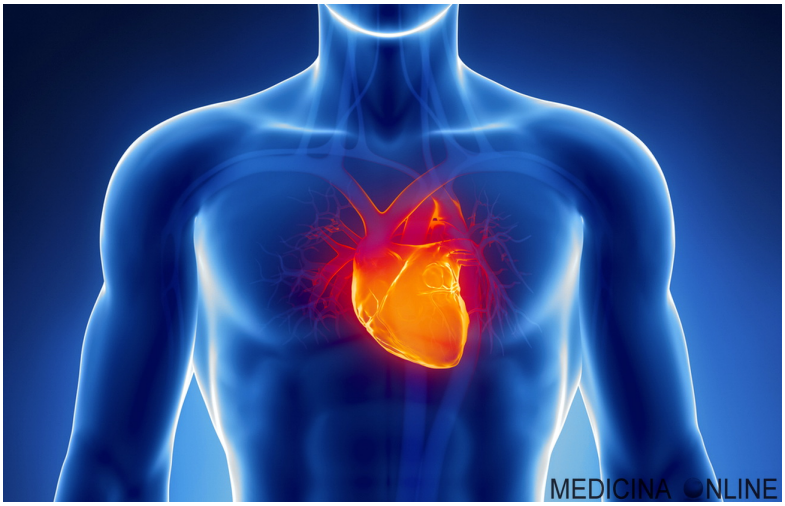

Figure 2.13: Heart chest's position.

The modeling of the two signals $x_b(t)$ and $x_h(t)$ can be of different types, considering or not various phenomena. In its simplest form, respiration can be modeled as a sinusoidal motion with an amplitude ranging from 4 to 12 millimeters and a resting frequency between 6 and 25 breaths per minute [2, 19]. The sinusoidal model, however, is not the most faithful as it does not consider the different duration of the two breathing phases. Inhalation is much faster and shorter than exhalation, which tends to be, during tidal breathing, slower (***figure 2.14***). The literature proposes visco-elastic tissue response models [18, 17, 23], more faithful to the actual thoracic motion due to breathing.

In a first approximation, breathing can be modeled with a sinusoidal pattern with 0.2 - 0.5 millimeters amplitude and 60 - 100 beats per minute frequency [6, 2]. Below 60 beats per minute is called bradycardia, while above 100 beats per minute is called tachycardia. The sinusoidal model, however, does not consider the cardiac mechanism's pulsatility. Other more complex models have been proposed, such as half-cycle sine pulses [24] or gaussian pulse train [25]. (***igure ??***) shows a representation of the different models.

2.4 Breathing analysis algorithm: state of the art

2.4.1 Time domain analysis

The first possibility for analyzing the respiratory signal is to study it in the time domain, that is, by going to identify the start and end phases of the respiratory

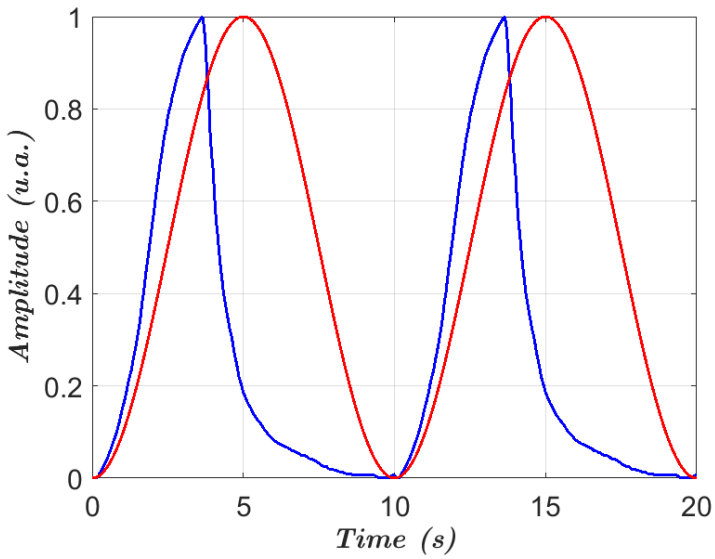

Figure 2.14: Comparison between sinusoidal breathing model and real chest breathing displacement.

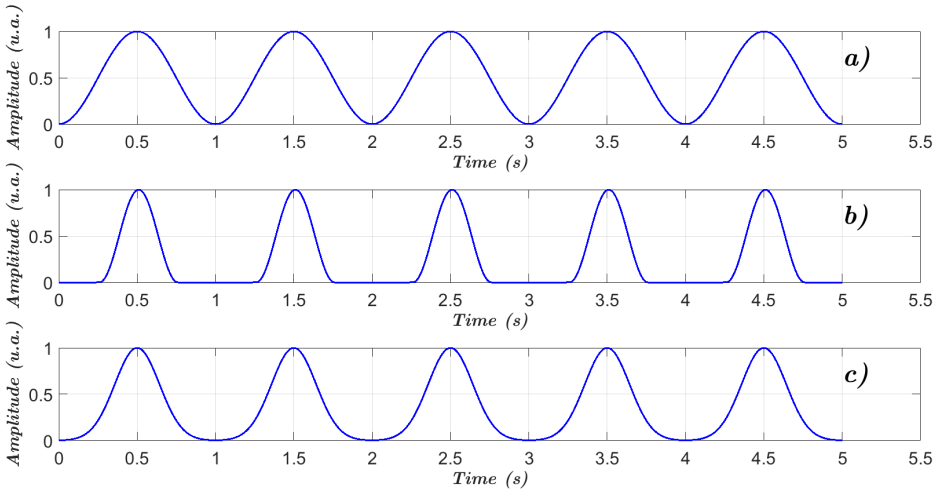

Figure 2.15: Comparison between sinusoidal beating (a), half-sinusoidal beating (b) and gaussian train beating (c) models.

cycle [26, 27, 28]. In this way, measuring the temporal duration of individual respiratory cycles and expressing them in frequency terms as breaths per minute is possible. This analysis requires working with the signal in the time domain after properly filtering them beforehand. The main advantage is that it does not require

splitting the signal into windows, as is the case with analyses based on the signal's frequency content. Based on the correct extraction of the instants of interest, this technique is susceptible to the quality of the source signal and the method of choice. An example of this analysis is shown in ***figure 2.16*** applied on actual data taken with the respiratory belt presented in the following chapters.

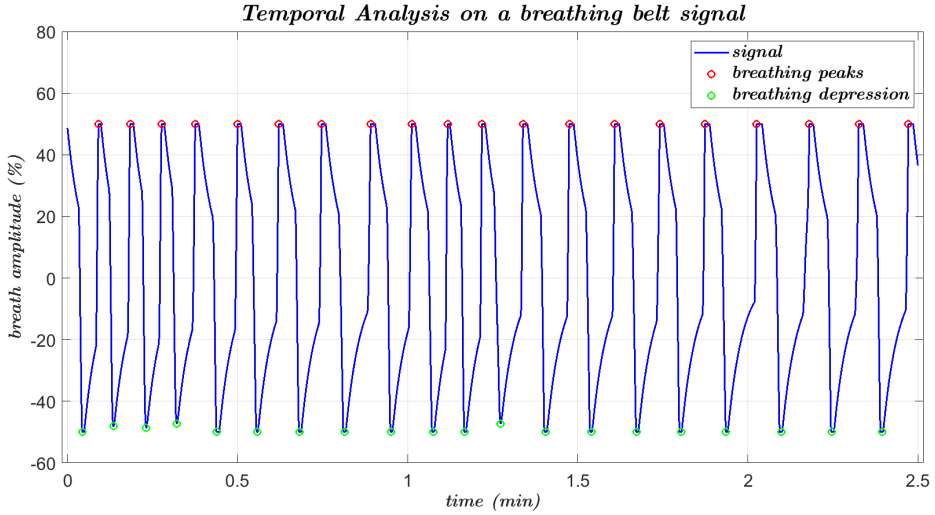

Figure 2.16: Example of temporal analysis on a biosignalplux breathing belt signal.

Within the analysis methods over time, Kalman filters are also used in some work [29, 24]. For the application under consideration, the Kalman filter is used to construct a model of the signal under investigation to compare and assess whether the newly extracted parameters align with the model. In this way, it is possible to follow the changes in the vital parameters with great rapidity and allow the exclusion of possible anomalies in the signals. The downside is related to the complexity and computational time in building the filter and using it, as it internally runs an iterative optimization cycle from the high computation time for a real-time application.

2.4.2 Frequency domain analysis

The respiratory signal can also be analyzed in the frequency domain. In this case, the signal is divided into windows of appropriate duration to the desired frequency resolution, remembering that the inverse of the time duration of the window in seconds gives the maximum frequency resolution. A transformation, such as the Fourier Transform, is applied on each window to pass into the frequency domain. The peak in frequency in the band of interest, i.e., between 5 and 40 breaths

per minute (83 to 667 mHz) for tidal respiration, corresponds to the respiratory rate. Frequency analysis for a periodic signal is a robust method. During tidal respiration, the breath is assimilated to a periodic signal; therefore, the frequency analysis turns out to be robust and reliable. It turns out, however, to be a less powerful analysis during speech because the thoracic motion due to breathing is less periodic. ***Figure 2.17***, shows a 20-second window of a real respiratory signal and the corresponding PSD whose peak corresponds to the respiratory rate evaluated on the specific window.

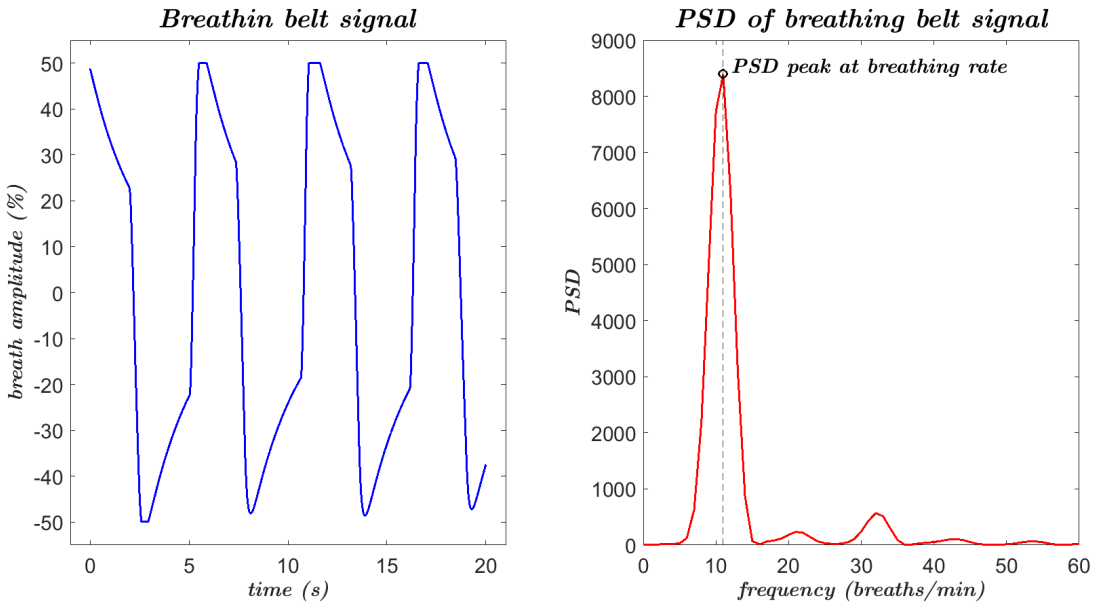

Figure 2.17: Example of frequency analysis on a biosignalplux breathing belt signal.

Frequency analysis for radar applications has been extensively studied in the literature because it allows for robust analysis that is less complex than other techniques and has a reduced computational burden. For these reasons, frequency analysis is also well suited for real-time applications. Specific to radar applications, frequency analysis is conducted with different techniques depending on the type of radar. Most studies, in any case, use Doppler radars by studying separately the in-phase and quadrature components of the received signal [30, 12, 31, 32, 33, 6, 34, 35].

2.4.3 Independent Component Analysis (ICA)

Independent Component Analysis (ICA) is a processing methodology aiming to decompose a non-Gaussian signal into its statistically independent basis components.

The analysis is based on finding the linearly dependent basis components that produce the analyzed signal. Linear dependence is an effective assumption in many applications in the biomedical field. In addition, the variables are assumed to be statistically independent of each other, and while this assumption is also very stringent, it allows many application problems to be solved effectively. Given a signal x generated by a mixing process from several sources, according to the model, it can be described as the linear combination of several s_i components, each with its own weight a_i. This formulation is also given in ***equation 2.38*** in its vector form.

$$x = \sum_{i=1}^{N} a_i s_i = As \tag{2.38}$$

Taking advantage of the assumption that the sources are independent of each other and have a non-Gaussian distribution, it is possible to calculate the coefficients of the A matrix. Calculating its inverse and knowing the signal x, the independent components s [36, 37] are extracted. This type of analysis has also been used on radar data to extract from the individual's distance signals the subject's respiratory rate [10].

2.4.4 Principal Component Analysis (PCA)

Principal Component Analysis is a technique that analyzes a data set in which several dependent variables describe each observation to represent them with a new set of orthogonal variables. Extracting these new variables, called principal components, coincides with identifying important information within the dataset. PCA also makes it possible to compress the size of the dataset while keeping the information content unchanged or nearly intact but reducing the complexity of subsequent processing. Obtaining the new variables is based on maximum variance and orthogonality. The first component is selected as the one with maximum variance and, therefore, maximum inertia, with which most information content is associated. Subsequent ones are chosen as orthogonal to the previous ones and always have maximum possible variance [38]. Techniques of this type have also been detailed in signal processing techniques for extracting the construct variables of a given signal or multiple signals. Indeed, they have also been used in the biomedical field to extract vital parameters from radar data, as described in [9].

2.4.5 Variational Mode Decomposition

Variational Mode Decomposition is a signal processing technique aiming to decompose a signal into its main modes. The basic algorithm identifies maxima and

minima recursively and estimates envelopes to interpolate these points, removing averages and considering high frequencies as a separate mode of disturbance. The result of the decomposition is highly dependent on the method of identifying the points of interest and the stopping criterion of the iterative optimization algorithm. The assumption about the basic modes, which allows the algorithm's convergence, is that the modes are band-limited. For many biomedical applications, this assumption is easily satisfied since biological and noise signals generally have a specific frequency definition that has already been verified in the literature. Several variants differ in the point identification method, and mode extraction [39]. Since they are also quite complex iterative algorithms, they generally have a high computational cost with long run times compared to other analysis techniques. VMD has also been used in analyzing respiratory signals from radar data as proposed in [40].

Chapter 3

Device

The radar used is the BGT60ATR24C, a 60 GHZ FMCW radar sensor (***figure 3.1***). Infineon developed it as part of a European project involving the Polytechnic University of Turin. It has a bandwidth of 4 GHz that can range from 58 to 63 GHz. It consists of two Tx transmitting antennas and four Rx receiving antennas to work in the MIMO regime. It also features optimized power modes for low-power consumption.

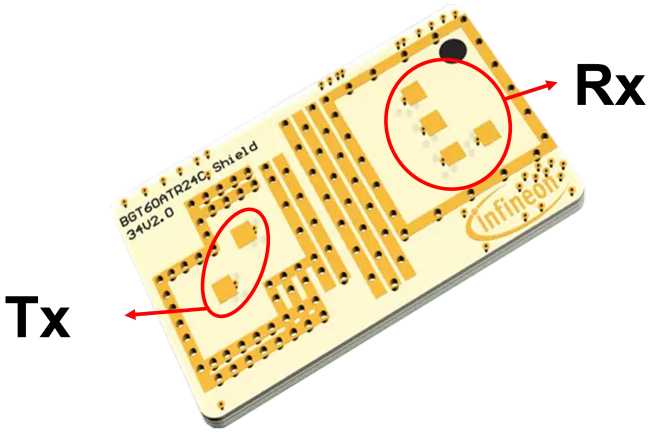

Figure 3.1: BGT60ATR24C radar image.

Figure 3.2 shows the functional block diagram taken from the device datasheet [41]. It can be divided into several basic components such as:

- RF Frontend, consisting of two transmitting antennas (Tx), four receiving antennas (Rx) and a voltage-controlled oscillator (VCO);

- Analog Baseband (ABB), consisting of a high pass filter (HPF), an anti-aliasing filter (SFF) and a VGA;
- Phase-locked loop (PLL), a third-order electronic circuit to generate the chirp ramp with the correct frequencies;
- Multiplexed Analog-to-Digital Coverted (MADC), composed of 4 channels of 12 bits differential SAR ADCs interfaced to the ABB via a driver and to the FIFO via a mux;
- Single Analog-to-Digital Converted (SADC), 8 to 10 bits single-ended SAR ADC used to sense the sensor data;
- first-in-first-out (FIFO) of 196 kbit;
- Serial Peripheral Interface (SPI), up to 50 MHz clock;
- Finite State Machine (FSM), which manage the complete chip;
- Clock wise, 80 MHz system clock (SYS CLK) domain for PLL, MADC, SADC; 50 MHz SPI clock for FIFO; SPI clock The main FSM syncs those two domains.

3.1 Setting Parameters

There are two ways to interface with the device. The first is to take advantage of the Infineon Toolbox provided by the manufacturer (***figure 3.3***). This interface allows setting all the specifications of interest. The tool carries out the entire processing chain from the raw data, and it is then possible to save the data from a specific recording and process it later in post-processing. The tool was used extensively in the first phase of the work to understand how the radar works and begin to interface with it. It allows you to set which and how many antennas to use, chirp parameters, both spatial and velocity resolutions, and even working ranges. It is a potent tool. However, this type of approach has two problems. The first is the inability to work in real-time and test the algorithm's performance, especially from the point of view of execution timing. It would not be allowed to test how well the algorithm can keep up with the arrival of data from the radar. The second issue is related to spatial resolution. The tool sets the maximum spatial resolution, the theoretical one obtainable (about 3 cm) with the FFT without switching to the apparent resolution. This resolution would not be sufficient for the application of interest, so it was necessary to use one of the other two interface options, using Matlab or C programming.

Given the greater familiarity with the Matlab language, we choose it. In addition, through App Designer, it was possible to develop a GUI that worked in real-time

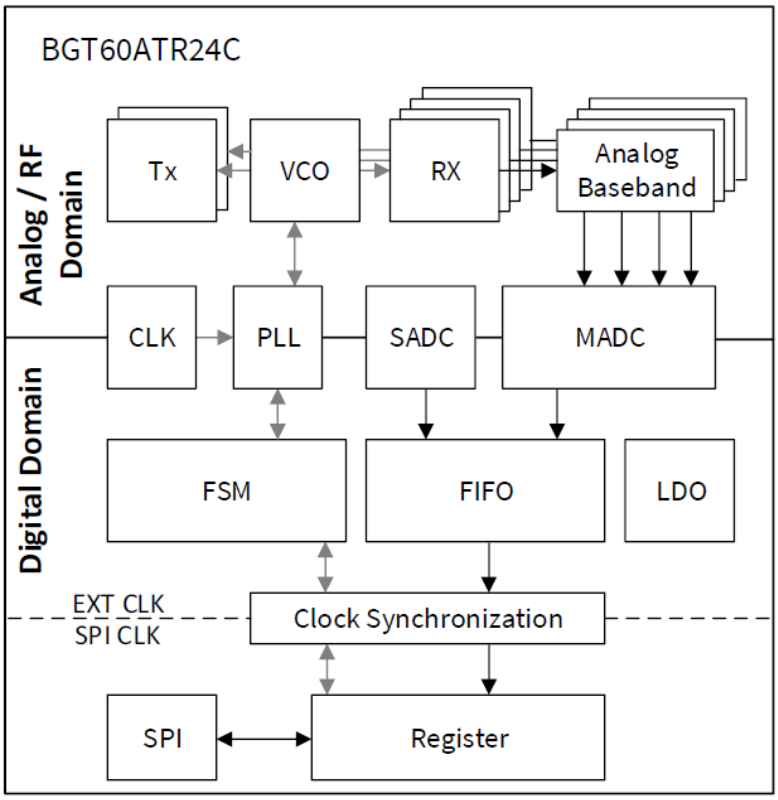

Figure 3.2: BGT60ATR24C functional block scheme [41].

and from which set all the radar parameters of interest. Through this second option, the number of parameters to be set is less intuitive than the Infineon tool but more controllable. The parameters are:

- **Rx mask**, Bitmask where each bit represents one RX antenna of the radar device. If a bit is set the according RX antenna is enabled during the chirps and the signal received through that antenna is captured. The least significant bit corresponds to antenna 1;
- **Tx mask**, allows you to set which and how many of the two receiving antennas to use. Bitmask where each bit represents one TX antenna;
- **Tx power level**, this parameter allows you to adjust the power of the emitted signal. It is a dummy parameter adjustable from 0 to 31, by default it has a value of 31;
- **If Gain dB**, Amplification factor that is applied to the IF signal coming from the RF mixer before it is fed into the ADC. By default it is set to 33, but can go up to a maximum value of 60;

Figure 3.3: Radar GUI interface.

- **Lower Frequency**, is the lower frequency of the chirp ramp in Hz;
- **Higher Frequency**, is the higher frequency of the chirp ramp in Hz;
- **Number of samples per chirp**, is the number of points with which the chirp is sampled and together with the sampling rate governs the duration of the chirp;
- **Sampling rate (fc)**, allows the sampling rate in Hz of the ADC to be set up to a maximum of 2.5 MHz. This parameter together with the number of samples per chirp allows setting the duration, ***equation 3.2***.

$$T = \frac{Number\_of\_samples\_per\_chirp}{fc} \tag{3.1}$$

  The duration of the chirp determines the maximum working distance of the radar, ***equation 3.2***, where c is the velocity of light.

$$Max\ distance = \frac{c\,T}{2} = \frac{Number\_of\_samples\_per\_chirp\ c}{2\ fc} \tag{3.2}$$

- **Chirp Repetition Time (CRT)**, is the time interval between successive chirps. This value must be greater than the duration of chirp T;

- **Number of chirps per frame**, is the number of chirps to be emitted within the frame. This number must be less than the duration of the frame divided by the CRT. It is also possible to set a limited number of chirps in the frame that will be executed in succession at the beginning of the frame and then enter a stand-by phase;
- **Frame**, is the duration of the frame expressed in seconds;
- **MIMO**, is the working mode of the radar (0 = SIMO, 1 = MIMO).

3.2 Characterization

The features observed in the radar are proposed below. The characterization phase was performed by following a different method than by going through several tests with the radar at different distances and with targets of different sizes and shapes.

3.2.1 Low distance noise

Since the radar, as seen in ***figure 3.1***, has the emitting and receiving antennas very close together (about 1 centimeter), there is high-intensity noise due to interference between the two. Several signal sampling tests were performed under different conditions so that the effect of interference between antennas on the signals of interest could be evaluated. For all tests, the radar was mounted on the tripod with the appropriate stand and positioned at a predefined distance from the wall, ***figure 3.4***. The system recorder raw radar data over two minutes to select a frame far from the radar switching. In ***figure 3.5***, four average PSDs performed on a 1-second duration frame composed of 2000 distinct chirps are shown. The first test refers to an unloaded condition, i.e., in the absence of a detectable target in the radar analysis field. Thus, the only contribution appears due to interference noise between antennas. On the other hand, the second test was carried out by positioning the radar at 10 centimeters so that the frequency contribution given by the wall reflection fell in the band of interest to the interference noise. The same test was performed at a wall-radar distance of 20 centimeters. Finally, the last test was carried out at a distance of 50 centimeters from the wall to compare spectral noise contribution versus the signal of interest obtained from the reflection on the target under a condition of frequency separation.

From ***figure 3.5*** it is possible to observe the differences in the spectrum as the radar-target distance varies. In the absence of targets, the only signal source is the short-distance noise between antennas placed very close together. Tests were performed at varying distances. At a distance of 10 centimeters, the signal reflected from the wall overlaps with the short-distance noise, significantly increasing its

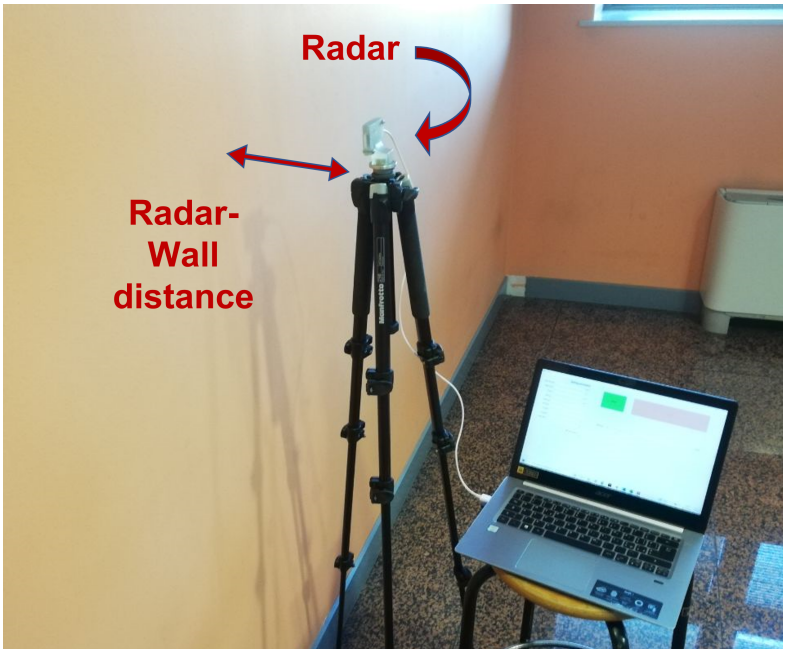

Figure 3.4: Radar-Wall setup.

amplitude in the spectrum compared with the noise alone. However, this increase is not selectively located at the corresponding distance but increases the entire spectrum due to multiple reflections. In the case of a wall-radar distance of 20 centimeters, the power increase at the correct distance is more appreciated. In this case, however, it can be observed that a smooth and ideally infinite object, having a wall much larger than the radar field of view, produces a reflection comparable to the noise and not much greater. At 50 centimeters distance, it is observed that the noise at a short distance persists, but a new contribution also appears at the corresponding distance. The actual distance evaluated is slightly less than 50 centimeters; however, given the resolution of the radar, it is reasonable. With this last example, the magnitude of the short-distance noise is well appreciated. As a result of these analyses, it was chosen to introduce a filter that would remove from the raw radar data the frequencies lower than that corresponding to 30 centimeters to eliminate the noise contribution due to interference between antennas completely.

3.2.2 Target Loss

The team encountered this specific problem during some analyses conducted with the 3D printer. In the present case, we simulated a sinusoidal respiratory motion withan amplitude of 20 millimeters and a frequency of 20 breaths per minute.

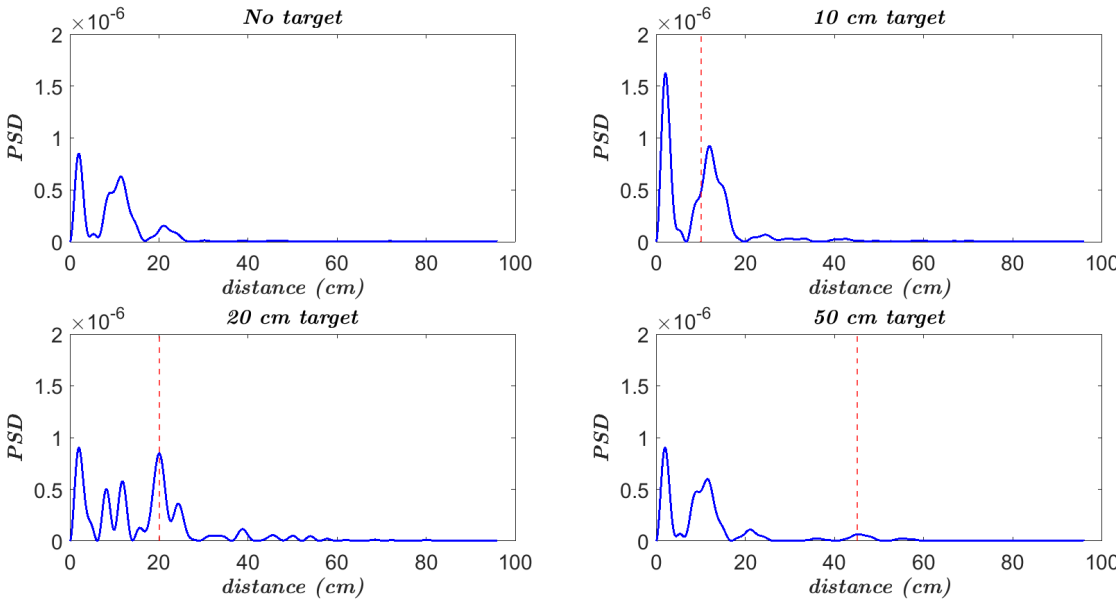

Figure 3.5: Different radar-wall distance PSD. Firstly without any target while the others at 10 - 20 - 50 centimeters.

By analyzing the distance signal extracted by the algorithm (***figure 3.6***), it is observed that the sine wave is correctly centered around the radar-target distance of 33 cm. For some time instants, it saturates at a distance of about 35 or 38 cm. Two chirps(A and B) corresponding to instants of correct and incorrect detection have been analyzed to understand the behavior (***figure 3.6***). It is well observed from the two graphs that in the case of correct detection (A) there is a central component in the signal at a frequency corresponding to about 33 cm. In the case of incorrect detection (B), on the other hand, such a component, although the condition is the same and the target is always at that distance, the previously detected peak is not present but is confused with the noise. The simple search for a maximum within a signal still produces an output that does not correlate with the object's location. This analysis led to an increase in the complexity of the distance extraction algorithm.

3.2.3 Chirp distribution in the frame

During device characterization, an open problem was the distribution of chirps within the frame. The frame duration can be set as greater than the product of number of chirps and CRT. This feature required understanding how the distribution of chirps occurs in the frame to understand how to properly set the number of

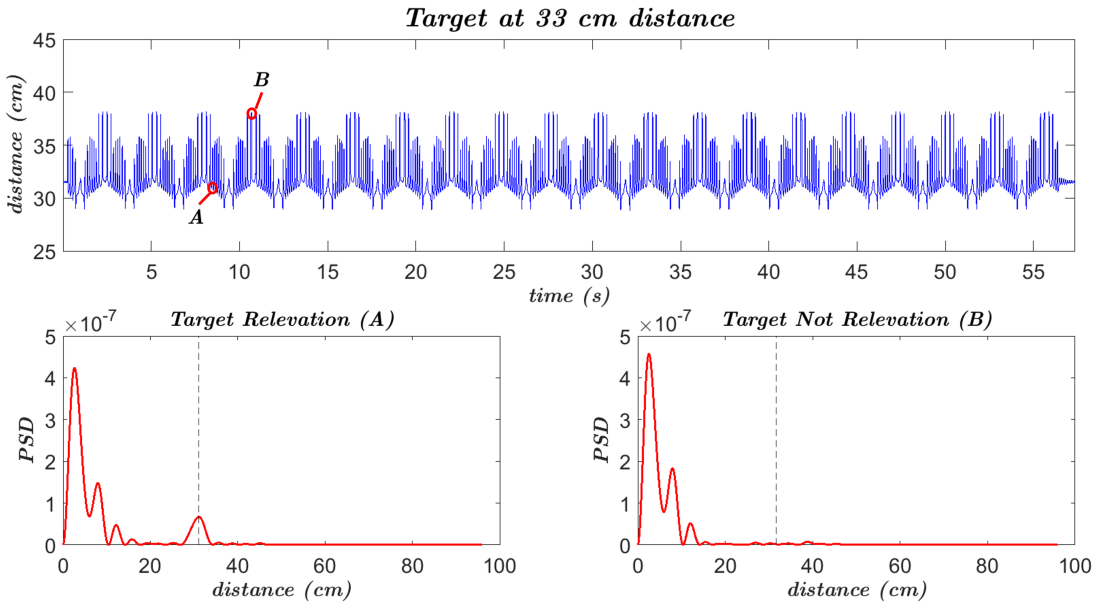

Figure 3.6: Target loss example.

hirps. To do this, a movement with the 3D printer of a total duration of 20 seconds was simulated, in which after 10 seconds, the cardboard mounted on the printer makes a receding movement. A 20-second duration frame was set on the radar with a number of chirps and a CRT that multiplied would give only 4 seconds. If the distribution was uniform, motion should have been identified from the frame analysis. If instead the chirps were sequenced then only the first position set by the programmed motion would be seen. As observed in ***figure 3.7***, the condition is the second in that a0only one reference position is identified demonstrating that the chirps are sent consecutively. This feature forced the value of the number of chir per frame to be set as high as possible so as to have continuity in the analysis of the subject's position.

3.2.4 Negligible Doppler effect

The Doppler effect occurs when a signal impinges on a moving body, which changes the frequency of the reflected signal. The magnitude of this frequency component is equivalent to the ratio of $2vf_T$ and c, where v is the body's velocity, f_t is the incident wave frequency, and c is the velocity of the radiation. To estimate the Doppler component in the application under consideration, consider the center-band frequency of the radar, 60 GHz, as the f_T frequency. In contrast, the velocity is estimated to be the maximum during normal breathing. Putting ourselves in the most stringent conditions, we assume shortness of breath with a respiratory rate

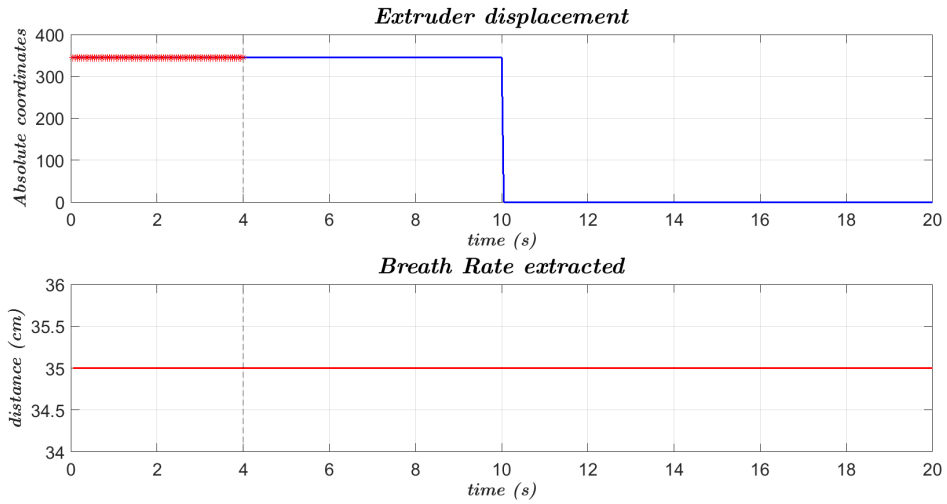

Figure 3.7: Target loss example.

of 60 breaths per minute such that each breath has a time support of one second. Assuming that the inspiratory act, the one with the shortest duration, corresponds to 30 % of the respiratory act, you have a period of 300 ms. Again to put ourselves in a limiting condition, assume an expansive breath, 12 millimeters in amplitude, so that the velocity identified is reasonably the maximum possible. Under these conditions, the mean chest velocity equals 0,04 m/s, ***equation 3.3***.

$$v = \frac{s}{t} = \frac{12\ mm}{300\ ms} = 0{,}04\ m/s \tag{3.3}$$

The corresponding Doppler frequency has a value in the order of tens of Hz, ***equation 3.4***.

$$f_D = \frac{2vf_T}{c} = \frac{2\ 0{,}04\ m/s\ 60\ GHz}{299792458\ m/s} = 16\ Hz \tag{3.4}$$

Assume a frequency analysis of a radar signal with the following parameters: sampling frequency 2,5 MHz, BW 5 GHz, and 64 samples per chirp. An object at a distance of 30 centimeters would produce a signal with a frequency of about 400 kHz, ***equation 2.17***. Comparing the two values shows that the Doppler effect is negligible in the application discussed here and with this specific radar used in CW mode and, therefore, not taken into account during the algorithm design.

3.2.5 Transferred power analysis

The on-body propagation of electromagnetic waves in the 60 GHz band is characterized by many peculiar characteristics, including large reflection and absorption due

to the strong dielectric contrast between the skin permittivity and free space, and high atmospheric attenuation caused by the resonant oxygen-induced absorption and a power reflection coefficient typically close to 40% for normal incidence [42]. These are the major limitations of using this 60 GHz technology for long-range space analysis. According to measurements conducted in [43], the expected penetration depth into human skin is estimated at 0,48 millimeters. For the shallow penetration into human tissues, the body surface can be modelled as a unique skin layer with a complex permittivity ϵ_{skin} (***equation 3.5***) described with the following values, $\epsilon_r = 7.98$ and $\sigma = 34.6 S/m$ [44]. ϵ_0 is the vacuum permittivity, and omega is the pulsation of the electromagnetic wave.

$$\epsilon_{skin} = \epsilon_r - j\frac{\sigma}{\omega\epsilon_0} \tag{3.5}$$

According to [31], the permittivity of cotton clothes is significantly smaller than the skin's one, $\epsilon_{r,cotton} \approx 1$, so the radiated signal will mainly be reflected at the patient's upper skin layer. The IEEE maximum allowed exposures for frequencies over $2000 MHz$ is $10 W/m^2$ [45, 46]. As analyzed in [47], there is no safety risk from the electromagnetic radiation produced by standard microwave radar sensors.

Chapter 4

Algorithm

The following chapter describes in detail the algorithm proposed by the following thesis project. The general operation is first presented in its essential components, which will then be examined individually and in detail.

4.1 MATLAB GUI

To run the real-time algorithm, a GUI was produced using App Designer, the Matlab tool for developing applications. ***Figure 4.1*** shows the GUI graphic consisting of three main parts: the parameter setting to program the radar, the data processing section, and the section to save the results to an external Matlab file.

The 'Setting Parameters' section consists of a button (Set Parameters) and nine text boxes for entering parameters for programming the radar. These parameters are not the same as those given in ***chapter 3.1***, as parameters have been chosen that are easier for the user to use and understand. For each parameter that can be entered in the GUI, radar parameters are calculated internally. The parameters that can be entered to program the radar are:

- **dist_max (m)**, which is the maximum working distance of the radar expressed in meters;
- **delta_d (m)**, which is the desired spatial resolution expressed in meters. This parameter will be used to define the number of points over which to perform the PSD;
- **fc (Hz)**, which is the sampling frequency of the ADC with which the signal output from the mixer is sampled;

Figure 4.1: Matlab GUI graphics.

- **CRT (s)**, which is the time distance between successive chirps expressed in seconds;
- **frame (s)**, which is the duration in seconds of each frame;
- **Rx mask**, which is the binary mask with which to encode the emitting antennas;
- **Tx mask**, which is the binary mask with which to encode the receiving antennas;
- **Tx power**, with which to define the 'Tx power level' parameter;
- **Gain (dB)**, with which to define the 'if_gain_dB' parameter.

Finally, the 'Set Parameters' button allows to set radar parameters and enables the start of data acquisition. The processing section has the function of acquiring the raw data from the radar, processing it, and showing the results through different graphical components. This section consists of two buttons (START and STOP), four LEDs, two cartesian graphs, and one polar graph. The START button starts the whole processing algorithm by acquiring the first frame. The four LEDs, on the other hand, have specific functions: calibration shows that the algorithm is in the process of searching for the subject, 'Low Quality' is turned on when the signal is of poor quality, 'Fixed' is turned on when a stationary object is detected, 'Human', on the other hand, is turned on when a human subject is detected, and then vital

parameters will be plotted in the different graphs. The three charts, however, have different purposes. The polar graph shows the position of the detected object so that the user can verify that it is indeed the subject. Of the two cartesian graphs, on the other hand, the first shows the value of the breath rate over the last 20 seconds while the second shows the displacement of the patient's chest in the previous 20 seconds. The STOP button terminates the acquisition and enables the save section of the results. The save section contains a text box to enter the file name and a button.

4.2 General Description

Figure 4.2 shows the high-level block diagram of the algorithm in its essential components. The entire process begins following the setting of parameters to program the radar correctly. Then when the START button is pressed, the middle section of the algorithm begins. This section consists of a cyclic repetition of several steps. The first is the retrieval of the frame from the radar buffer. Here, a check is made to verify that the pickup is performed at a one-time interval later than the previous pickup, equal to the frame's duration. This check is entered to construct the time axis and avoid pickup errors correctly. Following data acquisition, two different routines can be performed. The first is the subject search routine. In this routine, radar signals are frequency analyzed, targets present are recognized, and the human subject, if present, is identified. This verification phase has a twofold purpose. The first is to focus the subsequent vital-parameter analysis solely on the subject's location, reducing computational cost and time. The second is to avoid analyzing a non-human target by providing parameters of no integrity. This routine is repeated until a human subject is detected, alternating periods of analysis with periods of rest and waiting. Throughout the routine, the 'Calibration' LED lits on to indicate the search phase of the algorithm. On the other hand, the second routine begins following the human subject's detection. The subject's vital parameters are extracted and plotted in the appropriate graphs at this stage. Several situations can occur during this phase. First, the subject leaves the field of view, and the identified target is static. This condition is shown to the user by the illumination of the 'Fixed' LED. Although the target is recognized as human, the signal is of insufficient quality to extract vital parameters, and in this case, the 'Low Quality' led lits. On the other hand, if everything is proceeding as best as possible and the vital parameters are correctly identified the 'Human' led is kept on. The whole process continues cyclically until the STOP button is pressed. At this point, acquisition and processing are stopped, and the saving of results is enabled. It is then allowed to type the name of the file to which the data is to be saved, and pressing the SAVE button generates the Matlab file with the chosen

name. Subsequent chapters detail all the steps described above, describing how parameter selection, processing, and saving occur.

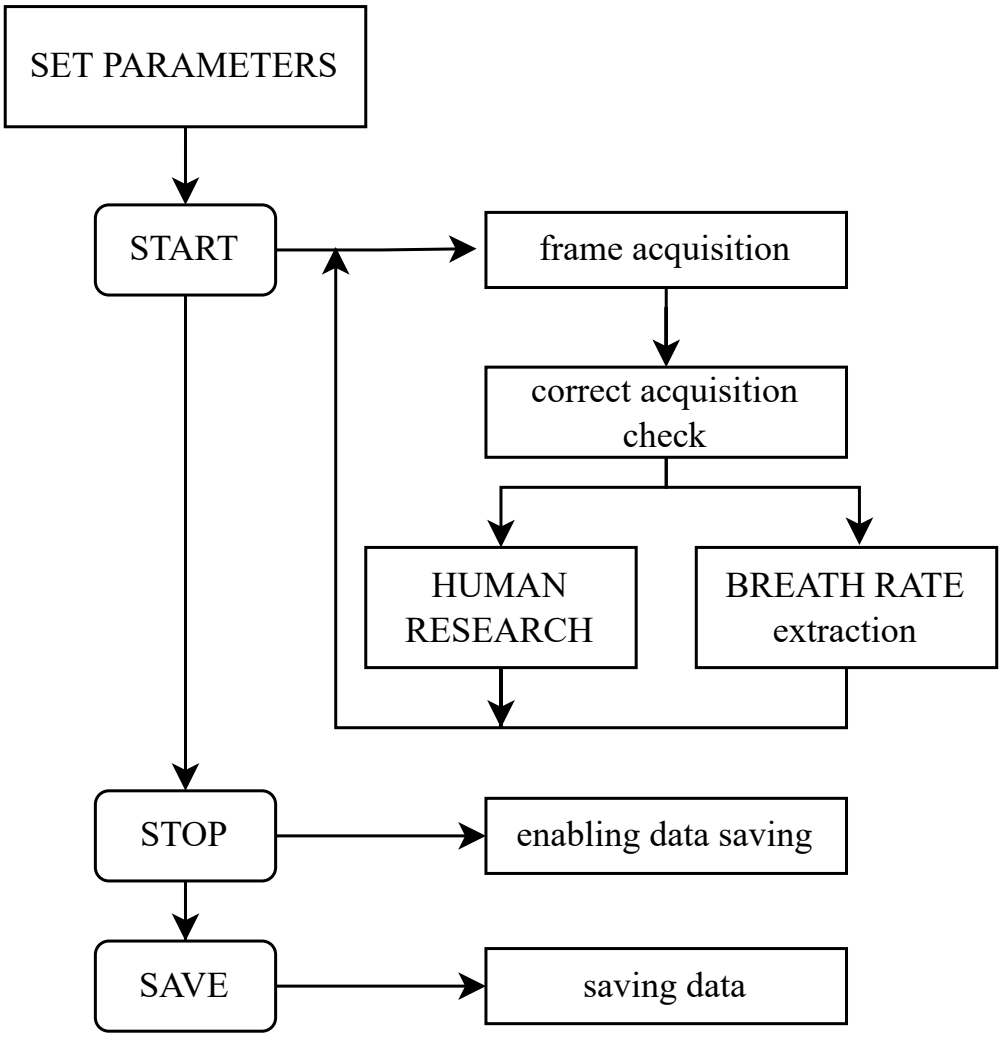

Figure 4.2: High-level algorithm block diagram.

4.3 Set Parameters

This section discusses the operations involved in the initial GUI settings and programming and connection operations with the radar. ***Figure 4.3*** shows the flowchart of the operations that occur at this stage. The first instructions performed are the start-up instructions that include disabling all buttons except the 'Set Parameters' button and the graphical settings of the different plots. The graphical

settings include the title, axis names, plot position, and limits to the axes where present. Suggested values are also printed on the screen in the text boxes for the parameters, which are modifiable by the user. Input and modification of the parameters in the text boxes are registered. The radar-related object is created when the 'Set Parameters' button is pressed. The radar parameters, in some cases different from those on the screen, are then set. The relationship between the parameters is presented in the sub-chapter of this section. The connection with the radar is then made, and the START button is enabled if there are no errors. This operation concludes the first phase of the algorithm.

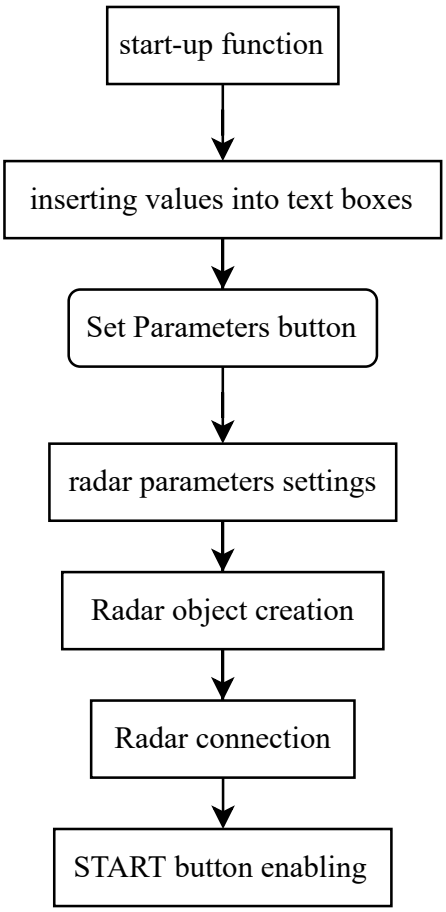

Figure 4.3: Parameter settings flowchart.

4.3.1 Radar programming

Table 4.1 shows on several columns the parameters that can be entered through the Matlab GUI and the parameters to program the radar correctly. The analysis

to go from the former to the latter and the corresponding calculations performed are given below.

Table 4.1: GUI and radar parameters comparison.

GUI parameters	Radar parameters
dist_max(m)	Number of samples per chirp
delta_d (m)	Lower Frequency
	Higher Frequency
fc (Hz)	Sampling rate (Hz)
CRT (s)	CRT (s)
frame (s)	frame (s)
	Number of chirps per frame
Rx mask	Rx mask
Tx mask	Tx mask
Tx power	Tx power level
Gain (dB)	If Gain dB
	MIMO

The parameters 'dist_max' and 'delta_t', as seen above, refer to the maximum desired distance and the desired spatial resolution expressed in meters. These two parameters, together with the sampling frequency 'fc' directly entered by the user, are used to calculate the parameters 'Number of samples per chirp', 'Lower frequency', and 'Higher Frequency' to program the radar as follows. Starting from ***equation 2.17***, which defined the IF frequency as $\frac{2Sd}{c}$, with S slope of the chirp, d the distance of the target and c speed of light, we rewrite it in terms of the maximum calculable frequency. Since the sampling rate is set to 'fc', the maximum computable IF signal frequency is worth $\frac{fc}{2}$ to avoid aliasing. ***equation 4.1*** then describes the relationship between maximum fIF, maximum distance, and sampling rate, taking into account the definition of slope as the ratio of BW to chirp duration T_{chirp}.

$$IF_{max} = \frac{fc}{2} = \frac{2Sd}{c} = \frac{2\ B\ d_{max}}{c\ T_{chirp}} \tag{4.1}$$

Rewriting the equation as a function of maximum distance yields ***equation 4.2***, which describes the relationship between maximum distance, spatial resolution and number of samples per chirp.

$$\begin{aligned} d_{max} = \frac{c\ T_{chirp}\ fc}{4B} = \frac{c}{2B}\frac{T_{chirp}\ fc}{2} = \frac{c}{2B}\frac{Number\ of\ samples}{2} \\ = \Delta d\frac{Number\ of\ samples}{2} \end{aligned} \tag{4.2}$$

To calculate the number of samples per chirp, it's enough to invert the formula, ***equation 4.3***.

$$Number\ of\ samples = \frac{2\ d_{max}}{\Delta d} \tag{4.3}$$

The spatial resolution in the formula Δd, however, cannot simply be replaced with the one entered by the user 'delta_t' because, while the user has no constraints, the theoretical one has the limit of $ris_{max} = \frac{c}{2BW_{max}}$. Thus there are two possibilities, if the spatial resolution entered is greater than the maximum one then there is a simple parameter substitution, while if it is less then the maximum one is used for the calculations, ***equation 4.4***.

$$\Delta d = \begin{cases} delta\_d, & \text{if } delta\_d >= ris_{max} \\ ris_{max}, & \text{if } delta\_d < ris_{max} \end{cases} \tag{4.4}$$

The same duality in the calculation of the number of samples per chirp occurs in the calculation of BW, ***equation 4.5***.

$$BW = \begin{cases} \frac{2delta\_d}{c}, & \text{if } delta\_d >= ris_{max} \\ BW_{max}, & \text{if } delta\_d < ris_{max} \end{cases} \tag{4.5}$$

From the BW calculation, the lower frequency and higher frequency of the chirp can be calculated as in ***equation 4.6***, where B_0 is the central frequency of the chirp.

$$lowerfrequency = B_0 - \frac{BW}{2} \quad \text{and} \quad higherfrequency = B_0 + \frac{BW}{2} \tag{4.6}$$

Frame and CRT values are directly set as entered by the user and are also used to define the number of chirps per frame as a ratio of the two quantities, ***equation 4.7***.

$$Number\ of\ chirps = \frac{frame}{CRT} \tag{4.7}$$

The parameters of Rx mask, Tx mask, Tx power level, and If Gain dB is set as entered by the user. In contrast, the MIMO parameter is entered by default equal to 0 since it is desired to work with a single transmitting antenna and a single receiving antenna. All these relationships are checked so that the accounts add up and there is no conflict between the variables. The correct values are printed on the screen after pressing the 'Set Parameters' button.

4.4 START - elaboration

Figure 4.4 shows the flow chart of the middle section of the algorithm, which is the signal processing section.

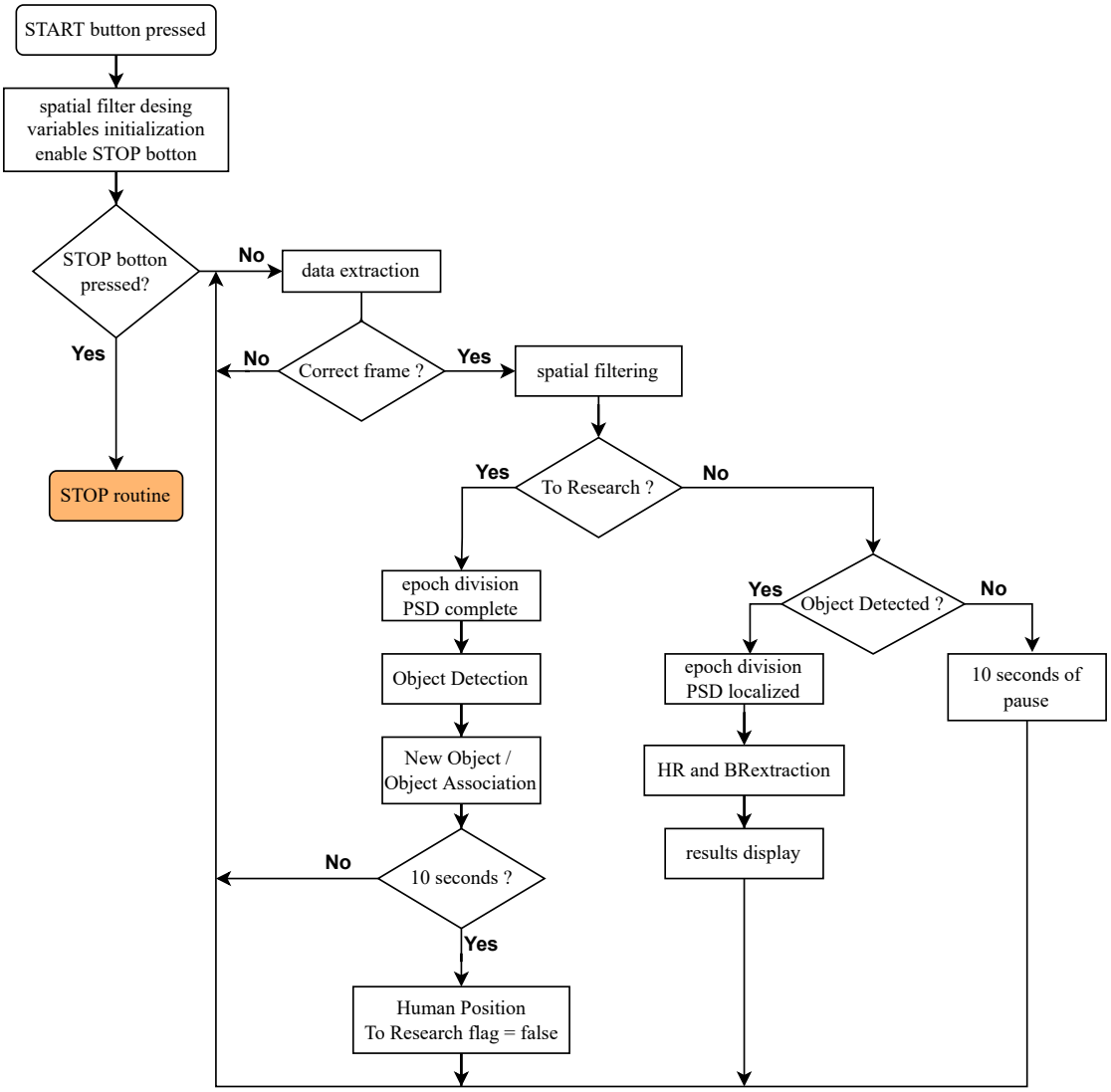

Figure 4.4: Start flowchart.

After pressing the START button following the settings operations, there is a first initialization phase. As the first operation, the spatial filter design necessary to remove short-range noise is done. A Butterworth filter with a cutoff frequency equal to the equivalent of 25 centimeters is implemented to be sure to remove all interference noise. This technical choice reduces the working distance of the radar by imposing it more significantly than 25 centimeters. Next, several variables useful for the analysis are initialized, and the STOP button is enabled so that the analysis can be stopped when desired. The central while loop is the one that governs the entire processing and begins with the extraction of the frame from the

radar buffer. At this level, many checks are performed to verify that the signal is sampled correctly. The first check is performed at the instant of data extraction. If the interval between the previous extraction and the current one deviates more than 5% from the set frame duration, then that specific frame is discarded. This type of verification is necessary to construct a consistent and verifiable time axis of radar data. If, for example, a 1-second frame was taken after 3 seconds from the previous one, it would not be possible to refer the chirps to a specific temporal instant, and the whole analysis would have no real meaning, risking distortion of the thoracic signal. When the frame has been correctly extracted, the radar data are extracted, and spatial filtering is performed to remove interference noise between antennas. At this point, three scenarios are opened: the first is related to the target search phase, the second is associated with the detection of the target believed to be non-human, however, and the third is associated with the detection of the target believed to be human. The three different scenarios present different signal processing by having other purposes. During the first iteration, the designated scenario is the first one. The entire field of view of the radar is scanned for targets, associating for each chirp packet the position of an object with the correct target, assuming that at this stage, the subject is relatively stationary. After the target search phase is complete, positions over time are saved for each, and these signals are analyzed to detect, if present, the subject. If all detected targets are found to be inanimate, then a resting phase is carried out for a certain amount of time (10 seconds) so as not to overload the system, and then the target detection phase is started again. If, on the other hand, a human target is detected, then the extraction of vital parameters and their display is carried out. At this stage, moreover, the focus is solely on the subject to follow as it moves. This upgrade makes possible future development possible in which the radar is mounted on a servomotor or mobile mechanism and rotates following the subject's movements within the environment, making its field of view "unlimited" 360°. The three scenarios are explored in detail in the following sub-chapters by going into the details of the different processing. The entire process is repeated iteratively until the STOP button is pressed, which terminates the operations.

4.4.1 Target Research

This section describes the portion of the algorithm designed for object detection. Its main function is to analyze the spectrum extracted from the radar data and perform an analysis to identify the presence of objects in a given time frame T, set to 10 seconds. The positions of the targets are entered into a framework assuming that they remain stationary during the analysis period. This procedure has two main purposes, the first is to identify whether or not there are targets of interest, and the second is to monitor their behavior so that at a later time, we can assess

whether the target is a physical person or a stationary object such as a wall, a bed, for example. In future developments, this approach allows monitoring not a single subject but multiple subjects detected at different distances and angles, using the radar in SIMO or MIMO mode. In ***Figure 4.5***, the specific flowchart of this section is shown.

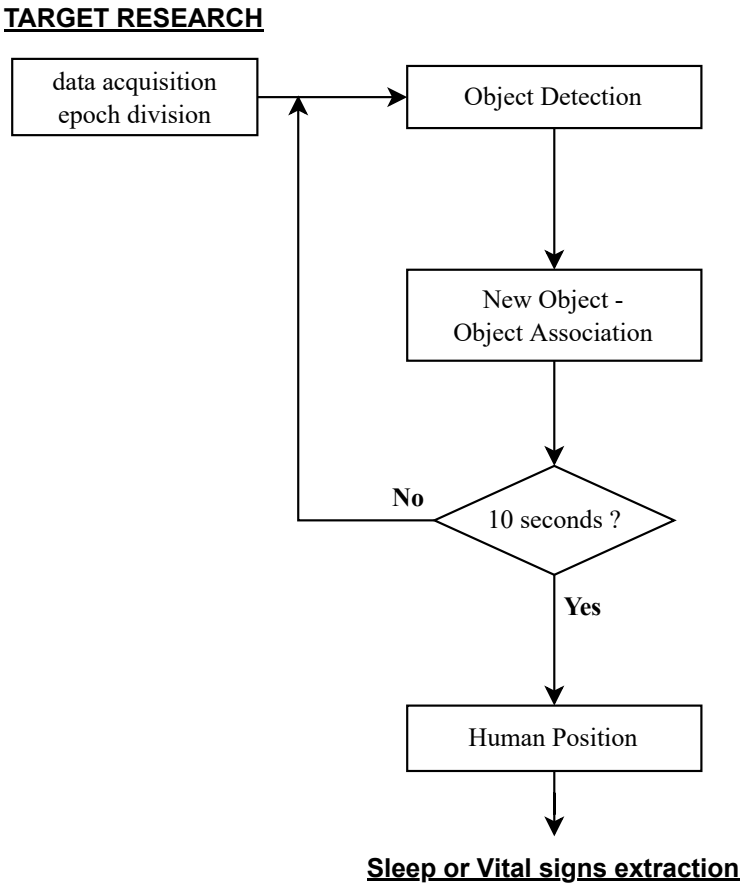

Figure 4.5: Target research flowchart.

The first operations is the data acquisition. Next, each chirp is analyzed individually in the 'Object detection' routine. This section has the function of processing the data packet, performing its PSD, extracting its peaks with sufficient power to be considered objects and not noise, and finally detecting its position at high resolution. The output of this routine, a vector containing the positions of the detected targets for the specific packet, is provided as input to the next routine, 'New Object - Object Detection'. The purpose of this second section is to associate each position with its corresponding target to monitor its movement.

The sub-routine 'New Object' is called in two conditions, at the first entry into the section for the first identification of targets and in case a new target appears in observation period T. On the other hand, the subroutine 'Object Association' is used to associate the detected positions with the corresponding targets correctly. After the interval T has elapsed, the detected positions for each target are analyzed, looking for the subject, if present. If this is detected, vital parameter extraction is performed, while if all detected targets are found to be nonhuman, then a refractory rest period is entered, reducing consumption. The three main routines, 'Object Detection,' 'New Object-Object Association,' and 'Human Position,' are discussed in more detail below.

Object detection

As mentioned earlier, this routine deals with analyzing the raw data from the radar to identify the targets present. As can be observed in ***Figure 4.6***, the data coming out of the radar are organized in a matrix having along the rows the samples of each chirp and for columns, the different chirps composing the frame.

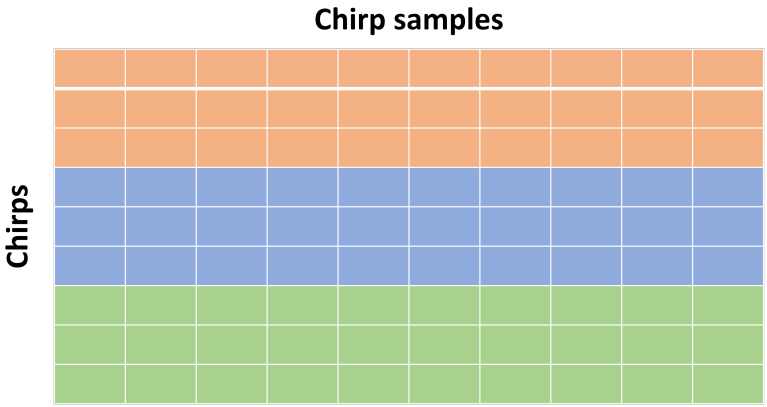

Figure 4.6: Radar data matrix.

Each chirp is analyzed as follow. A PSD calculation is performed on each chirp with a resolution twice the theoretical maximum obtainable, i.e., with a spatial resolution of about 6 cm. This choice is related to the fact that in the application of interest, the target is the human thorax, which certainly has a larger size than the spatial resolution used. A routine called 'Gaussian Division' is performed on the signal extracted with such a PSD, which is used to identify all potential targets in the curve. From the spectrum, it identifies maxima of them and for each identifies the previous and next minimum to divide the spectrum into its different contributions, ***Figure 4.7***. Once the contribution extremes are identified, integration is performed for each, then divided by the total power to extract each

strength. If the amplitude is greater than 20 %, the contribution is considered a target of interest; otherwise, it is discarded. We experimentally verified the choice of this threshold with several tests performed with the 3-D printer with cards of different sizes to obtain a reasonable value that was neither too sensitive nor too stringent. Suppose the contribution is found to be a target. In that case, the corresponding position is calculated, and a second PSD is performed, this time at high resolution, to accurately identify the actual position of the target of interest. This distance value is inserted within the output vector that will be provided as input to subsequent routines.

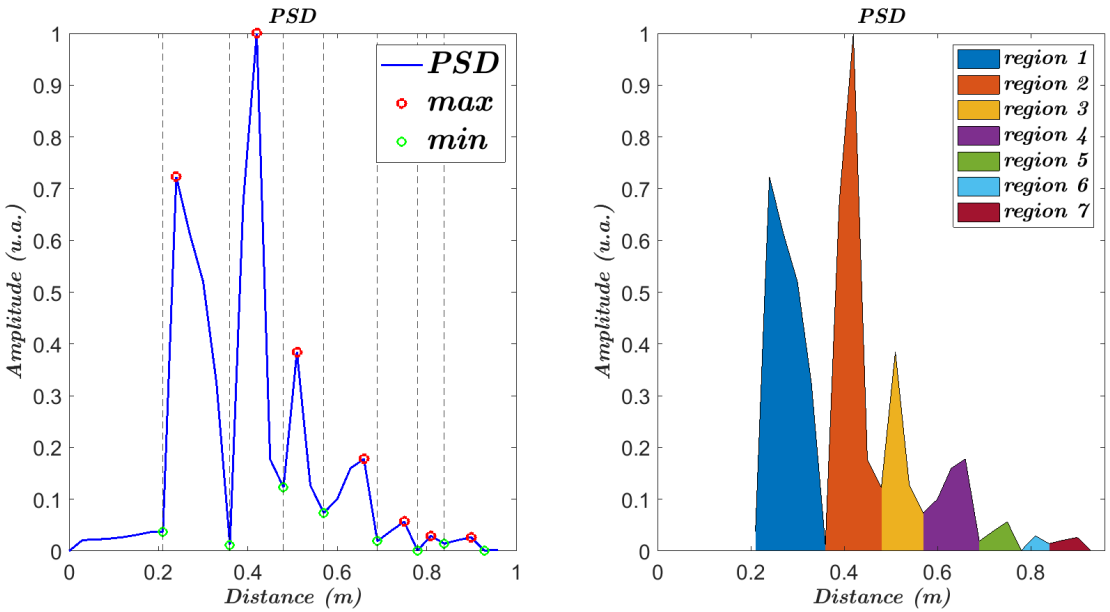

Figure 4.7: Gaussian division example. On the left is shown a PSD with its maximum values and the corresponding minimum value. On the right the same PSD array with the potential targets division.

New Object-Object Association

The 'New Object - Object Association' routine takes as input the vector containing the positions of the targets detected by the 'Object Detection' routine and compiles the structure called 'tracks' with the positions of each object detected. The track's structure consists of two variables for each instance, such as 'ID', which is an object identification number. The vector 'positions' where the position values associated with that specific object are stored, ***Figure 4.8***. This structure is initialized as empty. When a new object is detected, it is added to the structure with a new ID.

In contrast, the positions vector, initialized as a NaN vector, is updated with the detected position. The association between position and object is performed as follows. For each position, a check is performed on all previously detected targets. A limit velocity of the bodies under consideration is in the beginning defined. In this way, if the new position deviates by a Δ_d greater than the product of the maximum velocity and the time interval, then that position cannot be associated with that specific target. If the new position differs from the last detected position by a delta d less than this value, it is associated with the target; otherwise, analysis proceeds on the remaining targets. If it is not associated with any of them, the 'New Object' function is called, creating a new object. An evolution of the tracks' structure is shown in ***Figure 4.8*** as an example.

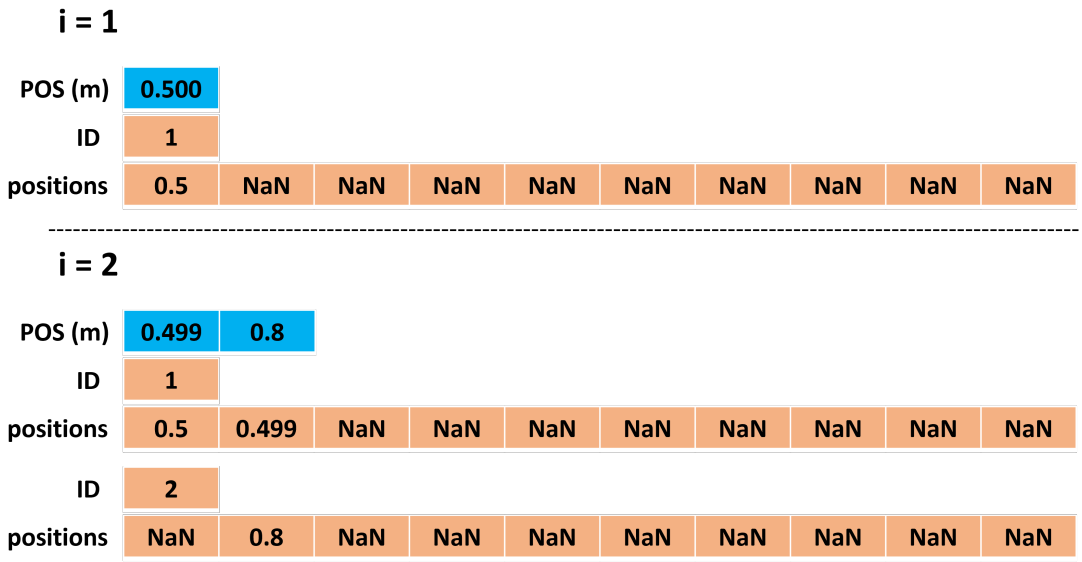

Figure 4.8: Tracks refilling example.

Human Position

The following routine, the flowchart of which is shown in ***figure 4.9***, contains the operations that are carried out to discriminate whether the target under consideration is the subject or not.

As a first operation, the design of a low-pass Butterworth filter with a cutoff frequency of 40 breaths per minute (about 667 mHz) is carried out, which will be used to filter the signal only in the band of interest. Then for each target identified, the vector of positions taken is extracted, and a count is made of how many NaN are present in the vector. The presence of a NaN means that the radar did not detect the target for the corresponding time instant. If the total number of NaN is

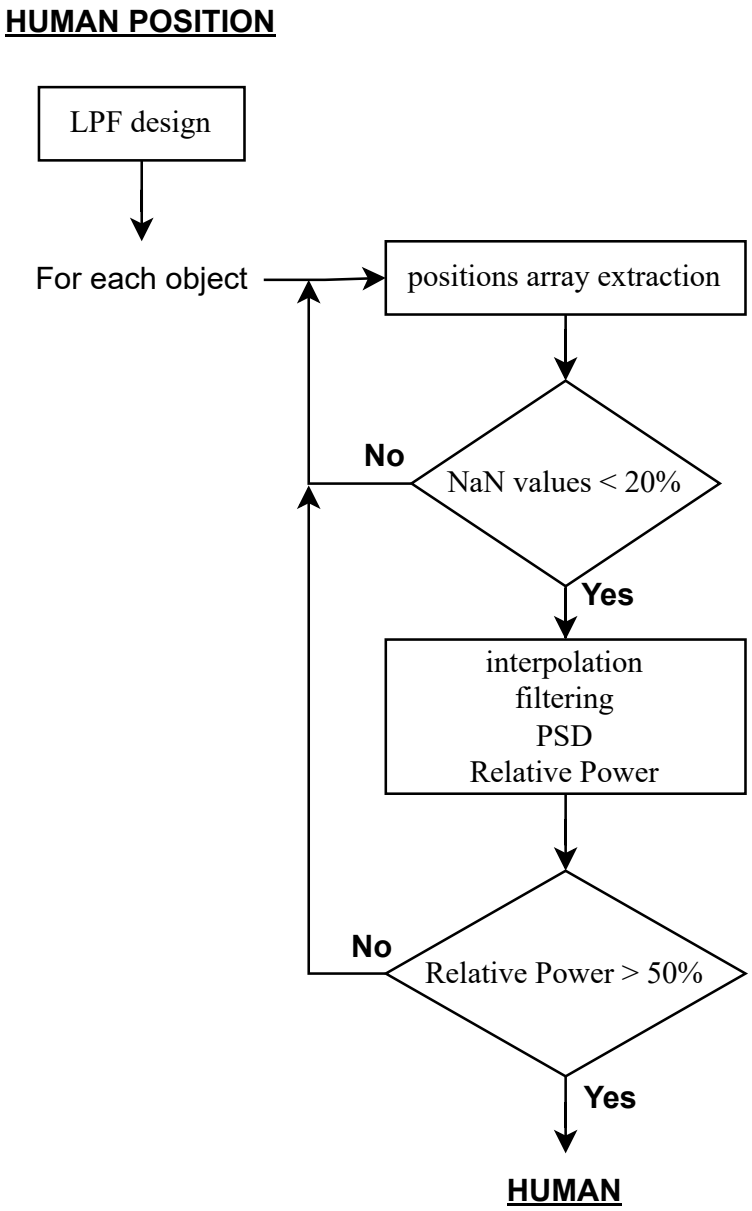

Figure 4.9: Human position flowchart.

greater than 20 % of the signal length, then that target is excluded because the signal quality is not high enough. Signals that exceed the check then this is linearly interpolated to remove the NaN values and replace them with numerical values. An example of such interpolation is shown in ***Figure 4.10***. In this example, on the left is shown raw data with some NaN samples (red lines), while on the right,

the final result after interpolation is shown. The interpolated signal is then filtered with the filter designed at the beginning of the routine to exclude frequencies beyond the band of interest set lower than 40 breaths per minute. The threshold choice is dictated by the literature. Normal respiration is defined up to this value, beyond which it is called accelerated respiration. Following filtering, a PSD of the signal is performed, taking as frequencies over which to calculate the PSD those corresponding to 0, 5, 10, 15, 20, 25, 30, 35, and 40 breaths per minute. The partial power contained in the 20 - 40 breaths per minute band is evaluated against the total power contained between 0- 40 breaths per minute. If the relative power is greater than 50% and the total amplitude is greater than 4 millimeters, the target is considered human. This type of processing is used to discern between a fixed target and a human target. If the target is fixed, most of the power is contained in the lower band of the signal, given the very slow fluctuations of the signal, while if the subject is human, then most of the power is contained in the respiratory band, as observable in ***figure 4.11***.

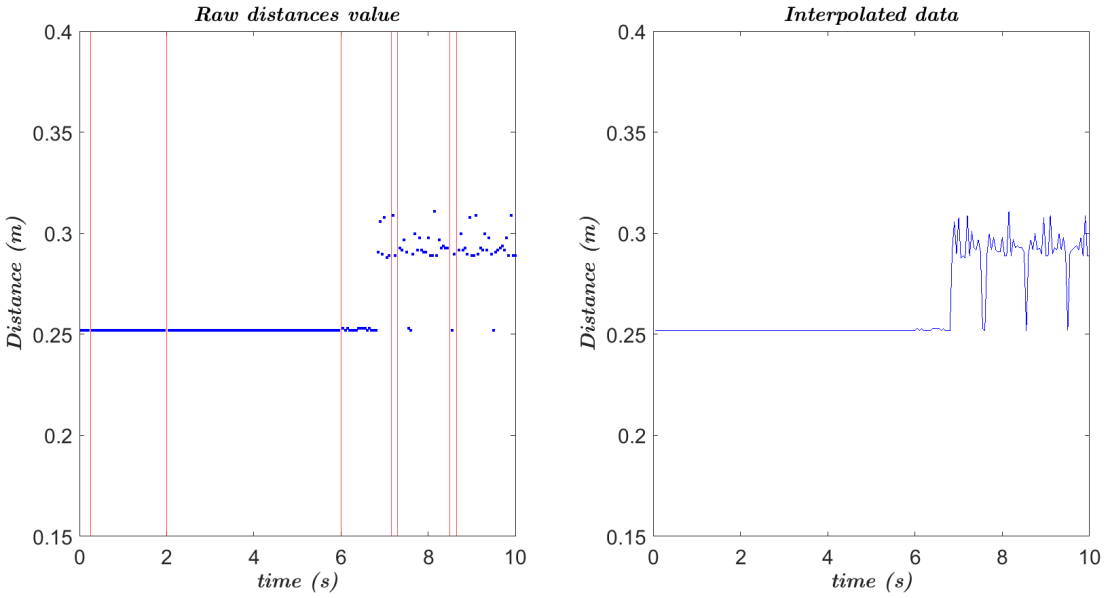

Figure 4.10: Interpolation example.

4.4.2 Vital parameters extraction

After the subject has been identified and its location identified, vital parameters are extracted. The entire process is shown graphically in the flowchart presented in ***figure 4.12***. After acquiring the data, each chirp is analyzed individually. The first operations refer to the evaluation of the instantaneous position of the subject. From

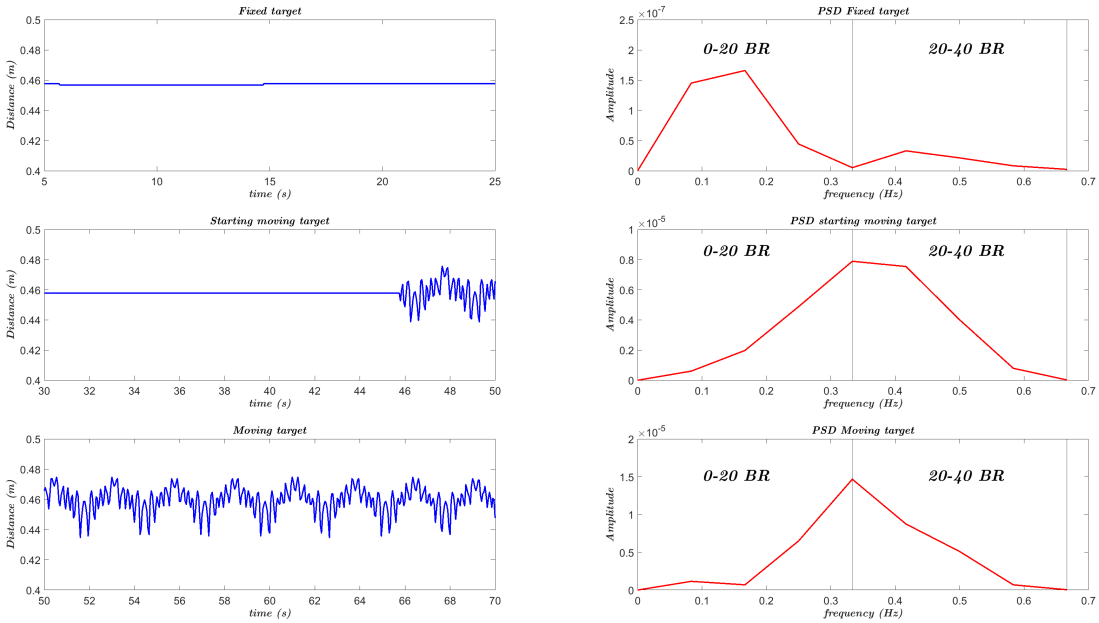

Figure 4.11: Fixed vs Human PSD comparison.

the raw data, a PSD is performed this time at high resolution but centered only in the frequency band related to the previous position ± 4 centimeters. This reduces computational time by avoiding performing the analysis over the entire spectrum while knowing the subject's position a priori. From the spectrum, the maximum is identified, and that is taken as the subject's current position by adding that value to the vector of positions. These operations are repeated for all component chirps in the frame. When the entire frame has been analyzed, extraction of the breathing rate is performed. The vector containing the positions occupied by the subject extracts the last 20 seconds of data. The signal is under-sampled with a median filter to 100 Hz in order to reduce noise, remove undetected chirps, and avoid filtering distortion. After that, a PSD has first performed again with a resolution corresponding to 1 breath per minute, as depicted in ***figure 4.13***. From the spectrum, the maximum is extracted, and this value is taken as the instantaneous respiratory rate. Several checks are performed on this extracted value to make sure that the figure is correct and reasonable. Before presenting this analysis, however, two variables that are used for this analysis must be introduced. The first is a Boolean vector called 'BRconsecutive' consisting of 5 values, all initialized to false. If the value of respiratory rate is deemed reliable, then the last value is set to TRUE, and the others shift one position back, while if the value is considered incorrect, then the last value is set to FALSE. The others turned accordingly. The following steps will clarify its function. The other variable was named 'lastBR' and

is essentially the last estimated value of respiratory rate. Later descriptions will explain its function.

Resuming the analysis, the checks made on the extracted breathing frequency value are as follows. First, we check that this value is greater than 4, which is the minimum frequency found in the literature for a resting respiration rate. If it is higher, a second check is made by comparing this value with the previous value contained in 'lastBR,' since such sudden changes in respiratory rate are not expected. If the respiration rate value passes both checks, it is considered reliable, and a TRUE is added to the 'BRconsecutive' array. If, on the other hand, it does not pass either condition, it is considered unreliable. However, if there is at least one TRUE value in the 'BRconsecutive' vector, then the current respiratory rate value is estimated to be equal to the previous one. If by frame, in fact, the quality of the signal should be lost, the algorithm continues to work, assuming that the respiratory rate has not changed. Suppose such loss of quality is prolonged for a duration of more than five frames. In that case, the respiratory rate value is set to NaN, and notified to the user is that the quality is too poor to allow correct and reliable estimation. If the output of the estimation routine, the respiratory rate value, is a number, graphs in the GUI are updated with the display of respiratory rate over the last 30 seconds, chest wall motion over the last 20 seconds, and the mean radial position assumed by the subject as verification of correct identification. On the other hand, if the value is non-numeric, the routine is aborted, and the LED notifying the user of poor quality turns on.

4.5 STOP and SAVING

When the STOP button is pressed, the iterative cycle is exited. The distance estimation and vital parameter extraction operations are then stopped. The SAVE button is enabled to allow the user to save the results of the analysis. A MATLAB file (.mat) saved with the name corresponding to the name entered in the 'filename' text box is generated. Specifically, the saved data are as follows:

- Frame sampling instants;
- Vector of respiratory frequencies;
- Distance sampling rate (given by the inverse of the time resolution set);
- Radar ADC sampling frequency;
- Frame duration.

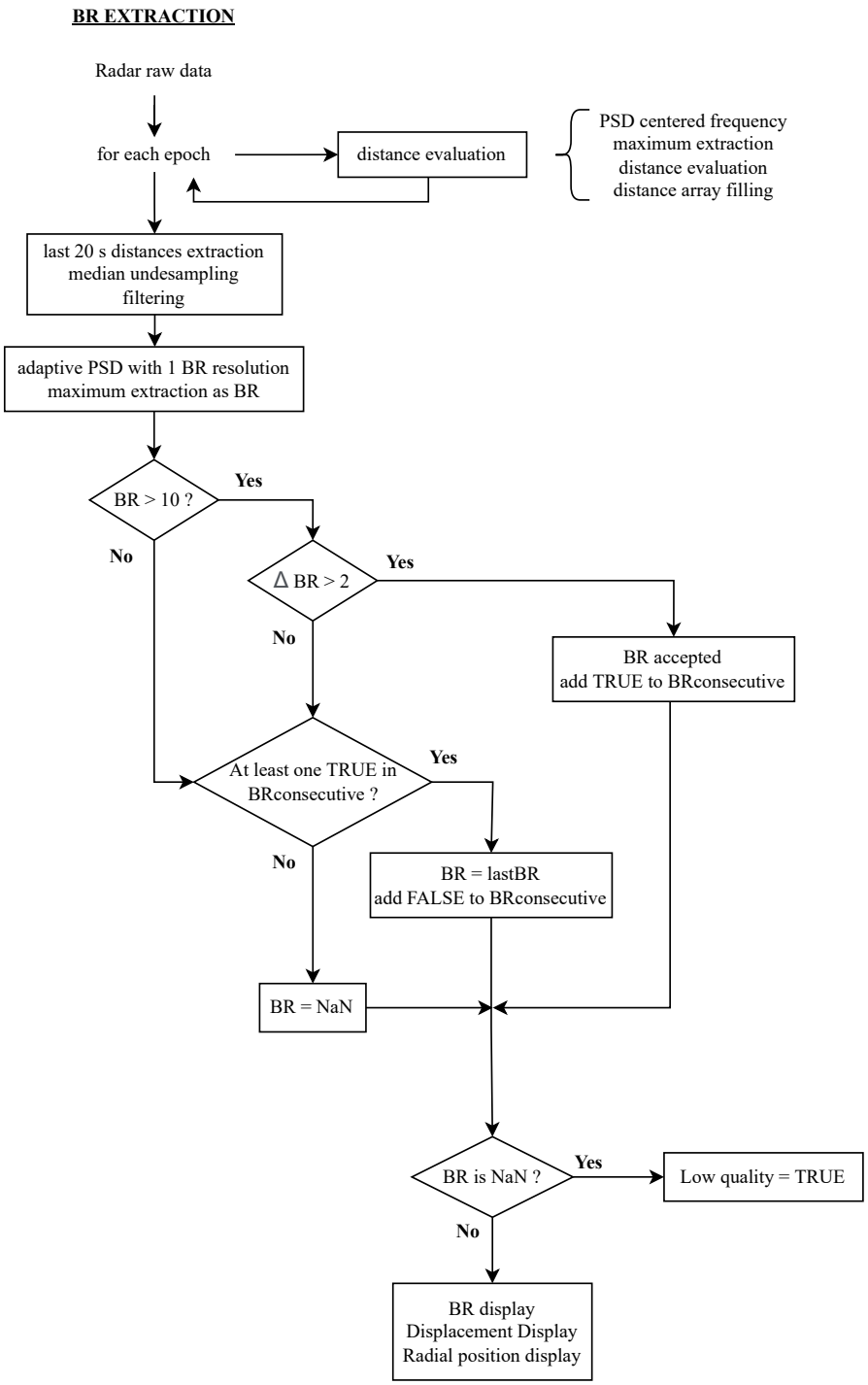

Figure 4.12: Vital signs extraction flowchart.

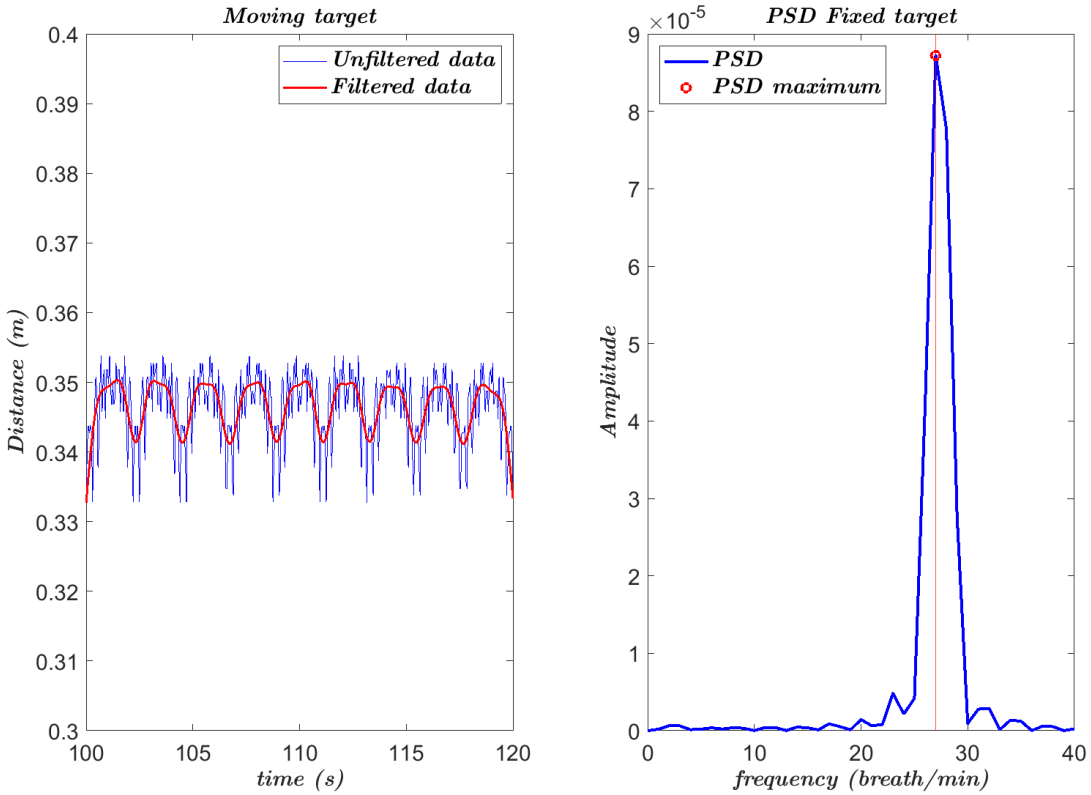

Figure 4.13: Breath rate extraction example.

Chapter 5

3D printer simulation

5.1 CAD for the radar's supports

The experimental setup to carry out all the tests presented required the production by a 3D printer of a specific substrate. The radar interfaced with the microcontroller was small and difficult to handle. In addition, stability was a prerequisite for the radar because, in case of oscillations, it would be impossible discriminate variations in target-subject distance due to the motion of the radar and variations due to the chest movement. The case was planned by Form 3+ printer from FormLab, which works with a photosensitive resin. This printer was chosen from those available because of its high resolution, a necessary parameter given and the small size of the device. We used SOLIDWORKS software to make the CAD, with which the geometry was drawn. A photograph of the device is presented in ***figure 5.1*** to show that the only possible attachment points are the three holes in the board containing the microcontroller. They were chosen to design a support system consisting of three cylinders that would fit inside the holes. The connection, however, also required that the radar be firmly in place, so a fastening system was made that would ensure stability but not risk going into mechanical contact with electronic components on the board. ***Figure 5.2*** shows the realized case.

The second support allowed the cardboard boards to be attached to the tracks of the RepRap X400 V3 3D printer. The path under consideration, ***figure 5.3***, is the one on which the extruder moves in 2D space via linear actuators. Through the designed support, it was therefore intended to attach rigid cardboard to these metal rails so that it would not oscillate during movements but would move in solidarity with the rails. Therefore, a 14 centimeter long and 3 centimeter wide plaque with two 'C' hooks attached to secure the plaque to the rails was chosen as the main structure, ***figure 5.3***. The plaque size selected is related to the boards' size for stability. To be even more sure of the strength of the infrastructure, we

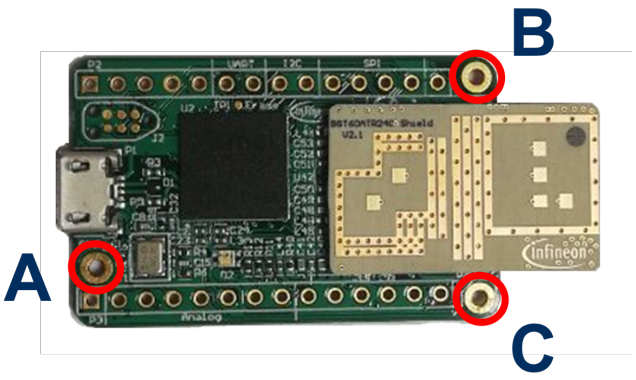

Figure 5.1: BGT60ATR24C photo with anchorage points (A,B,C).

Figure 5.2: 3D printed case.

used two supports placed at the ends of the boards.

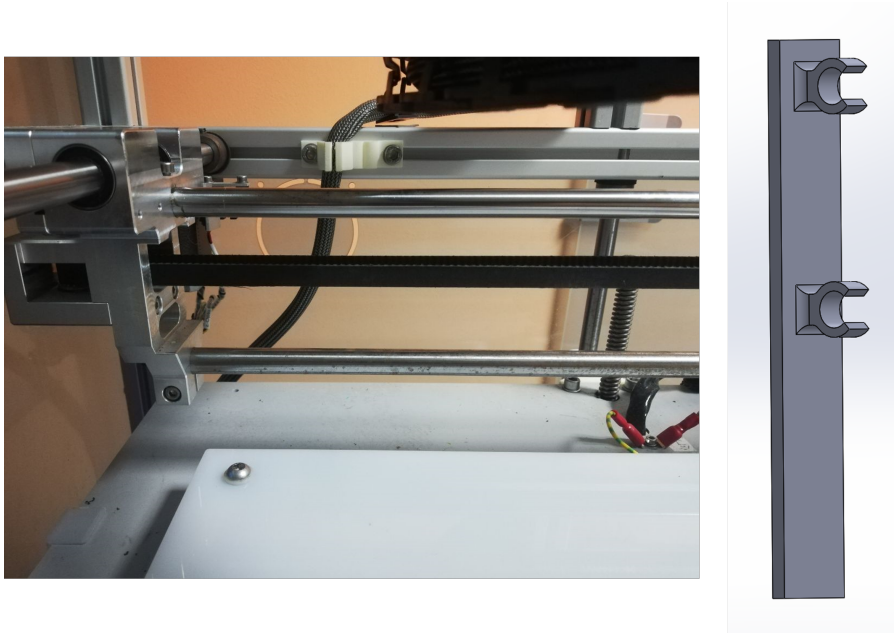

Figure 5.3: 3D printed hook and rails.

5.2 REPRAP X400

One of the algorithm validation steps was carried out using the RepRap X400 PRO V3 filament 3D printer from German RepRap. We chose it for some pecuniary features of particular interest. First and foremost, the large 390 x 400 x 320 millimeter print area allowed the use of cards, even large ones, to model the human torch. Furthermore, the feature of most significant interest for application as a validation model was the position accuracy along the XY plane, guaranteed by datasheet at 100 µm [48]. The high accuracy need is due to the type of signal to be modeled, which has an amplitude of a few millimeters. However, using a technology that is not specific to the designated application has some non-negligible limitations. The main ones are related to the extruder's minimum and maximum movement speeds. The maximum speed was going to limit the maximum frequency of the signal to be modeled in simulations with large movements. This limitation, however, did not have much impact on respiratory signals that, at most, have frequencies of about 40 to 50 breaths per minute. On the other hand, the presence of a minimum rate was strongly limiting. In the fact of signals with reduced amplitude and frequency, the motion obtainable with the printer was highly distorted from the ideal movement to be represented. This phenomenon reduced the number of tests that could be performed and the range of model parameter changes. In ***figure 5.4***, an example of distortion is shown. The signal taken as the respiratory model is a

sine wave having an amplitude of 12 millimeters and a frequency of 21 breaths per minute. As observed in the right section, the signal obtained, although it respects the general morphology of the ideal signal as the number of pulses and periodicity, has a shorter overall duration. Observing the zoom on the left, for the portions of the signal where the derivative is high, the obtained signal and the ideal signal have similar behavior. For the portions where the derivative tends to zero, the real motion has a different behavior with a rebound effect instead of a progressive slowing down resulting in a reversal of the direction of motion. Therefore, the presence of a minimum velocity leads to a change in the respiratory rate simulated with the 3D printer, which is recalculated for each signal, taking into account the minimum working velocity of the printer. The methods of transformation are clarified in the following section.

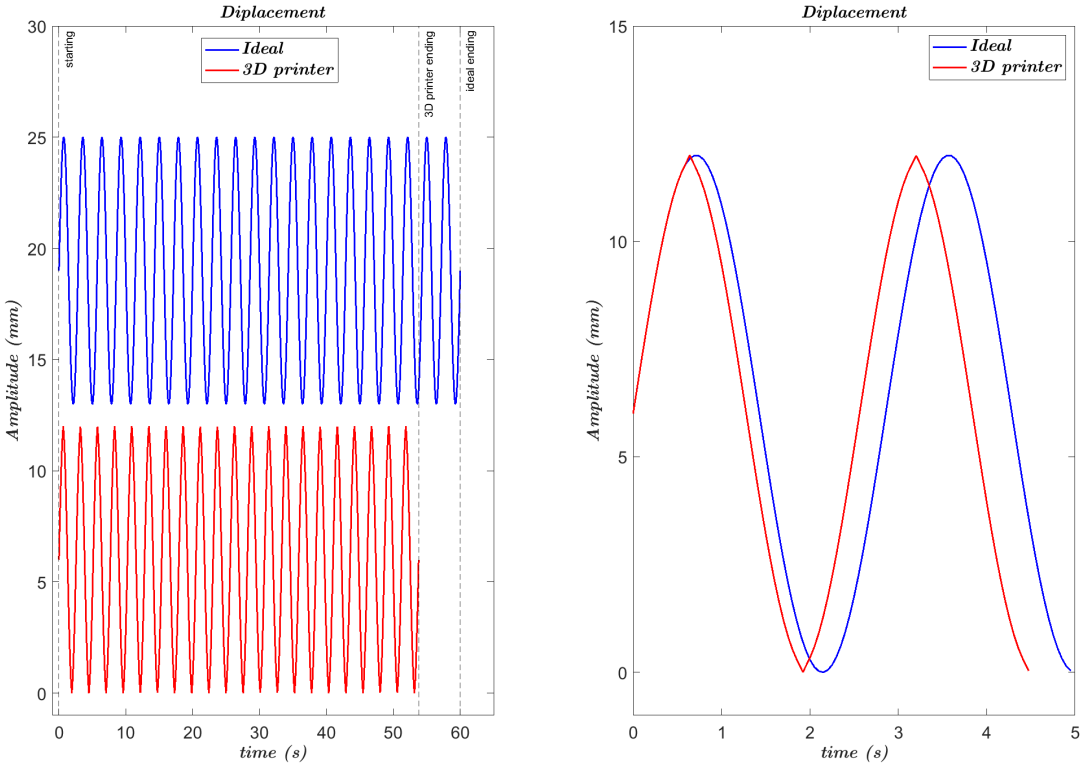

Figure 5.4: Comparison between the ideal signal and the real signal obtained by the 3D printer.

5.3 G-code

The operation of the 3D printer is based on the use of 'Simplify 3D' software, which converts CAD produced by software (such as Solidworks) into g-code instructions executable by the printer. In order to simulate the desired signals by 3D printer, g-code programming was used, overcoming the necessity of using 'Simplify 3D'. Before proceeding comes with the description of the method of conversion from model signal to g-code, a brief introduction to the g-code language and its commands used in the application is proposed. The commands are divided into different types depending on the reference letter. There are, in fact, G commands specific to positioning, F commands related to the speed of extruder movement, M commands specific to settings regarding motors, and the P command that imposes a pause. The main commands in each category are given in ***table 5.1***.

Table 5.1: Most used g-code commands.

Commands	***Description***
G0	fast moving
G1	controlled moving
G4	allow to set pause with P or S comands
G17	plane XY
G21	all measure in millimetre
G28	return to the home position
G90	absolute coordinates
G91	relative coordinates
M0	machine stop
M1	sleep modality
M05	spindle off
M30	main program end
M106	set fan speed
M108	extruder velocity
F	impose the velocity
S or P	impose the time to temporary stop

The commands shown in the table are just some of those used in 3D printer programming and are those that were used for motion simulations. The commands needed mainly concerned the definition of the reference system, extruder motion, and pause commands. The operation of the desired signal to gcode converter is shown in the block diagram in ***figure 5.5***. The first operation defines the time axis of the signal to be simulated by defining its overall duration and temporal resolution (dt). Then the signal is generated analytically as desired positions in

time expressed in millimeters. Obviously, the positions are understood as positions occupied by the extruder, thus taking into account the reference system of the printer. Once the desired signal is obtained, the extruder movement speeds (v), in mm/min, to reach consecutive positions in the desired time interval (dt) are calculated as follows: $v = \frac{\Delta s}{\Delta t}60$. A rounding of the s and v signals is then performed, and you are ready to write the signal-equivalent g-code into a text file. The first instructions to be written are to define the axes with commands G21, G17, and G90, to define all position measurements in millimeters, the motion in which plane it is being executed (XY), and that absolute coordinates are being used. Next, you write the instruction that brings the extruder to the initial position with a fast motion defined by instruction G0. For each subsequent position in the desired signal, an instruction is written with command G01 defining the new position and the speed with which the extruder will reach it, starting from the one currently occupied. This process is repeated iteratively for all positions. The only anomaly occurs when the associated speed is zero for a given position, which means that two consecutive positions are identical. In this case, instead of a displacement instruction, a pause instruction is written to the file with a duration equal to the time resolution chosen when constructing the time axis. When the signal conversion is finished, the extruder returns to the initial position with the G28 command, the spindle is turned off, and the main is terminated.

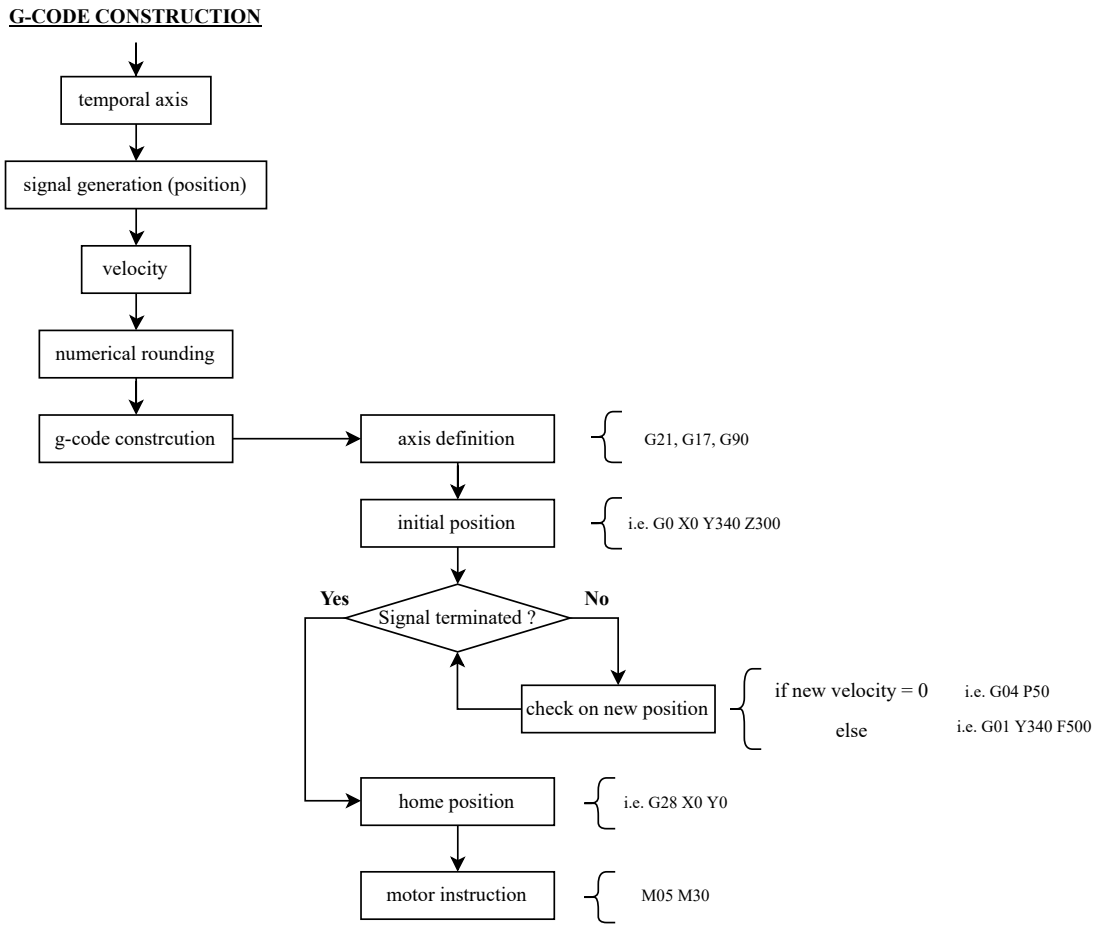

Figure 5.5: G-code construction scheme block.

Chapter 6

Results and Discussion

The following chapter describes how the different validation steps were performed. Regarding the tests performed with the signals synthesized with Matlab, validation was performed on the algorithm for extracting the physiological parameters following the extraction of the radar-subject distance. On the other hand, as for the tests performed with the 3D printer, validation was performed on the entire algorithm, including the target detection sections and parameter extraction. The entire algorithm was verified under real-world conditions in the third and final stage. Here, it was observed that the simulated conditions were far from the real ones and therefore, modifications were performed on the algorithm to make it more robust and sensitive for the application. Here, in particular, we modified the distance extraction process from the PSD of the different chirps.

6.1 Synthesized signals on Matlab

6.1.1 Measurements

The first validation phase was performed on the section of the algorithm that extracts the respiration rate from a chest motion signal. Since no real data were available at first, the breath was simulated as a sinusoidal motion with different frequencies. To simulate an actual input signal to the algorithm, different types of noise were added to the simple sinusoidal motion to verify its stability and robustness. We manufactured four different types of noise: uniformly distributed noise, normally distributed noise, linear component, and low-frequency sinusoidal modulation. All additive noise types were simulated with different intensities and related to different breathing frequencies. The different combinations used are shown in ***table 6.1***.

Table 6.1: Additive noise simulation parameters.

Uniformly distributed random noise	
Breath Rate (breath/min)	Noise amplitude (%)
[10 , 15 , 20 , 25]	[5 , 10 , 15 , 20]

Normally distributed random noise	
Breath Rate (breath/min)	Noise amplitude (%)
[10 , 15 , 20 , 25]	[5 , 10 , 15 , 20]

Linear increase noise	
Breath Rate (breath/min)	Total increase (%)
[10 , 15 , 20 , 25]	[5 , 10 , 15 , 20]

Linear decrease noise	
Breath Rate (breath/min)	Total decrease (%)
[10 , 15 , 20 , 25]	[5 , 10 , 15 , 20]

Sinusoidal modulation noise	
Breath Rate (breath/min)	Noise frequency factor
[10 , 15 , 20 , 25]	[0.4 , 0.6 , 1.4 , 1.6]

The first two types were designed to simulate noise on the extracted distance signal, either due to any noise in the raw data or introduced by the target search and localization section. The noise intensity was modulated in amplitude as a percentage of the amplitude of the breathing motion. On the other hand, the linear component was entered as a summative disturbance to the respiratory signal to simulate the patient's movement approaching and moving away from the radar. We did this to test how robust the algorithm is to any patient movement. The noise intensity for this type was modulated as a percentage change in distance throughout the signal relative to the resting position. The last type of noise, on the other hand, is a sinusoidal modulation summed with the respiratory signal to simulate the tilting motion of subjects during standing trials. In this case, however, the noise modulation was chosen related to the reference respiratory signal with a specific factor. The last two types of noise have relevant utility, especially in the actual simulation of tests performed on subjects. Indeed, it would be unrealistic to assume that although standing and stationary, the subjects do not exhibit any

movement, either tilting or approaching, or moving away from the radar. ***Figure 6.1*** shows in order the reference signal with a respiratory rate of 20 breaths per minute and the different types of additive noise, each with a specific modulation.

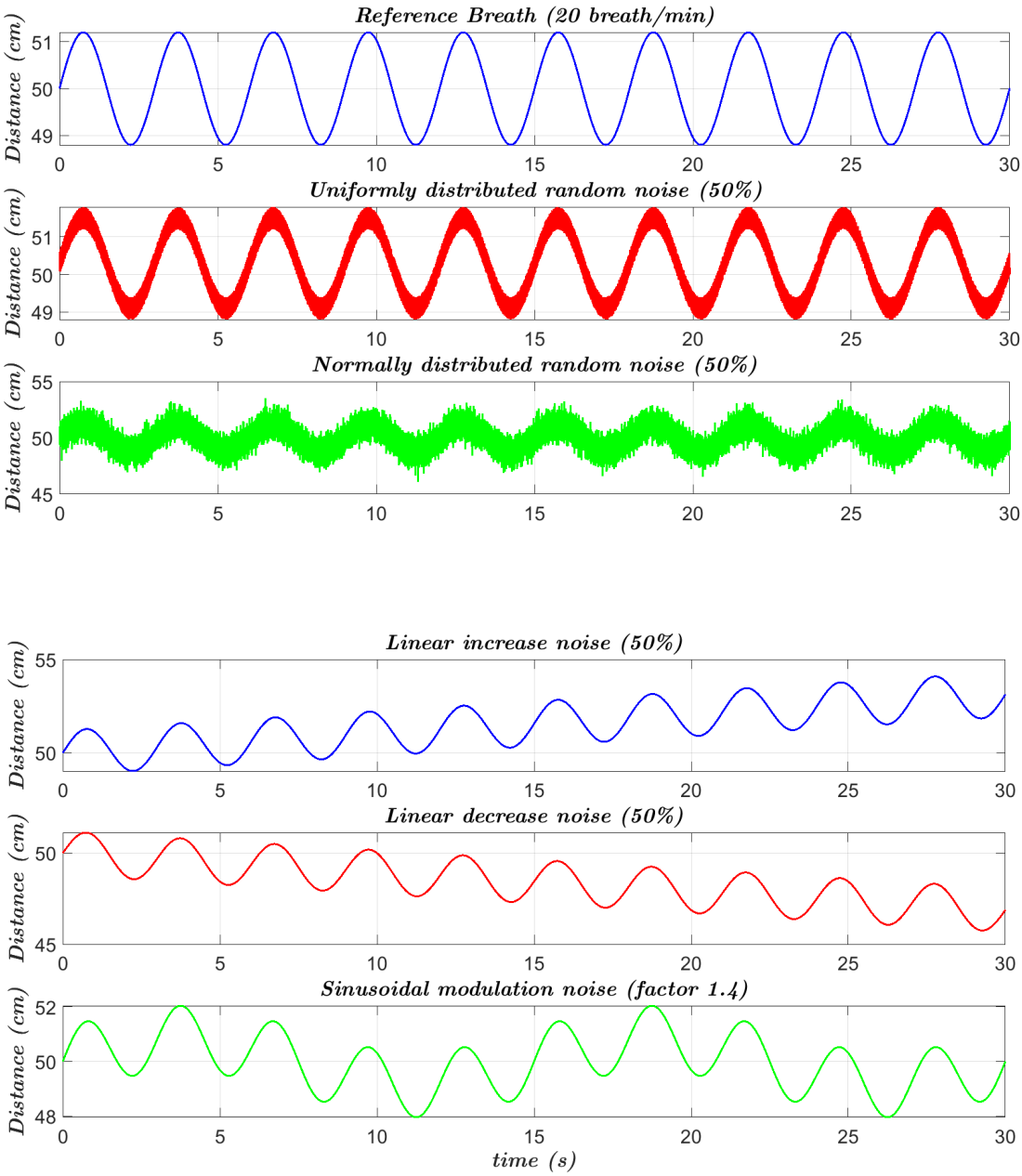

Figure 6.1: Comparison between different noises.

6.1.2 Results

We analyzed the results by comparing the output of the algorithm against the reference value over windows of 20-seconds duration shifted between them by 1 second to simulate the real behavior during the acquisitions. This was repeated for all synthesized signals, and two parameters of interest were evaluated for each: accuracy and the maximum error committed. The results have been reported in ***figure 6.2 - 6.3 - 6.4 - 6.5 - 6.6***. As can be observed graphically, the accuracy turns out to be 100% in almost all cases analyzed. Exceptions are three cases in which the accuracy remains above 80%. It is interesting to observe that the algorithm makes errors in the case of low-frequency signals (10 breaths per minute) given the short window duration. It was verified, however, that although the accuracy is not maximum for these cases, the error committed is less than one breath per minute, estimated by the algorithm to be at fault.

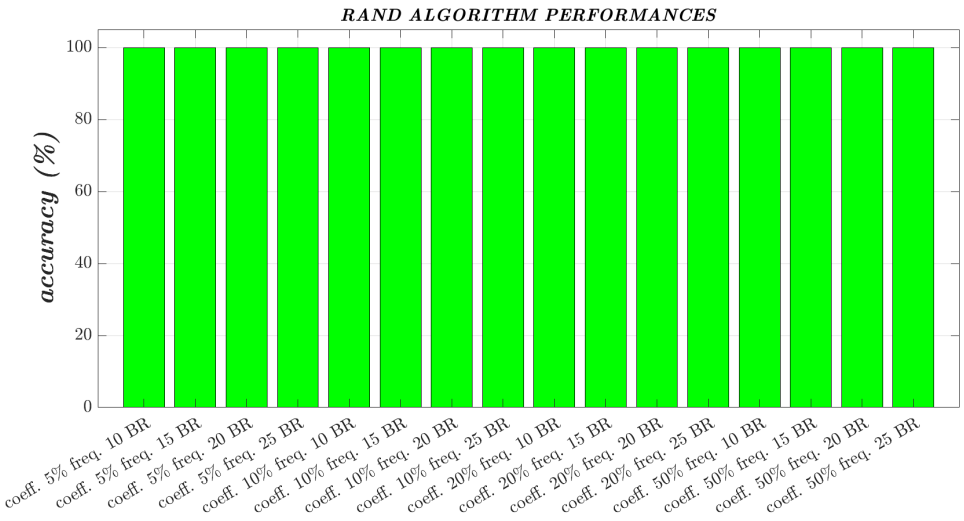

Figure 6.2: Accuracy on uniformly distributed random noise.

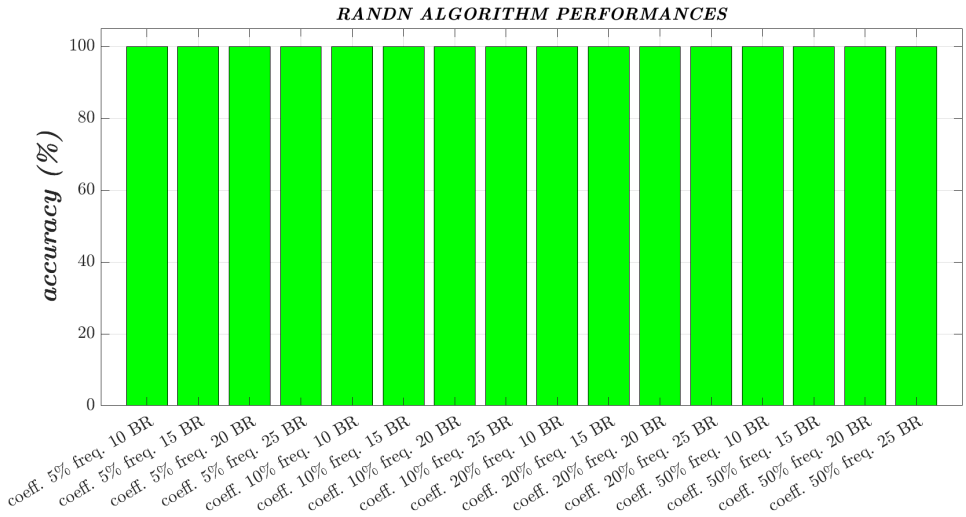

Figure 6.3: Accuracy on normally distributed random noise.

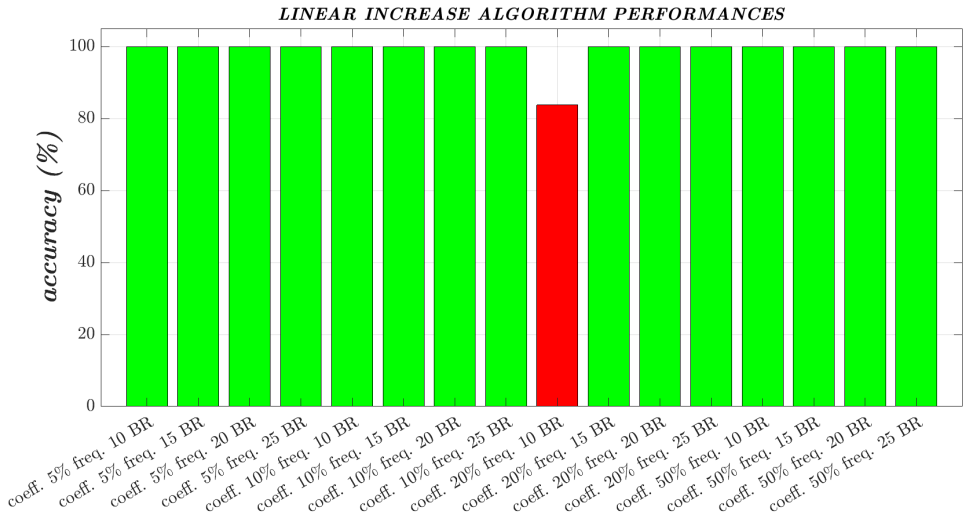

Figure 6.4: Accuracy on linear increase noise.

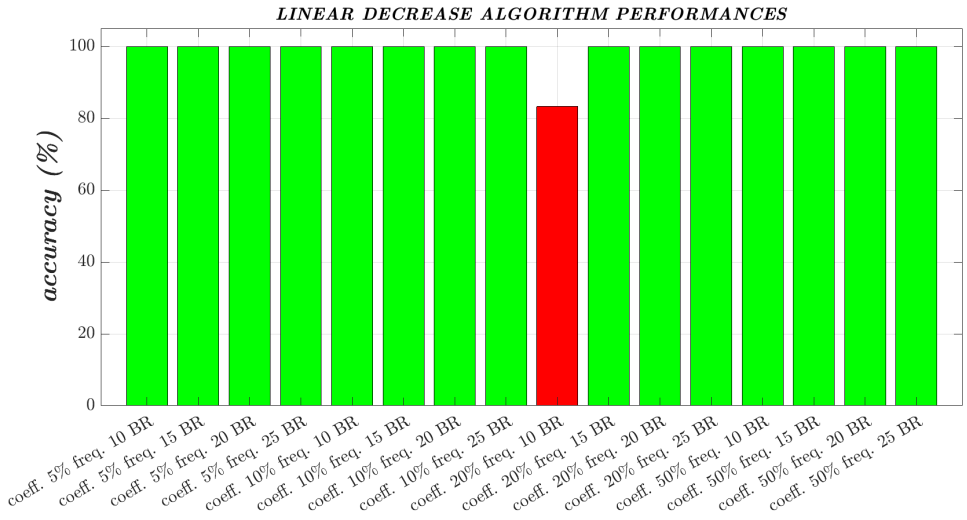

Figure 6.5: Accuracy on linear decrease noise.

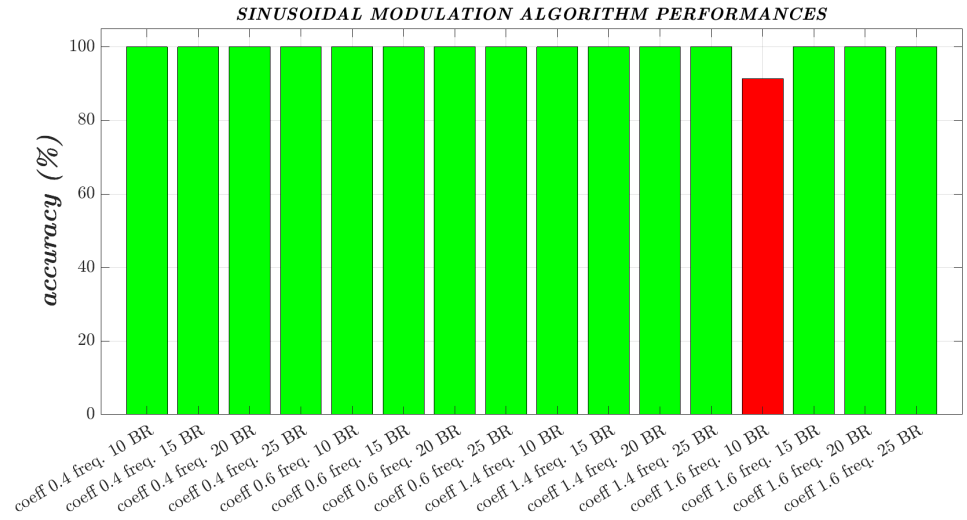

Figure 6.6: Accuracy on sinusoidal modulation noise.

6.2 Real data on Matlab

6.2.1 Measurements

To further test the robustness of the algorithm, real signals obtained from the study [2] were also used. The objective of this article was to compare data obtained from an electrocardiograph, a respiratory belt, a thermal nasal sensor, and a VICON system with markers placed on the chest (***figure 6.7***), for the study of chest motion

related to cardiac activity. Along with the article, the acquired data that were used

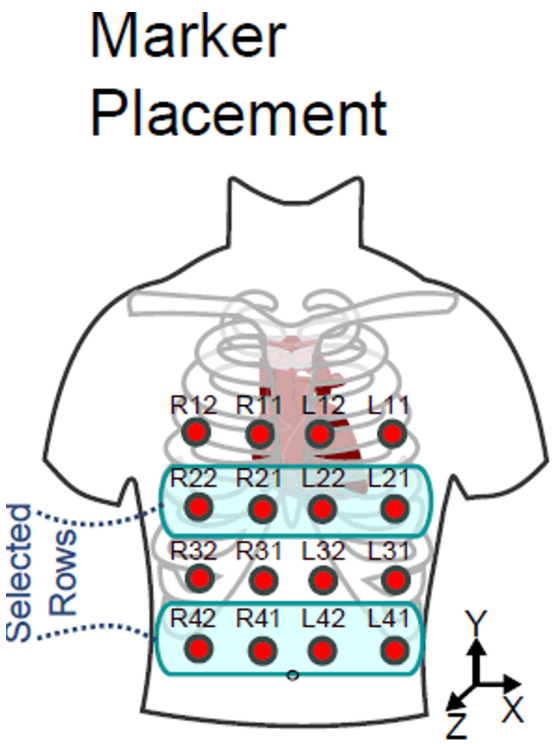

Figure 6.7: Thoracic marker position [2].

in this phase were also published. During the tests, different patients were asked to breathe while lying on a horizontal plane in different modes: free breathing, irregular breathing, apnea, and post-exercise breathing. The data taken, of interest for this testing phase, are those related to the respiratory belt and the motion of the L12 marker positioned anterior to the patient's chest, as shown in ***figure 6.8***.

The signal from the respiratory belt was used to define the correct respiratory rate. The marker motion, on the other hand, simulates the input signal to the physiological parameter extraction algorithm, and the algorithm is tested on this. We analyzed 21 signals acquired from subjects during a resting breath and three signals related to post-exercise breath. The signals related to apnea and irregular breathing were not considered as they were of little interest for the extraction of resting respiratory rate, the objective of this thesis. Analysis of the reference respiratory belt signal was performed in the time domain. The signal was filtered in the respiratory band between 5 and 40 breaths per minute using a Chebyshev Type I low-pass filter of five order and a Butterworth highpass filter of four order. Then the maximum and minimum were identified for each respiratory cycle. Using the same subdivision into windows used for the frequency analysis, the maxima

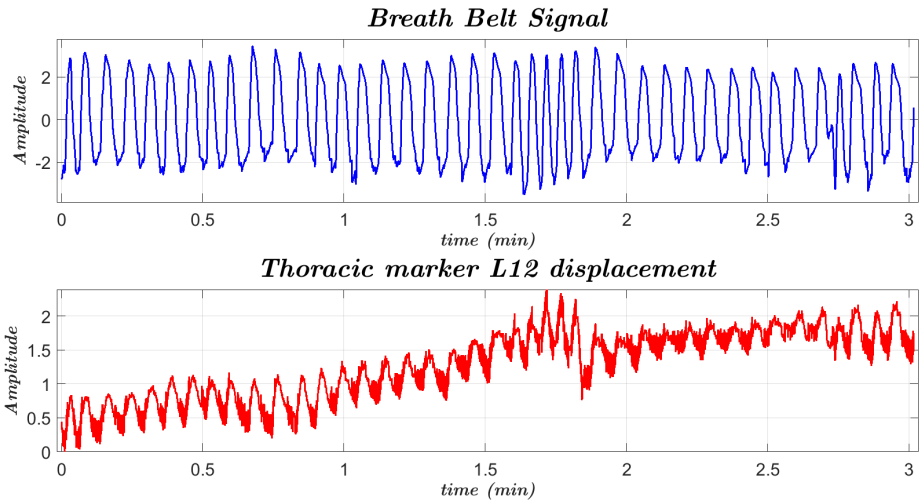

Figure 6.8: Example of respiratory belt and L12 marker displacement signals.

and minima of the respiratory cycles in them allowed the respiratory rate to be calculated. We performed a visual check for the correct identification of the points of interest for each signal. Frequency analysis, on the other hand, was performed on the thoracic marker displacement signals. An example of the analysis just described is given in ***figure 6.9***. The respiratory belt signal is reported with the maxima and minima correctly identified during the temporal analysis to define the 'correct' respiratory rate used as a reference and compare the respiratory rate extracted by the two methods.

6.2.2 Results

Both analyses, with the frequency method and peak over time analysis, were performed on windows of 10 seconds duration. For each window, the respiratory rate was calculated with both methods. The accuracy of the frequency method was then compared with that of the time method. ***Table 6.2*** shows the accuracies calculated as the average between the individual accuracies for each patient in the two breath types. Three accuracies were considered by considering, in addition to the coincident case, cases in which the frequency method differed by one or two breaths.

The overall accuracy appears to be high, especially considering the difference of one breath per minute is insignificant. Since an uncertified algorithm is taken as a

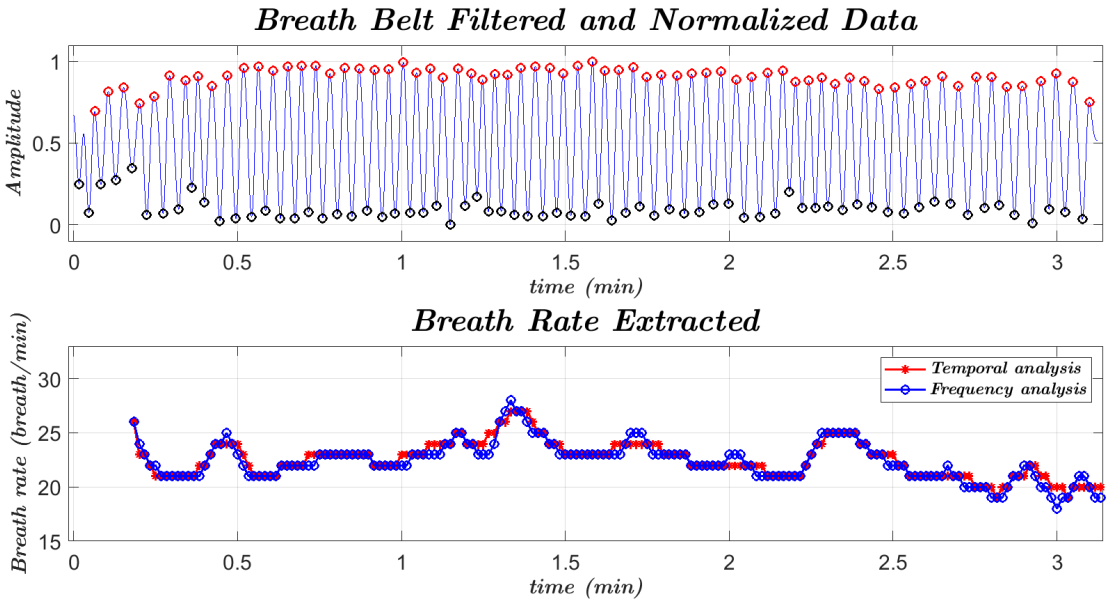

Figure 6.9: Breath rate comparison between temporal analysis on the breathing belt signal and frequency analysis on the marker displacement.

	ACCURACY			
	tollerance (breath/min)	**mean (%)**	**min (%)**	**max (%)**
free breathing	0	46.14	27.12	69.66
	1	84.63	65.12	99.42
	2	91.82	73.68	100
post exercise breathing	0	30.88	23.99	41.24
	1	69.53	62.73	76.84
	2	81.65	78.60	83.62

Table 6.2: Accuracy results on breathing and chest displacement signals taken from [2].

reference, the assumption that a difference of one breath per minute is negligible is more than reasonable. It can also be observed that accuracy is lower for signals extracted after exercise. This phenomenon can be attributed to two different aspects. The first is related to the more significant breathing irregularity during fatigue and breathlessness than during tidal breathing. The second is associated with the low numerosity of signals of this type, which reduces their statistical significance.

6.3 3D printer validation

6.3.1 Measurements

In this validation phase, we used the RepRap X400 filament 3D printer to simulate thoracic motion due to breathing. The validation steps with the printer were divided into two stages. The first round of analysis was to test the algorithm's ability to discern between a stationary or moving object and to begin testing the radar's ability to recognize large movements. In the second round of analysis, breathing acts were simulated using a sinusoidal pattern, with amplitudes and frequencies consistent with those found in the literature. The study of the reproduced movements and the results obtained are given below. In the first round of analysis, we synthesized several signals composed of static intervals alternating with sinusoidal motions around the rest position with different frequencies and amplitudes of motion. The signals were first generated on Matlab, later converted to gcode, and finally reproduced with the printer. For the generation of the signals, the temporal resolution of the instructions was set to 10 milliseconds to obtain as smooth movements as possible. The different signals consisted of four 'breathing' sessions with frequencies of 60 - 30 - 21- 12 breaths per minute, interspersed with periods of stillness lasting 20 seconds. The purpose was to test both the ability of the algorithm to distinguish between stationary objects and patients and to test the ability of the radar and algorithm to distinguish movements of small amplitudes. For this reason, signals with different amplitudes from 40 millimeters down to 10 millimeters were tested. Given the previously analyzed characteristics of the printer, the actual frequency of movement of the printer nozzle did not match the desired one. Therefore, the correct motion frequencies were recalculated to perform a comparative analysis of the results extracted by the algorithm. ***Figure 6.10*** shows an example of a signal generated through Matlab and the corresponding one produced by the 3D printer to compare with the radar data. It can be seen that the motion windows are of shorter duration than desired, and therefore the actual frequency is higher than desired. This limitation reduced the tests that could be performed with amplitudes less than 10 millimeters because motions at frequencies well above those of interest for the application under consideration would have been produced. All combinations of amplitude and frequency are shown in ***table 6.3***.

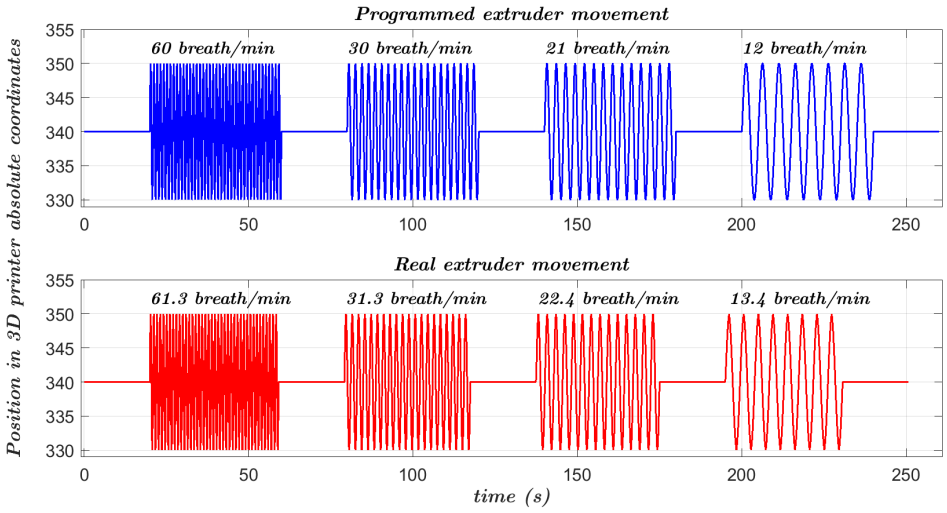

Figure 6.10: First validation cycle signal example designed on Matlab and real motion made by the 3D printer nozzle.

Amplitude (mm)	Programmed frequencies (breath/min)	Real frequencies (breath/min)
40	[60 - 30 - 21 - 12]	[60.2 - 30.7 - 21.7 - 12.7]
30	[60 - 30 - 21 - 12]	[60.7 - 30.9 - 21.9 - 12.9]
20	[60 - 30 - 21 - 12]	[61.3 - 31.4 - 22.4 - 13.4]
10	[60 - 30 - 21 - 12]	[62.7 - 32.8 - 23.9 - 15.3]

Table 6.3: Amplitude and frequency signal parameters compared to real 3D printer parameters movement, for the first validation cycle.

In the second round of validation using the 3D printer, we produced signals generated through Matlab to simulate real breathing acts. The amplitudes and frequencies of the signals were chosen based on the printer's literature and reproduction capabilities. A sinusoidal pattern was always chosen to simulate the respiratory act, given the simplicity of implementation. Individual signals generated with Matlab were converted to gcode. Each signal consists of 1 minute of stationary, followed by 3 minutes of simulated respiratory motion, and then returning to resting position, ***figure 6.12***. The signal sampling rate was set at 20 Hz, so that each instruction had a duration of 50 ms. Given, however, the movement limits of the printer, the real simulated respiratory phase has a shorter duration than desired, and therefore the real simulated frequency is higher. The signal thus constructed

allows testing of both the effectiveness of the discernment system between the stationary and moving object and verification of the correct extraction of the respiratory frequency. In fact, the first static phase simulates a stationary object, while the second phase simulates thoracic motion. The first phase then verifies the algorithm's ability to discriminate between a stationary object and a human while minimizing misclassification errors and extracting incorrect vital parameters where unnecessary. In addition, it allows the system to send to sleep mode if no subject is present to be monitored, reducing power consumption and enabling high energy savings. Five recordings were acquired during the test phase for each signal. An example of a generated signal is shown in ***figure 6.12***. In ***table 6.4***, on the other hand, the different combinations of frequencies and amplitudes used as well as the actual frequencies obtained with the printer, are shown.

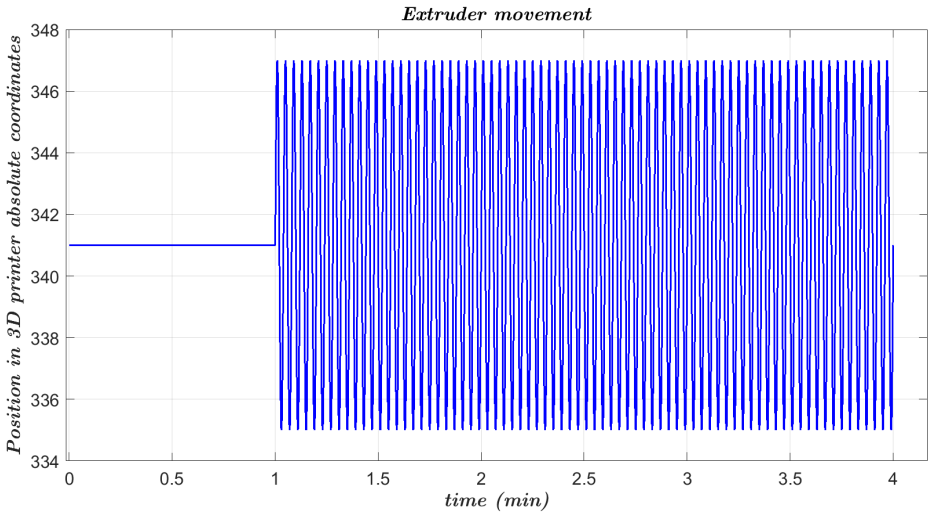

Figure 6.11: Second validation cycle signal example designed on Matlab and real motion made by the 3D printer nozzle.

Amplitude (mm)	Programmed frequency (breath/min)	Real frequency (breath/min)
12	12	14.8
	20	22.4
	25	27.4
7	12	18.3
	20	24.7
	25	29.4
4	20	31.9

Table 6.4: Amplitude and frequency signal parameters compared to real 3D printer parameters movement, for the second validation cycle

6.3.2 Results

We processed the data taken during the first validation run with the 3D printer to compare the real motion frequencies of the extruder with the respiratory frequencies extracted from the developed system. Recalling that the generated signal is composed of four different motion phases at decreasing frequencies (60 - 30 - 21 - 12 breaths/minute), the real extruder motion frequencies were calculated, taking into consideration the previously exposed printer speed limits. These values were later compared with the estimated values to verify the system's accuracy. In addition, it was verified whether the algorithm was able to recognize and distinguish motion phases from static phases by simulating the presence or absence of the subject. It was also verified that in the presence of motion, with a frequency higher than respiratory rates, the system would not consider the target to be of interest and, therefore, would not extract vital parameters. For different amplitudes of motion, the results obtained are presented in ***table 6.5***.

As can be seen, for all movement amplitudes, the system has high accuracy committing an error of at most two breaths per minute in the case of 10 millimeters amplitude. As the amplitude decreases, the error increases, and this phenomenon was expected since the movements are more challenging to identify. In all cases, however, the system correctly recognizes static from motion phases verifying that the algorithm correctly discriminates the presence of a subject from that of a stationary object. ***Figure 6.12*** shows, as an example, the signal related to motion with an amplitude 40 millimeters. During the first phase of motion with a rate of 60 breaths/minute, the algorithm does not extract the vital parameters because they are recognized outside the respiratory band. For the other phases, however, it correctly extracts the respiratory rate values with high accuracy and stability. The phenomenon of frequency estimation, even outside the motion ranges only, is

Amplitude (mm)	Description	Frequency 1 cycle (breath/min)	Frequency 2 cycle (breath/min)	Frequency 3 cycle (breath/min)
	Ref	30	21	12
40	Real	30 (30.0)	22 (21.7)	13 (12.7)
	Measured	31 (30.8)	22 (21.8)	13 (12.8)
30	Real	30 (30.4)	22 (21.9)	13 (12.9)
	Measured	31 (31.0)	22 (22.0)	13 (12.8)
20	Real	32 (31.5)	22 (22.4)	13 (13.5)
	Measured	31 (31.0)	22 (22.0)	13 (13.2)
10	Real	33 (32.8)	24 (24.0)	15.5 (15)
	Measured	31 (30.6)	24 (24.0)	14 (14.0)

Table 6.5: Results of the first 3D printer validation cycle.

related to the slippage of the observation window. Parameter estimation is based on the distance data of the last 20 seconds and therefore starts only when a large part of the motion signal falls within the observation window. With these promising analyses, we carried out the second round of validation.

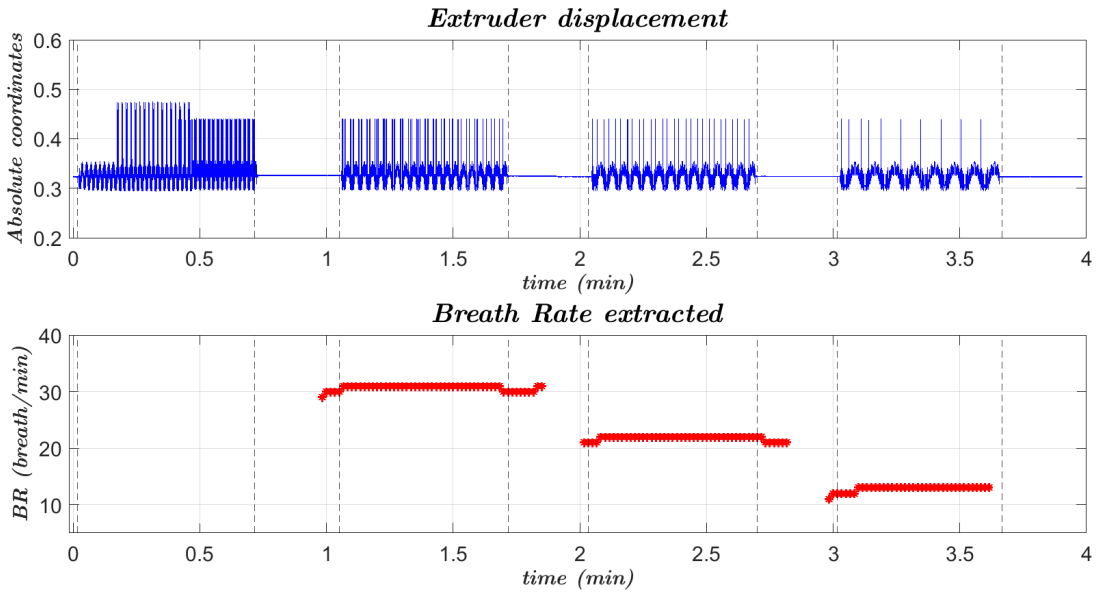

Figure 6.12: Example of breath rate extraction from extruder displacement.

The data obtained from the second validation run with the 3D printer were

analyzed with the following parameters:

- Detection of the cardboard as an object and correct classification as a fixed object within the first phase of signal stillness. This parameter is of interest for a twofold analysis. First, verify that the algorithm can correctly detect the object. Second, verify that the algorithm check how well the algorithm can detect an object, discriminate whether the object is stationary or moving;
- Number of windows in the motion range in which the algorithm did not extract any value of respiration rate due to poor signal quality. A high value of this parameter indicates that the signal quality is not sufficient to extract reliable vital parameters;
- Respiratory rate accuracy. This is the main parameter for evaluating the performance of the algorithm;
- Respiratory rate accuracy considering an error of one breath per minute as valid. Due to the limitations of the printer, the value of the reference frequency is not always integer. This parameter was therefore, included in the analysis to account for possible approximations of the respiratory rate.

The results shown in ***table 6.6***, show an overall high accuracy of the algorithm. For signals of 12 millimeters amplitude, the average accuracy over the different frequencies appears to be greater than 85%. Analyzing the value as the frequency varies, it is observed that the accuracy of the signal with reference frequency 22 breaths/minute is lower than for the other two cases. This can be attributed to the fact that the real frequency of the signal is 22,4 breaths/minute, which, however, since it does not make physiological sense, was rounded to 22 breaths/minute. However, since the frequency value straddles between 22 and 23, the algorithm sometimes misclassified the respiratory rate by committing an error of one breath per minute for this reason. Looking, in fact, at the accuracy, even with an error of one breath per minute, it rises above 96%. For signals with 7 millimeters amplitude, the average accuracy over all frequencies is lower than for signals with 12 millimeters amplitude. This is related to the reduction in motion amplitude and the more incredible difficulty detecting micro-movements. The accuracy with one breath per minute error is very high, however, because even for these signals, the real frequency of cardboard motion straddles two unit breath frequencies. There are, in addition, two signals with poor quality such that for 11% and 36% of the windows, respectively, the algorithm does not extract vital parameters. This 'safety' measure was included to avoid extracting erroneous vital parameters that, in the clinical setting, could deviate the physician's opinion with untrue values. In the case, on the other hand, of the 4 millimeters amplitude signals, performance is obtained with an average accuracy of'88% and with accuracy considering an error of one breath

per minute of more than 90'%. For all signals, moreover, the algorithm was able to detect the object and correctly classify the phases when it is stationary versus when it is in motion, confirming that the patient detection works with excellent performance.

Amplitude (mm)	**Reference frequency (breath/min)**	**Object Relevation**	**Low** quality (%)	**Accuracy** (%)	**Accuracy 1 BR** (%)
12	15 (14.8)	yes	/	93.1	100
		yes	/	95.8	100
		yes	/	82.1	96.6
		yes	/	92.5	96.3
	22 (22.4)	yes	/	71.9	98.8
		yes	/	81.3	99.4
		yes	/	79.6	96.7
		yes	/	80.6	100
	27 (27.4)	yes	/	96.3	100
		yes	0.6	90.7	93.8
		yes	/	96.0	100
		yes	/	69.4	96.7
7	18 (18.3)	yes	2.8	63.2	71.7
		yes	/	83.3	92.6
		yes	/	76.2	89.0
		yes	/	94.3	100
	25 (24.7)	yes	/	95.9	100
		yes	1.5	91.0	100
		yes	11.1	82.4	97.2
		yes	/	99.2	100
	29 (29.4)	yes	1.4	36.0	92.8
		yes	36	17.3	83.3
		yes	/	42.4	96.5
		yes	/	49.3	100
4	32 (31.9)	yes	/	97.2	100
		yes	/	99.1	100
		yes	1.8	76.8	80.4
		yes	1.9	78.5	88.8

Table 6.6: Results on second validation printer datas.

In ***figure 6.13***, an example of the distance signal evaluated by the algorithm compared with the real motion signal of the 3D printer is shown. It can be seen

that the amplitude of the motion that can be extracted from the radar is much higher than the real one, and moreover. However, the breathing signal is present and identifiable. It is submerged by a high degree of noise attributable to the different estimations of the instantaneous distance in the different chirps.

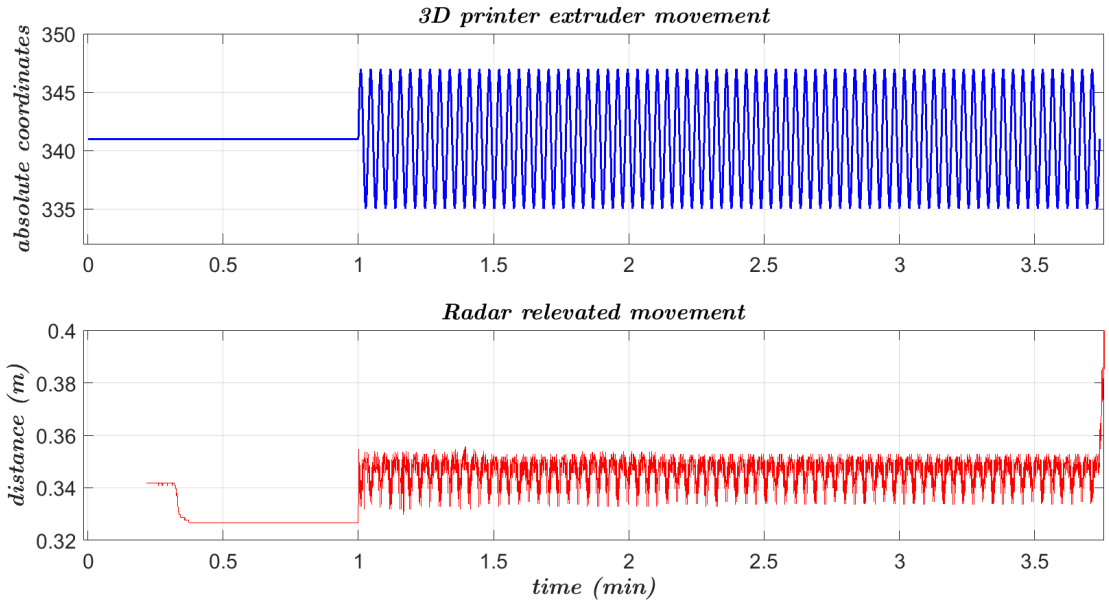

Figure 6.13: Comparison between 3D printer extruder real movement and radar extracted distance.

Thus, it is possible to conclude how the algorithm can correctly discriminate the presence of a subject or stationary object. Having identified the subject, the algorithm, under different conditions of breathing amplitude and with different respiratory rates, returns the corresponding value of respiratory rate with high accuracy, especially considering an error of one breath per minute is of little clinical significance.

6.4 Volunteers validation

6.4.1 Gold standard

The last validation phase was performed on volunteer subjects to verify the algorithm's behavior on real data and to compare the estimated respiration rate values with those extracted from a validated and commercially available device. The device used as a reference is the biosignalplux, a biosignal acquisition tool-kit

for advanced research applications (***figure 6.14a***). It consists of a central station, to which up to eight different sensors can be connected by cable, communicating with the computer via Bluetooth. The software used for communication is called opensignals (***figure 6.14b***) and allows various parameters to be set for the sensors, including, for example, the sampling rate and the number of bits of the ADC.

(a) *Biosignalsplux hub device [49].*

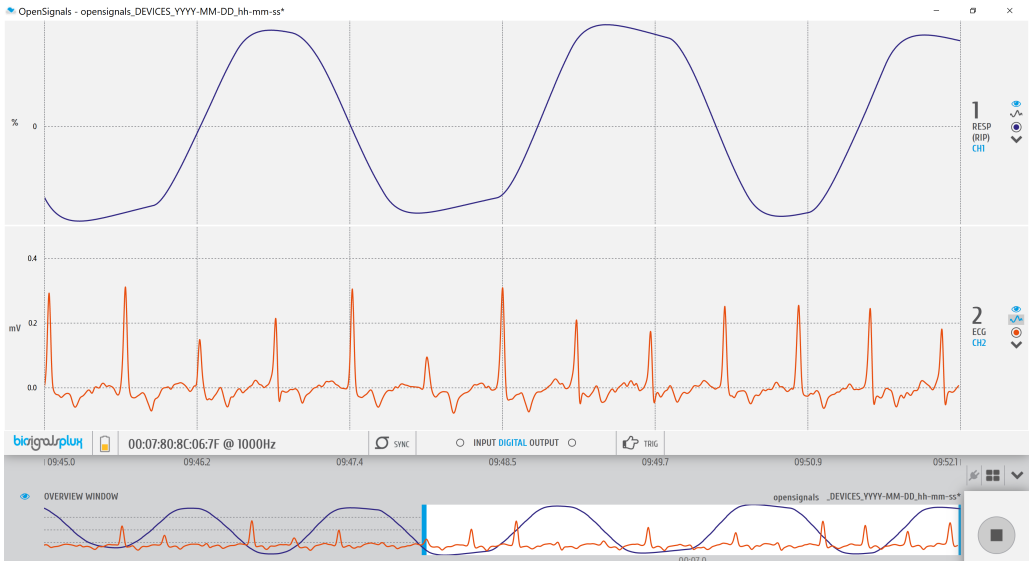

(b) *Opensignals interface.*

Figure 6.14: Biosignalsplux hub and Opensignals interface.

Several versions of the biosignalplux system are available, in particular, we have the professional version. Within that version were included the two sensors of

interest for this study, namely the respiratory band and the electrocardiographic sensor. The respiratory band used,[50] (***figure 6.15***), consists of an elastic band to be affixed around the chest and the PZT-sensitive piezoelectric element. Although the sensor only measures chest strain locally, the respiratory band allows the entire chest strain to be assessed, making the measurement less sensitive to motion artifacts. The elastic band is also adjustable in length to fit the subject. The sensor output is not directly the strain. Using the transfer function provided by the manufacturer, the output value allows the strain defined as a percentage between ±50% to be derived.

Figure 6.15: Biosignalsplux RIP sensor.

The second sensor used is the electrocardiographic sensor ,[51]. It consists of three electrodes (***figure 6.16***), of which the central one is a reference electrode, with which a differential bipolar measurement is made. It is a miniaturized system, equipped with a high SNR with an analog signal pre-conditioning circuit. Also for this sensor, the manufacturer provides the transfer function to convert the digital output to a voltage value between -1.47 mV and 1.47 mV.

6.4.2 Measurements

During this validation phase, we performed two acquisition types, one abdominal and one thoracic. The objective was to compare which of the two positions allowed a better respiratory rate estimation. It has been observed in the literature that

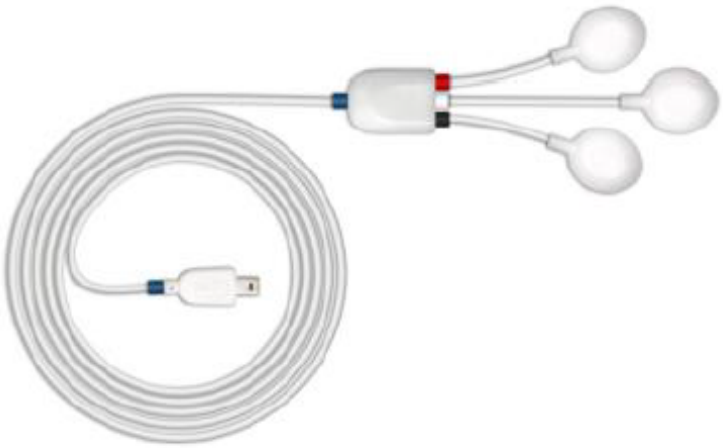

Figure 6.16: Biosignalsplux ECG sensor.

the abdominal position is the preferred one in several applications because it has a greater relative amplitude motion since, in the chest, the presence of the ribs increases stiffness. Tests were repeated for each type of acquisition, for a total of six acquisitions per subject. The following steps were followed for each test. The volunteer subject was asked to give verbal consent to use personal data for analytical purposes such as age, weight, and sex. The following data are of interest as they allow the identification of a more or less extensive chest. The subject was then placed in electrodes to extract the electrocardiographic signal used to analyze the possibility of also identifying this vital signal of considerable interest in the clinical field. The electrodes used were FIAM's F2080 in Ag/AgCl with a diameter of 55 mm. They were placed on the chest's left side at the level of the last ribs. Next, the respiratory band was placed on the chest at the sternum level. The placements are shown in ***figure 6.17***.

The radar, in its case produced by 3D printer, was mounted on a camera tripod and the height was chosen so that the projected wave was at the height of the umbilicus for abdominal motion measurements and at the height of the sternum for chest motion measurements, ***figure 6.18***.

Next, the biosignalplux was turned on, and we checked the quality of physiological signals obtained by electrocardiographic sensors and by respiratory belt. Having ascertained the quality of the signals, the real-time app for radar data acquisition and processing was launched. The two interfaces, that of opensignal and that of Matlab were placed on two parallel screens to monitor the progress. The single acquisition described below is then performed. The data of interest for both

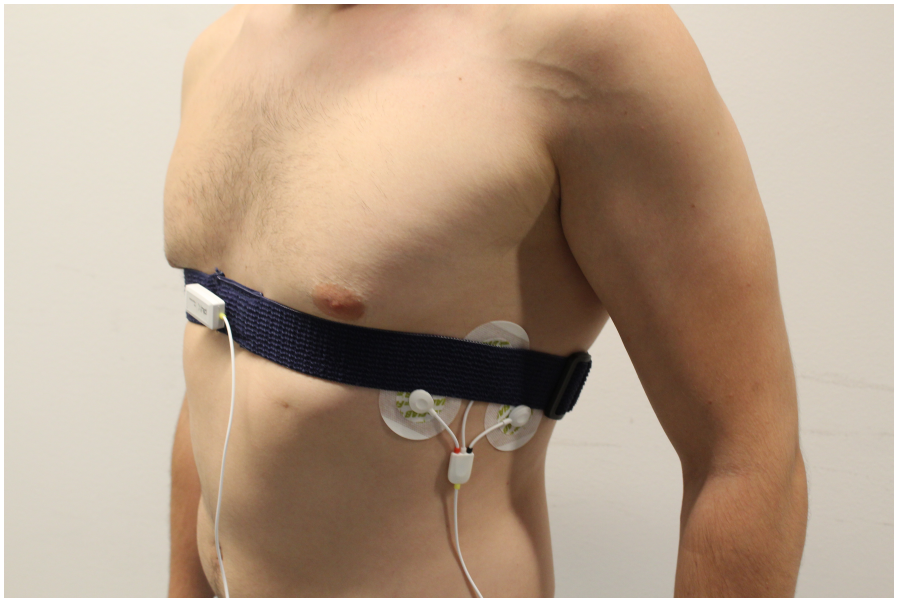

Figure 6.17: Representation of electrode and respiratory band placement on the patient's chest.

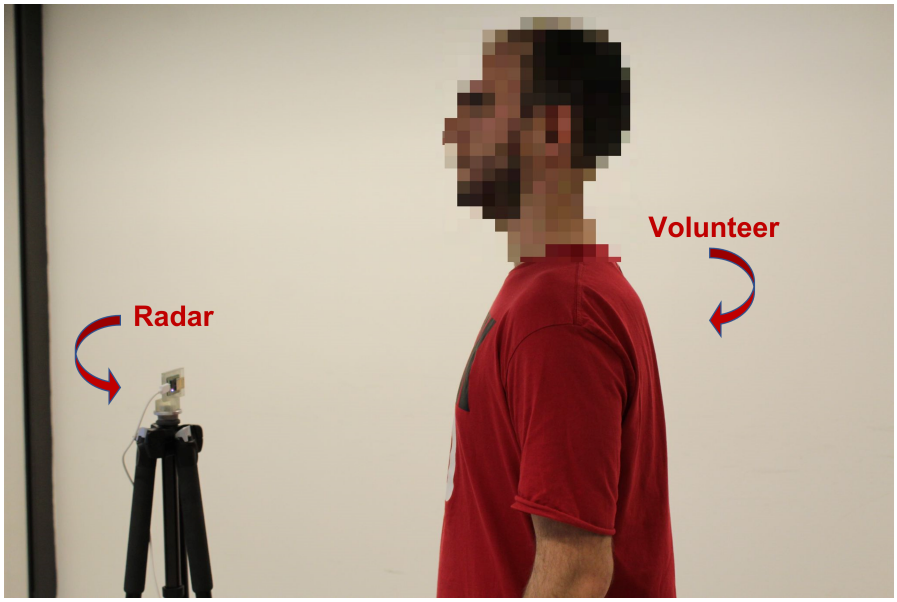

Figure 6.18: Radar setup.

interfaces were saved at the end of the acquisition. Opensignal allows the signals to be saved in a file with '.h5' extension, while through the GUI, the data were saved in '.mat' format. When the single acquisition was finished, the subject was

allowed to relax for a few minutes before resuming the next session. For the next acquisition, all steps were repeated, starting with the subject's positioning. A photograph of the experimental setup used is shown in ***figure 6.19***.

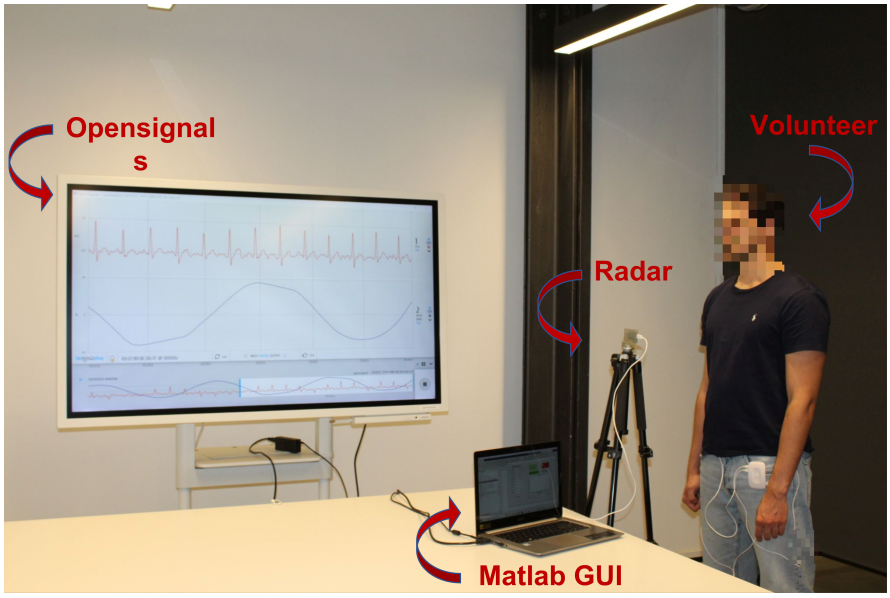

Figure 6.19: Complete setup.

The protocol used during the acquisitions is as follows: the subject is asked to perform 3 minutes and 30 seconds of relaxed breathing, followed by 40 seconds in which the subject is asked to accelerate the respiratory rate without hyperventilating, and finally, another 50 seconds of resting breathing is requested. The choice to vary the respiratory rate is due to the desire to test how readily the algorithm responds to a change in respiratory rate. The saved data were then reanalyzed later, and the results are shown in the following section.

6.4.3 Results

The tests were performed on three subjects aged 20 to 30, all in good health and with no diagnosed respiratory diseases. The biosignalplux data were compared and synchronized with the radar ones by comparing the respiratory frequencies extracted from both over the same observation windows. The respiratory belt data underwent several steps of analysis. They were subsampled at a frequency of 100 Hz with a median filter. They were then filtered by removing components outside the respiratory band. A Butterworth high-pass filter of order 2 and a cutoff frequency of 100 mHz and a Chebychev low-pass filter of order 3 with a cutoff frequency of 0.5 Hz was used. Respiratory frequency was extracted by frequency analysis on windows of

the same duration as the developed algorithm. The respiratory frequency data were then synchronized with those extracted by the algorithm to perform a comparison. Of the three subjects evaluated, only one yielded comparable results. For the other two subjects, the distance signals extracted with the radar did not allow any vital parameters to be evaluated. For the first subject, however, as shown in ***figure 6.20***, the distance signal is comparable with the chest strain signal measured by the respiratory band. ***Figure 6.20***, also shows how the algorithm takes about one minute to recognize the subject and then begins to estimate the vital parameters. The accuracy obtained on this subject's results is shown in ***table 6.7***.

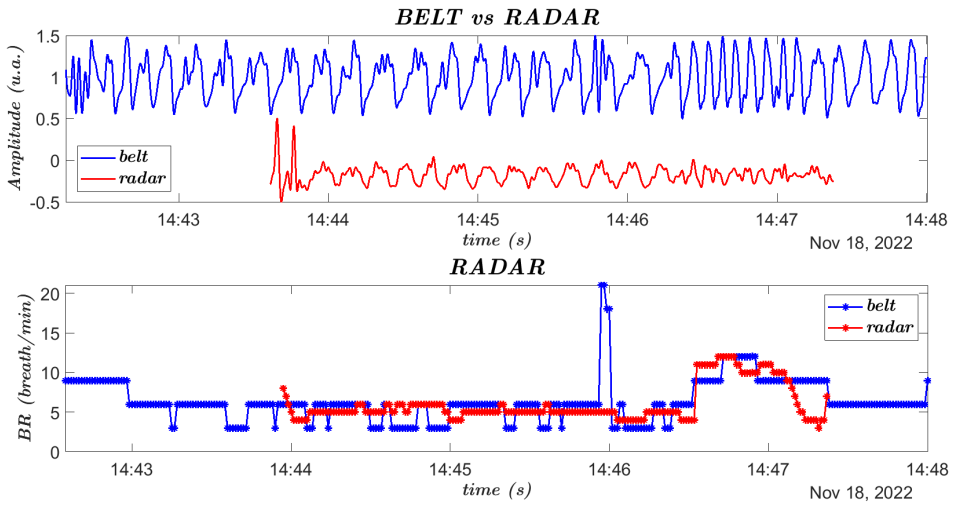

Figure 6.20: Comparison of thoracic displacement and breath rate signals.

	Accuracy (%)
Thoracic	63.07
Abdominal	56.0

Table 6.7: Volunteers breath rate test accuracy.

It can be seen that no significant difference was found in the results obtained at the abdominal level or at the thoracic level, which in both cases show an accuracy of around 60 percent. However, the numerosity of tests and analyses needs to be increased to arrive at more in-depth conclusions by comparing the two placements. Instead, an example of data extracted from the second and third patients is shown in ***figure 6.21***. As can be seen, especially when compared with ***figure 6.20***, in ***figure 6.21***, it is impossible to detect any pattern of comparison with data from the respiratory belt. There may be several reasons for this behavior. As

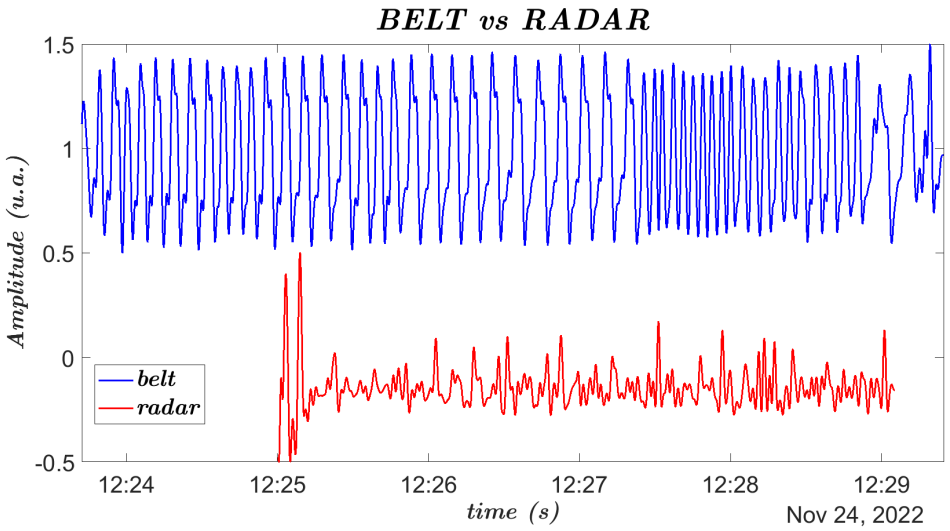

Figure 6.21: Comparison of bad thoracic displacement signals.

a first aspect, the difference between the cardboard used for the model and the human thorax intervenes. The thorax has a less smooth and uniform surface than the cardboard producing more reflections at different angles. In addition, respiration simulated with the 3D printer presented a constant frequency with larger amplitudes of movement, while human respiration is less regular, with varying frequencies and amplitudes between consecutive breaths. Intervening, in addition, are motion artifacts from movement by the subject due to in situ oscillations during the test. To rule out these components in the future, tests could be conducted in positions of more excellent stability, such as sitting, lying down, or leaning against a solid part. Although in the acquisition phase, ECG signal was also taken to check for potential heart rate extraction, quesat was not evaluated given the poor performance obtained with respiration alone. However, it is not ruled out that future work may increase performance and verify a feasibility of extracting this vital parameter as well with the use of radar. The conclusive results from this validation phase show that the whole system could be optimized to improve performance. However, the feasibility of using the BGT60ATR24C radar to extract vital parameters for subject 1 has been demonstrated.

Chapter 7

Conclusion

The purpose of the thesis project was twofold. The first was to characterize Infineon's BGT60ATR24C radar by investigating the application potential of the hardware, studying and understanding its settable parameters, and optimizing them for application. The second was to develop a real-time system capable of extracting a subject's vital parameters remotely and without contact by detecting chest wall movements. During characterization, it became apparent that there was high interference between 'emitting and receiving antennas at short distances. For this reason, the optimal distance chosen for the subsequent ones was between 30 and 40 centimeters. Starting from the characterization analyses, an algorithm was constructed that would take the raw data from the radar, recognize the presence of a subject in the field of view, and extract its vital parameters. There were several processing steps to test the algorithm with different outcomes. Initial validations were performed on respiratory data simulated with Matlab software and real chest motion data in an accessible database. The analyses were performed by investigating the accuracy of the respiratory rate extraction system. The signals produced were characterized by different noises, amplitudes, and frequencies. The obtained accuracies (>95%) allowed us to proceed to the following validation steps. The second primary validation phase was performed using the RepRap X400 3D printer to simulate thoracic motion during breathing. We mounted a 24,5 x 34 centimeters cardboard on the printer rails. By programming the printer in gcode language, the extruder movement and, thus the cardboard, simulated the thoracic motion due to breathing. Also, for this validation step, the accuracies obtained were satisfactory (>88%), considering an error of 1 breath per minute as of little relevance to the application. The last validation phase was performed on three volunteer subjects. The biosignalsplux system equipped with a breathing belt was used as a reference for extracting the respiratory rate. The subjects were asked to stand upright, facing the radar, and breathe naturally for five minutes. For two of the three subjects, comparison with the reference data was not possible,

given the poor quality of the signals. For the first subject, however, the accuracy obtained in the two configurations, abdominal and thoracic, was 60 % lower than those previously estimated with the 3D printer. The reasons for this reduction were attributed to several factors. The first aspect is related to the surface difference between the cardboard and a thorax; the latter produces multiple and directionally different reflections. In addition, the real thoracic movements of a standing subject are less periodic than those simulated with the 3D printer because of motion artifacts. The irregularity in both frequency and amplitude of the real breath also affected the conclusive performance. However, I achieved the thesis goal by demonstrating the BGT60ATR24C usability for contactless respiratory rate monitoring, as revealed by the analysis on the first subject. Future developments could go toward optimizing the algorithm by improving extraction performance. Performance could be investigated under different conditions: standing, sitting or lying down. One could also change the relative position by positioning the radar anteriorly, posteriorly, or laterally. Also, by configuring the radar in MIMO mode, multiple transmitting and receiving antennas could be used to reduce possible artifacts.

Bibliography

[1] Zhongyuan Fang, Wensong Wang, Jipeng Wang, Bingqiang Liu, Kai Tang, Liheng Lou, Chun Huat Heng, Chao Wang, and Yuanjin Zheng. «Integrated Wideband Chip-Scale RF Transceivers for Radar Sensing and UWB Communications: A Survey». In: *IEEE Circuits and Systems Magazine* 22 (1 2022), pp. 40–76. ISSN: 15580830. DOI: 10.1109/MCAS.2022.3142689 (cit. on p. 1).

[2] Ghufran Shafiq and Kalyana C. Veluvolu. «Surface chest motion decomposition for cardiovascular monitoring». In: *Scientific Reports* 4 (May 2014). ISSN: 20452322. DOI: 10.1038/srep05093 (cit. on pp. 1, 5, 26, 73, 74, 76).

[3] Salim S. Virani et al. *Heart Disease and Stroke Statistics - 2021 Update: A Report From the American Heart Association*. Feb. 2021. DOI: 10.1161/CIR.0000000000000950 (cit. on p. 1).

[4] Ting Zhang, Julien Sarrazin, Guido Valerio, and Dan Istrate. «Estimation of human body vital signs based on 60 ghz doppler radar using a bound-constrained optimization algorithm». In: *Sensors (Switzerland)* 18 (7 July 2018). ISSN: 14248220. DOI: 10.3390/s18072254 (cit. on pp. 1, 4).

[5] Hua Zhang, Sheng Li, Xijing Jing, Pengfei Zhang, Yang Zhang, Teng Jiao, Guohua Lu, and Jianqi Wang. «The separation of the heartbeat and respiratory signal of a doppler radar based on the LMS adaptive harmonic cancellation algorithm». In: vol. 1. IEEE Computer Society, 2013, pp. 362–364. DOI: 10.1109/ISCID.2013.97 (cit. on p. 1).

[6] Vladimir L. Petrovic, Milica M. Jankovic, Anita V. Lupsic, Veljko R. Mihajlovic, and Jelena S. Popovic-Bozovic. «High-Accuracy Real-Time Monitoring of Heart Rate Variability Using 24 GHz Continuous-Wave Doppler Radar». In: *IEEE Access* 7 (2019), pp. 74721–74733. ISSN: 21693536. DOI: 10.1109/ACCESS.2019.2921240 (cit. on pp. 1, 9, 26, 29).

[7] Dingyang Wang, Sungwon Yoo, and Sung Ho Cho. «Experimental comparison of ir-uwb radar and fmcw radar for vital signs». In: *Sensors (Switzerland)* 20 (22 Nov. 2020), pp. 1–22. ISSN: 14248220. DOI: 10.3390/s20226695 (cit. on pp. 1, 3).

[8] Fan Yang, Shan He, Siddharth Sadanand, Aroon Yusuf, and Miodrag Bolic. «Contactless Measurement of Vital Signs Using Thermal and RGB Cameras: A Study of COVID 19-Related Health Monitoring». In: *Sensors* 22 (2 Jan. 2022). ISSN: 14248220. DOI: 10.3390/s22020627 (cit. on p. 3).

[9] Erika Pittella, Anna Bottiglieri, Stefano Pisa, and Marta Cavagnaro. «Cardiorespiratory Frequency Monitoring Using the Principal Component Analysis Technique on UWB Radar Signal». In: *International Journal of Antennas and Propagation* 2017 (2017). ISSN: 16875877. DOI: 10.1155/2017/4803752 (cit. on pp. 3, 30).

[10] M Donelli. *A RESCUE RADAR SYSTEM FOR THE DETECTION OF VICTIMS TRAPPED UNDER RUBBLE BASED ON THE INDEPENDENT COMPONENT ANALYSIS ALGORITHM*. 2011, pp. 173–181 (cit. on pp. 4, 30).

[11] S. K. Niranjan, Institute of Electrical, Electronics Engineers, Institute of Electrical, Electronics Engineers. Bangalore Section, and IEEE Computational Intelligence Society. Bangalore Chapter. *Proceedings of the Second International Conference on Green Computing and Internet of Things (ICGCIoT 2018) : 16-18 August 2018, Karnataka, India*. ISBN: 9781538656570 (cit. on p. 4).

[12] Marco Mercuri, Ping Jack Soh, Gokarna Pandey, Peter Karsmakers, Guy A.E. Vandenbosch, Paul Leroux, and Dominique Schreurs. «Analysis of an indoor biomedical radar-based system for health monitoring». In: *IEEE Transactions on Microwave Theory and Techniques* 61 (5 2013), pp. 2061–2068. ISSN: 00189480. DOI: 10.1109/TMTT.2013.2247619 (cit. on pp. 4, 29).

[13] Fadel Adib, Hongzi Mao, Zachary Kabelac, Dina Katabi, and Robert C. Miller. «Smart homes that monitor breathing and heart rate». In: vol. 2015-April. Association for Computing Machinery, Apr. 2015, pp. 837–846. ISBN: 9781450331456. DOI: 10.1145/2702123.2702200 (cit. on p. 4).

[14] Hui Sup Cho and Young Jin Park. «Detection of heart rate through a wall using UWB impulse radar». In: *Journal of Healthcare Engineering* 2018 (2018). ISSN: 20402309. DOI: 10.1155/2018/4832605 (cit. on p. 4).

[15] Masashi Muragaki, Shigeaki Okumura, Takuya Sakamoto, and Toru Sato. *Non-contact respiration measurement using ultra-wideband array radar with adaptive beamforming technique for cancer radiotherapy; Non-contact respiration measurement using ultra-wideband array radar with adaptive beamforming technique for cancer radiotherapy*. 2016 (cit. on p. 4).

[16] *Radar perimetrali per applicazioni automotive Elaborato in Comunicazioni Digitali e Internet* (cit. on pp. 4, 22, 23).

[17] «Radar-based Monitoring of Vital Signs: A Tutorial Overview». In: (). DOI: 10.36227/techrxiv.19212918.v1. URL: https://doi.org/10.36227/techrxiv.19212918.v1 (cit. on pp. 6, 26).

[18] Ferran Cañellas Cruz, Idelfonso Tafur Monroy, Juan José, and Vegas Olmos. *Radar system based on Frequency-Modulated Continuous Wave transmission*. 2016 (cit. on pp. 7, 9, 10, 26).

[19] «[75] Non-contact acquisition of respiration and heart rates using Doppler radar with time domain peak-detection algorithm $_{E}nhancedReader$». In: () (cit. on pp. 9, 26).

[20] *Radartutorial*. URL: https://www.radartutorial.eu/02.basics/Frequency%20Modulated%20Continuous%20Wave%20Radar.en.html (cit. on pp. 9, 10).

[21] Simon Kingsley and Shaun Quegan. *Understanding radar systems*. Vol. 2. SciTech Publishing, 1999 (cit. on p. 20).

[22] *The Process of Breathing | Anatomy and Physiology II*. URL: https://courses.lumenlearning.com/suny-ap2/chapter/the-process-of-breathing-no-content/ (cit. on p. 25).

[23] Alysson Roncally Carvalho and Walter Araujo Zin. *Respiratory system dynamical mechanical properties: Modeling in time and frequency domain*. June 2011. DOI: 10.1007/s12551-011-0048-5 (cit. on p. 26).

[24] Junhyeong Park, Jong Wook Ham, Seungwoon Park, Do Hoon Kim, Seong Jin Park, Hyunseong Kang, and Seong Ook Park. «Polyphase-Basis Discrete Cosine Transform for Real-Time Measurement of Heart Rate with CW Doppler Radar». In: *IEEE Transactions on Microwave Theory and Techniques* 66 (3 Mar. 2018), pp. 1644–1659. ISSN: 00189480. DOI: 10.1109/TMTT.2017.2772782 (cit. on pp. 26, 28).

[25] Mehrdad Nosrati and Negar Tavassolian. «High-Accuracy Heart Rate Variability Monitoring Using Doppler Radar Based on Gaussian Pulse Train Modeling and FTPR Algorithm». In: *IEEE Transactions on Microwave Theory and Techniques* 66 (1 Jan. 2018), pp. 556–567. ISSN: 00189480. DOI: 10.1109/TMTT.2017.2721407 (cit. on p. 26).

[26] Marcin Włodarczak. *RespInPeace: Toolkit for Processing Respiratory Belt Data* (cit. on p. 27).

[27] Chathuri Daluwatte, Christopher G. Scully, George C. Kramer, and David G. Strauss. «A robust detection algorithm to identify breathing peaks in respiration signals from spontaneously breathing subjects». In: vol. 42. IEEE Computer Society, Feb. 2015, pp. 297–300. ISBN: 9781509006854. DOI: 10.1109/CIC.2015.7408645 (cit. on p. 27).

[28] D. Khodadad et al. «Optimized breath detection algorithm in electrical impedance tomography». In: *Physiological Measurement* 39 (9 Sept. 2018). ISSN: 13616579. DOI: 10.1088/1361-6579/aad7e6 (cit. on p. 27).

[29] Muhammad Arsalan, Avik Santra, and Christoph Will. «Improved Contactless Heartbeat Estimation in FMCW Radar via Kalman Filter Tracking». In: *IEEE Sensors Letters* 4 (5 May 2020). ISSN: 24751472. DOI: 10.1109/LSENS.2020.2983706 (cit. on p. 28).

[30] Yuyong Xiong, Shiqian Chen, Xingjian Dong, Zhike Peng, and Wenming Zhang. «Accurate measurement in doppler radar vital sign detection based on parameterized demodulation». In: *IEEE Transactions on Microwave Theory and Techniques* 65 (11 Nov. 2017), pp. 4483–4492. ISSN: 00189480. DOI: 10.1109/TMTT.2017.2684138 (cit. on p. 29).

[31] Gabor Vinci, Stefan Lindner, Francesco Barbon, Sebastian Mann, Maximilian Hofmann, Alexander Duda, Robert Weigel, and Alexander Koelpin. «Six-port radar sensor for remote respiration rate and heartbeat vital-sign monitoring». In: *IEEE Transactions on Microwave Theory and Techniques* 61 (5 2013), pp. 2093–2100. ISSN: 00189480. DOI: 10.1109/TMTT.2013.2247055 (cit. on pp. 29, 41).

[32] Jeeeun Lee and Sun K. Yoo. «Radar-based detection of respiration rate with adaptive harmonic quefrency selection». In: *Sensors (Switzerland)* 20 (6 Mar. 2020). ISSN: 14248220. DOI: 10.3390/s20061607 (cit. on p. 29).

[33] Mari Zakrzewski, Harri Raittinen, and Jukka Vanhala. «Comparison of center estimation algorithms for heart and respiration monitoring with microwave doppler radar». In: *IEEE Sensors Journal* 12 (3 2012), pp. 627–634. ISSN: 1530437X. DOI: 10.1109/JSEN.2011.2119299 (cit. on p. 29).

[34] Jonas Weib, Rodrigo Perez, and Erwin Biebl. «Improved People Counting Algorithm for Indoor Environments using 60 GHz FMCW Radar». In: vol. 2020-September. Institute of Electrical and Electronics Engineers Inc., Sept. 2020. ISBN: 9781728189420. DOI: 10.1109/RadarConf2043947.2020.9266607 (cit. on p. 29).

[35] Adeel Ahmad, June Chul Roh, Dan Wang, and Aish Dubey. «Vital signs monitoring of multiple people using a FMCW millimeter-wave sensor». In: Institute of Electrical and Electronics Engineers Inc., June 2018, pp. 1450–1455. ISBN: 9781538641675. DOI: 10.1109/RADAR.2018.8378778 (cit. on p. 29).

[36] A Hyvärinen and E Oja. *Independent component analysis: algorithms and applications*. URL: www.elsevier.com/locate/neunet (cit. on p. 30).

[37] Ganesh R Naik and Dinesh K Kumar. *An Overview of Independent Component Analysis and Its Applications*. 2011, pp. 63–81 (cit. on p. 30).

[38] Hervé Abdi and Lynne J. Williams. *Principal component analysis*. July 2010. DOI: 10.1002/wics.101 (cit. on p. 30).

[39] Konstantin Dragomiretskiy and Dominique Zosso. «Variational mode decomposition». In: *IEEE Transactions on Signal Processing* 62 (3 Feb. 2014), pp. 531–544. ISSN: 1053587X. DOI: 10.1109/TSP.2013.2288675 (cit. on p. 31).

[40] Hongming Shen, Chen Xu, Yongjie Yang, Ling Sun, Zhitian Cai, Lin Bai, Edward Clancy, and Xinming Huang. «Respiration and Heartbeat Rates Measurement Based on Autocorrelation Using IR-UWB Radar». In: *IEEE Transactions on Circuits and Systems II: Express Briefs* 65 (10 Oct. 2018), pp. 1470–1474. ISSN: 15583791. DOI: 10.1109/TCSII.2018.2860015 (cit. on p. 31).

[41] «Infineon-BGT60ATR24C-DataSheet-v01$_0$0 − EN». In: () (cit. on pp. 32, 34).

[42] Anda R. Guraliuc, Maxim Zhadobov, Guido Valerio, Nacer Chahat, and Ronan Sauleau. «Effect of textile on the propagation along the body at 60 ghz». In: *IEEE Transactions on Antennas and Propagation* 62 (3 2014), pp. 1489–1494. ISSN: 0018926X. DOI: 10.1109/TAP.2013.2295425 (cit. on p. 41).

[43] Nacer Chahat, Maxim Zhadobov, Ronan Sauleau, and Stanislav I. Alekseev. «New method for determining dielectric properties of skin and phantoms at millimeter waves based on heating kinetics». In: *IEEE Transactions on Microwave Theory and Techniques* 60 (3 PART 2 Mar. 2012), pp. 827–832. ISSN: 00189480. DOI: 10.1109/TMTT.2011.2176746 (cit. on p. 41).

[44] Nacer Chahat, Guido Valerio, Maxim Zhadobov, and Ronan Sauleau. «On-body propagation at 60 GHz». In: *IEEE Transactions on Antennas and Propagation* 61 (4 2013), pp. 1876–1888. ISSN: 0018926X. DOI: 10.1109/TAP.2013.2242034 (cit. on p. 41).

[45] Fulai Liang, Fugui Qi, Qiang An, Hao Lv, Fuming Chen, Zhao Li, and Jianqi Wang. «Detection of multiple stationary humans using UWB MIMO radar». In: *Sensors (Switzerland)* 16 (11 Nov. 2016). ISSN: 14248220. DOI: 10.3390/s16111922 (cit. on p. 41).

[46] James C Lin. *New IEEE Standard for Safety Levels with Respect to Human Exposure to Radio-Frequency Radiation*. URL: http://mmfai.info/public/docs/eng! (cit. on p. 41).

[47] Guohua Lu, Fang Yang, Yue Tian, Xijing Jing, and Jianqi Wang. «Contact-free measurement of heart rate variability via a microwave sensor». In: *Sensors* 9 (12 Dec. 2009), pp. 9572–9581. ISSN: 14248220. DOI: 10.3390/s91209572 (cit. on p. 41).

[48] «Manuale stampante x400$_p ro_v 3_3 d$». In: () (cit. on p. 63).

[49] *biosignal acquisition tool-kit for advanced research applications*. URL: `http://www.plux.info` (cit. on p. 85).

[50] *Inductive Respiration (RIP) Sensor Data Sheet RIP 27042015*. 2015. URL: `http://biosignalsplux.com/` (cit. on p. 86).

[51] *Electrocardiography (ECG) Sensor Datasheet ECG 10082020*. 2020. URL: `http://biosignalsplux.com/` (cit. on p. 86).